2017

Where to draw the line: Chasing energy extrapolations, cluster convergence, and molecular trajectories

Jeffery Boschen
Iowa State University

Recommended Citation

Boschen, Jeffery, "Where to draw the line: Chasing energy extrapolations, cluster convergence, and molecular trajectories" (2017). *Graduate Theses and Dissertations*. 15493.
https://lib.dr.iastate.edu/etd/15493

Where to draw the line: Chasing energy extrapolations, cluster convergence, and molecular trajectories

by

Jeffery Scott Boschen

A dissertation submitted to the graduate faculty

in partial fulfillment of the requirements for the degree of

DOCTOR OF PHILOSOPHY

Major: Physical Chemistry

Program of Study Committee:
Theresa L. Windus, Major Professor
Mark S. Gordon
William S. Jenks
Jacob W. Petrich
Xueyu Song

Iowa State University

Ames, Iowa

2017

TABLE OF CONTENTS

ACKNOWLEDGMENTS

I would first like to thank my advisor, Prof. Theresa Windus, for giving me years of support and guidance, but also plenty of freedom during my time in graduate school. I'd also like to thank the members of my committee, Profs. Mark Gordon, William Jenks, Jake Petrich, and Xueyu Song for their support.

I'm grateful to Prof. Klaus Ruedenberg for continuing to share his expertise in helpful discussions and collaborations. Thank you to Dr. Federico Zahariev for a number of helpful discussions. Thank you to Dr. Da-Jiang Liu, Prof. Jim Evans and Prof. Pat Thiel for a fruitful collaboration and exposing me to a bit of surface chemistry. To the past and present members of the Windus group, thanks for making the office an enjoyable place to work. In particular, I want to thank Dr. Dan Theis for initiating much of the work that would become chapters in this thesis.

Finally, a very special thank you to all my friends and family who have kept me encouraged me over the years, but most of all to my parents, Scott and Sara, for their incredible love and support.

This work was supported by the U.S. Department of Energy (DOE), Office of Basic Energy Sciences, Division of Chemical Sciences, Geosciences & Biosciences at the Ames Laboratory under contract number DE-AC02-07CH11358. The Ames Laboratory is operated for the DOE by Iowa State University. The document number assigned to this thesis/dissertation is IS-T 3208.

ABSTRACT

The adsorption of S on Cu surfaces is studied by density functional theory using both plane-wave and atomic orbital basis sets. Calculations are performed on Cu clusters of increasing sizes, and strong oscillations in the S-Cu binding energy versus cluster size are found. Although expected for small clusters, the oscillations persist even to clusters containing a few hundred atoms. Smearing of the occupancy function in plane-wave DFT, and averaging over clusters of different sizes are presented as possible approaches to approximate bulk results using small to medium sized clusters.

Chemically accurate potential energy curves for the lowest lying singlet states of C_2 are obtained using the correlation energy extrapolation by intrinsic scaling (CEEIS) method. The potential energies also include complete basis set extrapolation, core-valence correlation, spin-orbit coupling, and scalar relativistic effects. Our calculated ro-vibrational levels show deviations from experiment of between ~10-20 cm^{-1}, demonstrating near spectroscopic accuracy.

The correlation energy extrapolation by many-body expansion (CEEMBE) method is presented. Like the CEEIS method, CEEMBE approximates configuration interaction (CI) energies using a linear extrapolation from CI calculations with reduced numbers of virtual orbitals. The method also uses a many-body expansion of the CI energy based on separating the valence orbitals into groups. Tests on ozone and F_2 potential energy surfaces show that CI energies can be reproduced to within a few millihartree, and in many cases to within less than 1 millihartree. We also present a hybrid methodology, CEEMBE-*h*, which adds CEEIS style extrapolations to the CEEMBE procedure. CEEMBE-*h* reproduces the original CEEMBE energies to within 0.1-0.5 millihartree or less.

Nonadiabatic dynamics using spin-flip time-dependent density functional theory (SF-TDDFT) are presented for the penta-2,4-dieniminium cation. We developed an interface between the GAMESS and Newton-X programs for SF-TDDFT dynamics. Time-derivative couplings between SF-TDDFT states are calculated using an approximate wavefunction overlap method. Our comparison with analytical couplings from CASSCF demonstrates that the overlap method for time-derivative couplings is effective for SF-TDDFT. Because of the spin-contamination in SF-TDDFT, the interface includes a state-tracking algorithm to ensure dynamics are propagated on the correct potential energy surface.

CHAPTER 1. INTRODUCTION

General Overview

The interactions between adsorbates and metal surfaces is of interest for understanding surface reconstruction, catalytic effects, and the anchoring of other ligands. Modeling a practically infinite metal surface can be challenging, but cluster models can be used to examine the local interactions between a substrate and the metal surface. Understanding how properties, such as binding energy, depend on the cluster size can reveal insight into the bulk behavior, as well as help evaluate the validity of the cluster model.

Theoretical calculations which can reproduce experimental energies to within 1 kcal/mol are said to achieve “chemical accuracy”. Such methods provide powerful tools for predicting and interpreting experimental results, as well as benchmarking other theoretical methods. One major challenge to achieving such accuracy is recovering the electron correlation energy, which is captured exactly by full configuration interaction. As such, methods which can approximate configuration interaction energies at a reduced computational expense are an active area of research in quantum chemistry.

Although much of the work done in computational chemistry falls within a time-independent frame work, the dynamic evolution of chemical systems in time is also of great importance. However, using quantum chemistry methods within molecular dynamics simulations can be impractical when the process of interest occurs over too long of timescales. Ultrafast photoinduced processes which occur on sub-picosecond timescales are a reasonable target for quantum molecular dynamics simulations. Such reactions are relevant to biology (vision, deactivation of DNA), and have potential applications in solar energy, as well as molecular probes, switches, and motors.

Theoretical Background

The Schrödinger Equation

The time evolution of a non-relativistic quantum system is given by the Schrödinger equation[1–6] (equations given in atomic units):

$$i\frac{\partial}{\partial t}\Psi(\mathbf{r},\mathbf{R},t) = \hat{H}\Psi(\mathbf{r},\mathbf{R},t) \tag{1}$$

Ψ is the wavefunction of the system and depends on the time, t, and the coordinates, $\mathbf{r}$ and $\mathbf{R}$, of all electrons and nuclei, respectively. Whenever the Hamiltonian, $\hat{H}$, does not depend on time, the equation can be simplified to the following eigenvalue problem:

$$\hat{H}\Psi(\mathbf{r},\mathbf{R}) = E\Psi(\mathbf{r},\mathbf{R}) \tag{2}$$

Wavefunctions that satisfy this time-independent Schrödinger equation are referred to as stationary states and their time dependence is given by a simple phase factor:

$$\Psi(\mathbf{r},\mathbf{R},t) = e^{-iEt}\Psi(\mathbf{r},\mathbf{R},t=0) \tag{3}$$

Quantum chemistry methods are used to solve or approximate solutions to these equations.

In molecular systems without an external potential, the Hamiltonian is given by:

$$\begin{aligned}\hat{H} = \sum_{i=1}^{N}\frac{-\nabla_i^2}{2} + \sum_{A=1}^{K}\frac{-\nabla_A^2}{2M_A} + \sum_{i=1}^{N}\sum_{A=1}^{K}\frac{-Z_A}{|r_i - R_A|} \\ + \sum_{i=1}^{N}\sum_{j>i}^{N}\frac{1}{|r_i - r_j|} + \sum_{A=1}^{K}\sum_{B>A}^{K}\frac{Z_A Z_B}{|R_A - R_B|}\end{aligned} \tag{4}$$

where the sums contain the electronic and nuclear kinetic energies, the electron-nuclear attraction, the electron-electron repulsion, and the nuclear-nuclear repulsion, respectively. N and

K are the number of electrons and nuclei, M and Z are the mass and charge of the nuclei, and R and r are the positions of the nuclei and electrons, respectively. The time-independent Schrödinger equation can be further simplified by assuming that the nuclear and electronic coordinates can be separated and the wavefunction written as a product of two functions:

$$\Psi(\mathbf{r},\mathbf{R}) = \psi_{nucl}(\mathbf{R})\psi_{elec}(\mathbf{r};\mathbf{R}) \tag{5}$$

This is known as the Born-Oppenheimer approximation[7] and gives the standard problem of electronic structure theory:

$$\hat{H}_{elec}\psi_{elec}(\mathbf{r}) = E_{elec}\psi_{elec}(\mathbf{r};\mathbf{R}) \tag{6}$$

This electronic Schrödinger equation only depends parametrically on the nuclear coordinates: $\hat{H}_{elec}$ only includes the terms from equation (4) that depend on the electronic coordinates. An approximation of the total energy of the system can be obtained by adding the nuclear-nuclear repulsion energy to E_{elec}. The physical motivation for the approximation is that the large difference between the masses of electrons and nuclei allows the electrons to adjust instantaneously to nuclear motion.

Hartree-Fock Theory

Solving the electronic Schrödinger equation exactly is not practical for most chemical systems. The standard approach in quantum chemistry is to use the Hartree-Fock method[8–11] as a starting approximation. The ansatz for the wavefunction in Hartree-Fock theory is based on a product of one-electron functions (orbitals):

$$\phi_1(r_1)\phi_2(r_2)\phi_3(r_3)\ldots\phi_N(r_N) \tag{7}$$

The orbitals contain both spatial and spin components. This Hartree product ansatz fails to satisfy the antisymmetric property of fermions, so instead the determinant of the following matrix is used as a wavefunction:

$$\Psi_{HF}(\mathbf{r}) = \frac{1}{\sqrt{N!}} \begin{vmatrix} \phi_1(r_1) & \phi_2(r_1) & \cdots & \phi_N(r_1) \\ \phi_1(r_2) & \phi_2(r_2) & \cdots & \phi_N(r_N) \\ \vdots & \vdots & \ddots & \vdots \\ \phi_1(r_N) & \phi_2(r_N) & \cdots & \phi_N(r_N) \end{vmatrix} \tag{8}$$

This wavefunction form is known as a Slater determinant[12].

The energy of Ψ_{HF} can be found using $\hat{H}_{elec}$, and a set of conditions for minimizing the energy of Ψ_{HF} can be derived. These are known as the Hartree-Fock equations:

$$\hat{f}(r_1)\phi_i(r_1) = \epsilon_i \phi_i(r_1) \tag{9}$$

where ϵ_i is the energy of the ith molecular orbital, ϕ_i, and $\hat{f}$ is the Fock operator, a one-electron operator which has the form:

$$\hat{f}(r_1) = -\frac{\nabla_1^2}{2} + \sum_A^K \frac{-Z_A}{|r_1 - R_A|} + \sum_j^N \left[\hat{J}_j(r_1) - \hat{K}_j(r_1)\right] \tag{10}$$

$$\hat{J}_j(r_1)\phi_i(r_1) = \left[\int d\mathbf{r}_2\, \phi_j^*(r_2) \frac{1}{|r_1 - r_2|} \phi_j(r_2)\right] \phi_i(r_1) \tag{11}$$

$$\hat{K}_j(r_1)\phi_i(r_1) = \left[\int d\mathbf{r}_2\, \phi_j^*(r_2) \frac{1}{|r_1 - r_2|} \phi_i(r_2)\right] \phi_j(r_1) \tag{12}$$

The first two terms of equation (10) give the kinetic energy and nuclear attraction of one electron while the last term includes the Coulomb ($\hat{J}$) and exchange ($\hat{K}$) operators. The Coulomb and exchange operators describe the average repulsion felt by one electron from the other electrons in the system. $\hat{K}$ arises from the antisymmetric character of the Slater determinant. The Fock operator and the coupled set of equations from equation (9) give the conditions on the orbitals needed to minimize the energy of the wavefunction.

In practice, the form of the molecular orbitals must be specified to solve the Hartree-Fock equations. The most common choice for the molecular orbitals is to take linear combinations of atomic orbitals (LCAOs):

$$\phi_i = \sum_{\mu} C_{\mu i} \chi_{\mu} \tag{13}$$

Each molecular orbital is expanded in a basis of atom-centered functions (χ). These atomic orbitals are most often implemented as Gaussian functions. With this expansion, the problem can be reduced to a matrix equation. For a closed shell system the Hartree-Fock solution can be found from the Roothaan-Hall equations[13,14]:

$$\mathbf{FC} = \mathbf{SC\epsilon} \tag{14}$$

where the matrix elements of **F** and **S** are defined as:

$$F_{\mu\nu} = \langle \chi_{\mu} | \hat{f} | \chi_{\nu} \rangle \tag{15}$$

$$S_{\mu\nu} = \langle \chi_{\mu} | \chi_{\nu} \rangle \tag{16}$$

C and $\boldsymbol{\epsilon}$ are the LCAO coefficients and orbital energies, respectively. The Roothaan-Hall equations are nonlinear because the Fock matrix depends on the LCAO coefficients. As a result the problem must be solved iteratively. In each cycle the Fock matrix is diagonalized to find the molecular orbital coefficients, which in turn produce a new Fock matrix. The solution is found once this process reaches self-consistency: when the iterative process produces the same molecular orbitals and energy after each step.

Due to the variational principle, the Hartree-Fock energy serves as an upper bound for the exact ground state energy. Because the Hartree-Fock wavefunction only allows the electrons to interact through an average field, explicit correlation of electron positions is neglected. The difference between the Hartree-Fock energy and the exact non-relativistic energy is called the correlation energy. Although typically a small portion of the total energy of the system, describing electron correlation is usually necessary to describe reaction energies to within chemical accuracy (~1 kcal/mol).

Configuration Interaction

In many chemical systems and processes, the single reference nature (i.e. one Slater determinant) of the Hartree-Fock wavefunction leads to poor accuracy. The Hartree-Fock method cannot even qualitatively describe the dissociation of a diatomic molecule (and other bond-breaking processes). Even equilibrium structures of simple systems may have multi-reference character, as will be seen in Chapter 4, a study of C_2. One solution to address this problem and introduce electron correlation is to describe the system using additional configurations. The configuration interaction (CI) approach variationally minimizes the energy of a wavefunction that is a linear combination of several configurations. Starting from some reference state (typically the Hartree-Fock ground state), additional determinants may be generated by replacing some number of occupied orbitals with virtual orbitals:

$$\psi_0 = |\phi_1 \dots \phi_i \dots \phi_N| \rightarrow |\phi_1 \dots \phi_a \dots \phi_N| = \psi_i^a \qquad (17)$$

where *i* and *a* correspond to occupied and virtual orbitals respectively in the Hartree-Fock reference. Such an occupied to virtual substitution is referred to as an “excitation”, and the example above produces a singly excited determinant.

The case where all possible excited determinants are included in the wavefunction is known as full configuration interaction (FCI):

$$\Psi_{CI} = c_0\psi_0 + \sum_{i,a} c_i^a \psi_i^a + \sum_{\substack{i<j \\ a<b}} c_{ij}^{ab}\, \psi_{ij}^{ab} + \sum_{\substack{i<j<k \\ a<b<c}} c_{ijk}^{abc}\, \psi_{ijk}^{abc} \dots \qquad (18)$$

where *a*, *b*, *c* and *i*, *j*, *k* are virtual and occupied orbitals, respectively. This wavefunction includes sums running over all possible singly, doubly, triply, etc. excited determinants, up to the number of electrons in the system.

Minimizing the energy of Ψ_{CI} with respect to the c coefficients yields the matrix equation:

$$\mathbf{Hc} = E\mathbf{Sc} \tag{19}$$

$$H_{ij} = \langle \psi_i | \hat{H}_{elec} | \psi_j \rangle \tag{20}$$

$$S_{ij} = \langle \psi_i | \psi_j \rangle \tag{21}$$

where the ψ_i correspond to the Slater determinants from equation (18). Equation (19) will have a number of solutions equal to the number of configurations in equation (18), each with an energy E and set of c coefficients describing the wavefunction. The lowest energy solution corresponds to the ground state of the system and higher energy solutions correspond to excited states. From the Hylleraas-Undheim-MacDonald theorem[15,16], each CI solution is a strict upper bound on the true energy of the corresponding state.

A FCI wavefunction will give the exact solution to the Schrödinger equation for a given basis set. Thus, FCI can completely recover the correlation energy (within a particular basis set). However, the number of configurations increases factorially with the size of the system and is impractical for all but the smallest systems or basis sets. In practice, most CI calculations restrict the number of configurations in some way, such as only including excitations up to a certain number of electrons. For example, if equation (18) is truncated at the third term, the method is CI with single and double excitations (CISD).

In some cases, the Hartree-Fock orbitals are not a suitable reference for (truncated) CI calculations. Another approach is to variationally optimize the reference orbitals for the specific choice of configurations included in the CI wavefunction. This is known as the multi-configurational self-consistent field (MCSCF) method. MCSCF wavefunctions are optimized with respect to both the CI coefficients and the atomic basis coefficients of the molecular orbitals. In most implementations of the MCSCF method, one alternates between orbital improvement and CI steps in each iteration until the energy has converged with respect to both sets of coefficients.

The choice of configurations to include in an MCSCF calculation is both nontrivial and important for the quality of the result. Although many schemes exist for generating configurations, a common approach is known as the complete active space (CAS)[17] or fully optimized reaction space (FORS)[18]. In this method, a set of orbitals are chosen from some reference set (typically Hartree-Fock orbitals). The orbitals are chosen to include all those relevant for the process of interest. For example, to describe a bond dissociation it is necessary to include both bonding and anti-bonding orbitals. Within this active space of orbitals, all possible configurations are generated and included in the MCSCF wavefunction.

For especially high accuracy, it is possible to combine the MCSCF method with truncated CI approaches. These calculations are known as multi-reference CI (MRCI). A set of MCSCF orbitals and configurations are taken as the reference wavefunction, and then further excitations into the virtual orbital space are allowed from each configuration in the MCSCF wavefunction. For example, one might include in an MRCI calculation the MCSCF reference determinants plus all the determinants generated by allowing up to double excitations from any of the reference determinants into the virtual orbital space (i.e. MR-CISD).

Full CI calculations scale factorially with the size of the system and are impractical to perform for all but the smallest chemical systems. In practice, most CI calculations only include up to double excitations. However, it is well known that much of the correlation energy can be recovered without including the full set of determinants into the wavefunction. The development of methods to approximate CI energies that include higher levels of excitation is an active area of research and Chapters 4, 5 and 6 of this work present and apply two such methods: correlation energy extrapolation by intrinsic scaling (CEEIS) and correlation energy extrapolation by many-body expansion (CEEMBE).

Density Functional Theory

Another foundation for electronic structure calculations is density functional theory (DFT). DFT focuses on the electron density rather than the wavefunction. This is motivated by the Hohenberg-Kohn theorems[19], which prove that there is a one-to-one correspondence between the electron density and the potential. Consequently, the density determines the wavefunction and properties of the system: the energy is a functional of the density. Most DFT calculations in chemistry (including the studies in this work) use the Kohn-Sham formulation[20] of DFT. In Kohn-Sham DFT, the density is expanded in a basis of one-electron orbitals. This leads to equations that are similar to Hartree-Fock theory, where the Fock operator is replaced by the one-electron Kohn-Sham operator:

$$\hat{h}_{KS} = -\frac{\nabla^2}{2} + \sum_{A}^{K} \frac{-Z_A}{|r - R_A|} + \int dr' \frac{\rho(r')}{|r - r'|} + \hat{V}_{XC}(r) \tag{22}$$

where ρ is the electron density. The terms in equation (22) correspond to the electron kinetic energy, the electron-nuclear attraction, the electron-electron repulsion, and the exchange-correlation functional: $\hat{V}_{XC}$. This allows DFT to incorporate correlation effects not included at the Hartree-Fock level. If $\hat{V}_{XC}$ were known exactly, then the exact energy of the system could be calculated. However, the exact functional is unknown and in practice DFT calculations require the selection of an approximate functional. Careful selection of the density functional is required for obtaining good quality results for a given chemical system and desired property.

Time-Dependent DFT

DFT can also be applied to excited state calculations, and the most common approach is time-dependent density functional theory (TDDFT). In analogy to the Hohenberg-Kohn theorems of time-independent DFT, TDDFT is motivated by the Runge-Gross theorem[21] which maps the time-dependent electron density to the time-dependent wavefunction, up to a phase factor. As in the time-independent case, the Kohn-Sham formalism will be used to represent the time-dependent density in a basis of atomic orbitals.

Excitation energies can be obtained by considering an infinitesimal time-dependent perturbation applied to the system. The poles in the linear response of the density to the perturbation will correspond to the excitation energies. In the Casida formalism[22], these are given by the matrix equation:

$$\begin{pmatrix} \mathbf{A} & \mathbf{B} \\ \mathbf{B}* & \mathbf{A}* \end{pmatrix} \begin{pmatrix} \mathbf{X} \\ \mathbf{Y} \end{pmatrix} = \boldsymbol{\omega} \begin{pmatrix} \mathbf{1} & \mathbf{0} \\ \mathbf{0} & -\mathbf{1} \end{pmatrix} \begin{pmatrix} \mathbf{X} \\ \mathbf{Y} \end{pmatrix} \tag{23}$$

with elements given by:

$$\mathbf{A}_{ia,jb} = (\epsilon_a - \epsilon_i)\delta_{ab}\delta_{ij} + \frac{\partial \mathbf{F}_{ia}}{\partial \mathbf{P}_{jb}} \tag{24}$$

$$\mathbf{B}_{ai,bj} = \frac{\partial \mathbf{F}_{ai}}{\partial \mathbf{P}_{jb}} \tag{25}$$

$$\mathbf{F}_{pq} = \int dx \phi_p(x) \left[-\frac{\nabla_{\mathrm{r}}^2}{2} - \sum_A \frac{Z_A}{|r - R_A|} + \int dx' \frac{\rho(x')}{|r - r'|} + \hat{V}_{XC}(x) \right] \phi_q(x) \tag{26}$$

$\boldsymbol{\omega}$ contains the excitation energies, $\omega_i = E_i - E_0$, where E_i is the energy of the ith excited state and E_0 is the energy of the DFT ground state. **X** and **Y** are response vectors with elements that correspond to excitations and de-excitations respectively. These excitations correspond to pairs of occupied/virtual orbitals. **F** is the Kohn-Sham Hamiltonian, **P** is the one electron density matrix, and the ϵ_i are Kohn-Sham orbital energies. The problem can be simplified further by using the Tamm-Dancoff approximation[23,24], which eliminates the **B** elements from the matrix equation:

$$\mathbf{A}\mathbf{X} = \boldsymbol{\omega}\mathbf{X} \tag{27}$$

Since **X** only contains single excitations, the Tamm-Dancoff approximation produces a formalism that is very similar to configuration interaction with single excitations (CIS). The approximation has been found to yield excitation energies which are in good agreement with the full TDDFT method, at a reduced computational expense. In general, the terms neglected in the Tamm-Dancoff approximation are relatively small.

The TDDFT approach described above has some shortcomings. One is that the excited states are described solely by single excitations into the virtual orbitals. Excited states which are characterized by double or higher excitations cannot be adequately represented. Another is that the ground and excited states are treated differently in the formalism. One consequence of these shortcomings is that the potential energy surfaces near conical intersections between ground and excited states in TDDFT do not exhibit the correct topology[25,26]. A related method that can address these issues is the “spin-flip” formulation of TDDFT (SF-TDDFT)[27].

In SF-TDDFT the reference orbitals are taken from a ground state DFT calculation with higher spin than the states of interest. For example, when targeting singlet states, a high spin triplet is used as the reference. The states of interest are then generated by allowing spin-flip excitations from the reference. These excitations involve single transitions from α to β spin orbitals. Assuming the Tamm-Dancoff approximation, the matrix **A** from equation (27) will only include contributions from the spin-flip excitations, and the excitation energies $\boldsymbol{\omega}$ will be relative to the high spin reference. In this formulation, the target ground state as well as the target excited states are all treated in the same manner and the proper conical intersection topology between ground and excited states is recovered.

Molecular Dynamics with Surface Hopping

All the methods described so far solve the time-independent Schrödinger equation with fixed nuclear coordinates. But the dynamic behavior of chemical systems in time is also of great interest. In this work, molecular dynamics will be described by a mixed quantum-classical approach that treats the nuclei classically while the electronic degrees of freedom follow quantum mechanics. The wavefunction obeys the electronic time-dependent Schrödinger equation:

$$i\frac{\partial}{\partial t}\Psi_{elec}(\mathbf{r},\mathbf{R},t) = \hat{H}_{elec}\Psi_{elec}(\mathbf{r},\mathbf{R},t) \tag{28}$$

and the wavefunction can be expanded in a basis of adiabatic states:

$$\Psi_{elec}(\mathbf{r},\mathbf{R},t) = \sum_j C_j(t)\psi_j\,(\mathbf{r};\mathbf{R}) \tag{29}$$

The ψ_j are time-independent solutions to equation (6), and only depend on the nuclear coordinates parametrically. Inserting equation (29) into equation (28) and integrating gives the time dependence of the C_j amplitudes:

$$\frac{\partial}{\partial t}C_j(t) = -\sum_k C_k(t)\left(iH_{jk} + \left\langle\psi_j\middle|\frac{\partial}{\partial t}\psi_k\right\rangle\right) \tag{30}$$

$$\frac{\partial}{\partial t}C_j(t) = -\sum_k C_k(t)\left(iH_{jk} + \frac{\partial\mathbf{R}}{\partial t}\cdot\mathbf{d}_{jk}\right) \tag{31}$$

$$H_{jk} = \langle\psi_j|\hat{H}_{elec}|\psi_k\rangle \tag{32}$$

$$d_{jk}^{(R)} = \left\langle\psi_j\middle|\frac{\partial}{\partial R}\psi_k\right\rangle \tag{33}$$

H_{jk} is the Hamiltonian matrix element between two adiabatic states, $\mathbf{R}$ is a vector of the nuclear coordinates, and $\mathbf{d}_{jk}$ is a vector of the so-called nonadiabatic coupling matrix elements (NACMEs) between adiabatic states. The $\left\langle \psi_j \middle| \frac{\partial}{\partial t} \psi_k \right\rangle$ term is referred to as the time-derivative coupling. The population of an electronic state is given by $P_{jj} = \left| C_j^* C_j \right|$.

The nonadiabatic dynamics of the system can be incorporated in various ways, but in this work will be described using the "surface hopping" method.[28,29] An ensemble of independent trajectories is used to represent the system. At each time step, a trajectory has defined nuclear positions and momenta, amplitudes C_i for all ψ_i, and is associated with a specific adiabatic surface ψ_j. The classical propagation of the nuclei is achieved by calculating the forces on the nuclei due to the energy of the active electronic state:

$$F_R = \frac{\partial}{\partial R} H_{jj} = \frac{\partial}{\partial R} E_j \tag{34}$$

The force is given by the nuclear gradient of the currently active adiabatic surface.

Nonadiabatic effects are included by allowing the active adiabatic surface to change, or "hop", after each time step. Whether a trajectory hops to another state or not is a random process where the likelihood depends on the populations and coupling between the states. The most popular surface hopping scheme is Tully's fewest switches surface hopping (FSSH) method.[29] In FSSH, the hopping probability from ψ_j to ψ_k is given by:

$$T_{j \to k} = \frac{2}{P_{jj}} \int_t^{t+\Delta t} \mathrm{Re}\left(P_{jk} \frac{\partial \mathbf{R}}{\partial t} \cdot \mathbf{d}_{jk} \right) dt \tag{35}$$

If this number exceeds a randomly determined value between 0 and 1, then the trajectory will move from ψ_j to ψ_k.

Each trajectory is required to obey energy conservation, so the change in electronic energy following a hop must be compensated by adjusting the nuclear momenta accordingly. Typically, momenta are rescaled in the direction of the derivative couplings, $\mathbf{d}_{jk}$. In some cases, a hop is randomly selected which cannot occur without violating energy conservation. These "frustrated" hops are not allowed and in some schemes the nuclear velocity is reversed after a frustrated hop.

As seen in equations (30) and (31), the couplings between the states can be represented (and calculated) in two ways. In equation (30), time derivative couplings, $\left\langle \psi_j \middle| \frac{\partial}{\partial t} \psi_k \right\rangle$ are used which depend on the derivative of the adiabatic states with respect to time. In equation (31), an equivalent form uses the NACMEs, $\mathbf{d}_{jk}$, and nuclear velocities, $\frac{\partial \mathbf{R}}{\partial t}$. Depending on the electronic structure method used to determine the adiabatic surfaces, analytical calculations for the $\mathbf{d}_{jk}$ may be available. For methods where analytical $\mathbf{d}_{jk}$ are not available it is still possible to obtain the time derivative couplings using a finite difference approximation with wavefunction overlaps between the adiabatic surfaces at different times[30]:

$$\left\langle \psi_j \middle| \frac{\partial}{\partial t} \psi_k \right\rangle \approx \frac{1}{2\Delta t}\left[\left\langle \psi_j\left(t - \frac{\Delta t}{2}\right) \middle| \psi_k\left(t + \frac{\Delta t}{2}\right)\right\rangle - \left\langle \psi_j\left(t + \frac{\Delta t}{2}\right) \middle| \psi_k\left(t - \frac{\Delta t}{2}\right)\right\rangle\right] \tag{36}$$

By running simulations with large numbers of trajectories, the surface hopping method tries to capture the behavior of a fully quantum molecular system by averaging over the trajectories. In this manner the excited state lifetimes, quantum yields, and dynamic properties of a reaction can be obtained.

Thesis Organization

The chapters in this thesis include both published (Chapters 2-5) and unpublished (Chapters 6-7) articles. Chapters 2 and 3 are studies of the adsorption of S on Cu clusters of varying sizes using DFT. Convergence of the binding energy with respect to cluster size is examined. Chapter 4 is an investigation of the potential energy curves of the lowest lying singlet states of C_2. The study applies a method to approximate the full CI energy: CEEIS, as well as several additional corrections to achieve near spectroscopic accuracy. Chapters 5 and 6 introduce and evaluate a new methodology for approximating CI energies: CEEMBE, with applications to F_2 and ozone. Finally, Chapter 7 describes the implementation and application of spin-flip TDDFT as the electronic structure method for nonadiabatic dynamics.

References

(1) Schrödinger, E. *Phys. Rev.* **1926**, *28* (6), 1049–1070.

(2) Schrödinger, E. *Naturwissenschaften* **1926**, *14* (28), 664–666.

(3) Schrödinger, E. *Ann. Phys.* **1926**, *385* (13), 437–490.

(4) Schrödinger, E. *Ann. Phys.* **1926**, *384* (6), 489–527.

(5) Schrödinger, E. *Ann. Phys.* **1926**, *384* (4), 361–376.

(6) Schrödinger, E. *Ann. Phys.* **1926**, *384* (8), 734–756.

(7) Born, M.; Oppenheimer, R. *Ann. Phys.* **1927**, *389* (20), 457–484.

(8) Hartree, D. R. *Math. Proc. Camb. Philos. Soc.* **1928**, *24* (01), 89.

(9) Hartree, D. R. *Math. Proc. Camb. Philos. Soc.* **1928**, *24* (01), 111.

(10) Fock, V. *Z. Für Phys.* **1930**, *61* (1–2), 126–148.

(11) Fock, V. *Z. Für Phys.* **1930**, *62* (11–12), 795–805.

(12) Slater, J. C. *Phys. Rev.* **1929**, *34* (10), 1293–1322.

(13) Roothaan, C. C. J. *Rev. Mod. Phys.* **1951**, *23* (2), 69–89.

(14) Hall, G. G. *Proc. R. Soc. Lond. Math. Phys. Eng. Sci.* **1951**, *205* (1083), 541–552.

(15) Hylleraas, E. A.; Undheim, B. *Z. Für Phys.* **1930**, *65* (11–12), 759–772.

(16) MacDonald, J. K. L. *Phys. Rev.* **1933**, *43* (10), 830–833.

(17) Roos, B. O.; Taylor, P. R.; Si, P. E.; others. *Chem. Phys.* **1980**, *48* (2), 157–173.

(18) Ruedenberg, K.; Schmidt, M. W.; Gilbert, M. M.; Elbert, S. T. *Chem. Phys.* **1982**, *71* (1), 41–49.

(19) Hohenberg, P.; Kohn, W. *Phys. Rev.* **1964**, *136* (3B), B864–B871.

(20) Kohn, W.; Sham, L. J. *Phys. Rev.* **1965**, *140* (4A), A1133–A1138.

(21) Runge, E.; Gross, E. K. U. *Phys. Rev. Lett.* **1984**, *52* (12), 997–1000.

(22) Casida, M. E. In *Recent Advances in Density Functional Methods (Part 1)*; 1995; pp 155–192.

(23) Tamm, Igor. *J Phys USSR* **1945**, *9* (449).

(24) Hirata, S.; Head-Gordon, M. *Chem. Phys. Lett.* **1999**, *314* (3–4), 291–299.

(25) Levine, B. G.; Ko, C.; Quenneville, J.; MartÍnez, T. J. *Mol. Phys.* **2006**, *104* (5–7), 1039–1051.

(26) Gozem, S.; Melaccio, F.; Valentini, A.; Filatov, M.; Huix-Rotllant, M.; Ferré, N.; Frutos, L. M.; Angeli, C.; Krylov, A. I.; Granovsky, A. A.; Lindh, R.; Olivucci, M. *J. Chem. Theory Comput.* **2014**, *10* (8), 3074–3084.

(27) Shao, Y.; Head-Gordon, M.; Krylov, A. I. *J. Chem. Phys.* **2003**, *118* (11), 4807–4818.

(28) Tully, J. C.; Preston, R. K. *J. Chem. Phys.* **1971**, *55* (2), 562–572.

(29) Tully, J. C. *J. Chem. Phys.* **1990**, *93* (2), 1061–1071.

(30) Hammes-Schiffer, Sharon; Tully, J. C. *J. Chem. Phys.* **1994**, *101* (6), 4657–4667.

CHAPTER 2. SIZE DEPENDENCE OF S-BONDING ON (111) FACETS OF CU NANOCLUSTERS

A paper published in the *Journal of Physical Chemistry C*, 2016, 120(19), 10268-10274

Jeffery S. Boschen, Jiyoung Lee, Theresa L. Windus, James W. Evans, and Da-Jiang Liu

JSB and JL were responsible for the atomic orbital basis results, DJL contributed the plane wave basis results.

Abstract

We demonstrate a strong damped oscillatory size dependence of the adsorption energy for sulfur on the (111) facets of tetrahedral Cu nanoclusters up to sizes of ~300 atoms. This behavior reflects quantum size effects. Consistent results are obtained from density functional theory analyses utilizing either atomic orbital or plane-wave bases and using the same Perdew–Burke–Ernzerhof functional. Behavior is interpreted via molecular orbitals (MO), density of states (DOS), and crystal orbital Hamilton population (COHP) analyses.

1 Introduction

There exist extensive analyses of the size dependence of adsorption properties for CO and other species on selected subsequences of metal nanoclusters.(1, 2) A particular advantage of studies for finite clusters with small to medium sizes is that there is considerable flexibility in available electronic structure methods: from density functional theory (DFT) analysis with atomic orbital basis expansions, plane-wave basis sets, or real-space grid methods,(1-3) to higher-level quantum chemistry methods.(4) These cluster studies are often focused on extrapolation of behavior determined from precise calculations for smaller sizes [of $n = O(10^1)$ to $O(10^2)$ atoms], not just to the larger-size regime common for supported catalytic nanoparticles [with $n = O(10^2)$ to $O(10^4)$], but beyond to the limit corresponding to extended surfaces [with $n \rightarrow \infty$]. This goal has prompted interest in identifying simple scaling rules for the variation of intrinsic properties, $A(n)$, in the larger size regime. These sometimes have the form $A(n) \approx A(\infty) + cn^{-1/3}$ based on surface area versus volume contributions and associated thermodynamic considerations.(1) However, more complex behavior might be anticipated in some systems even for sizes up to $n = O(10^2)$.(2, 5)

Various adsorbate-cluster systems have been studied previously, including: CO adsorption on (111) facets of Pd(1, 6-8) and Pt,(1, 9, 10) O adsorption on (111) facets of Pt,(11) CO and O adsorption on (111) facets of Au(2, 5, 12) and Pt,(3) CO adsorption on (111) facets of Cu,(4) and S adsorption on various facets of Ni.(13) These studies often choose sequences of octahedral or cuboctahedral clusters. Our focus in this work is on S adsorption on (111) facets of Cu, motivated in part by recent experiments for S/Cu(111).(14-17) These experiments are in turn motivated by the potential for S to induce surface reconstruction and to form metal–S complexes, which can facilitate rearrangement or destabilization of metal nanostructures by providing alternative mass transport pathways.(15, 17) (As an aside, interest exists in the interaction of sulfur and organosulfur with coinage metals more generally. In addition to reconstruction, complexation, and destabilization, which occur also for Ag and Au,(18-22) S can act as a promoter or poison in catalysis,(23) and the S–metal bond also plays a key role in anchoring various molecular ligands particularly on Au(111) surfaces.(24, 25)) In our study, we focus on characterization of S adsorption for sequences of tetrahedral (T_d) Cu clusters with exposed (111) facets, for which one might anticipate rapid convergence in adsorption behavior to that for extended Cu(111) surfaces, if interactions between the adsorbate and the metal surface are short-ranged.

The majority of DFT studies of adsorption on clusters have utilized localized orbital-based DFT,(1, 6, 7, 9-11, 13) but some have instead used plane-wave DFT with periodic boundary conditions (with one cluster-plus-adsorbate system included in each unit cell).(12) The former has a potential advantage in providing and elucidating a localized orbital based picture of bonding. In this work, we will implement and compare both approaches utilizing the same Perdew–Burke–Ernzerhof (PBE) functional.(26) Our results for adsorption energies from both approaches are quite consistent with each other. There are complications for either method with respect to extrapolation of behavior to infinite cluster size, as discussed below. However, this limiting behavior can be accessed independently within the plane-wave DFT approach from calculations using slab rather than cluster geometries for increasing lateral unit cell sizes and appropriately averaging over slab thicknesses to eliminate quantum size effects (see below).(27)

A key observation of our analysis is a particularly strong size dependence of the adsorption energy of S on the (111) facets of tetrahedral Cu clusters. Specifically, we find a nonmonotonic damped oscillatory variation, which dominates over any $n^{-1/3}$ type scaling behavior, at least for sizes up to $n \approx 300$ atoms. For metal thin films and other nanostructures, it has long been recognized that effectively constraining nearly free electrons in a finite nanoscale region introduces large variations in energies and other properties.(28-31) The effect is quantum in nature and thus is commonly referred to as quantum size effects (QSE). Associated behavior cannot be described by any simple scaling rule, but it can be effectively captured even in free electron models and jellium models. As an aside, although the strong size dependence due to

QSE complicates extrapolation of energetics for bulk systems, it may open possibilities for tuning catalytic and other properties of nanoclusters. Indeed, QSE-modified adsorption properties(2) and catalytic properties(32) of metal nanoclusters have been observed in previous studies.

Another component of our study is to provide chemical insight into the binding strength and variation of S on the Cu nanoclusters. For DFT analysis based on localized orbital basis expansions, one can extract and identify molecular orbitals (MOs) characterizing bonding for smaller Cu clusters, but not necessarily for larger clusters. For plane-wave based DFT, this type of interpretation is not straightforward. However, using crystal orbital Hamilton population (COHP) analysis,(33) we are able to identify both bonding and antibonding MOs from such plane-wave based analyses. There is no one-to-one correspondence between the MOs from finite cluster calculations versus slab geometry calculations. However, by combining several MOs from the cluster calculations for medium to large clusters, a correspondence can be established. This indicates that although the convergence in energetics is slow, a qualitative picture that describes bonding of S and the Cu(111) surface emerges even for relatively small clusters.

We also find that the T_d Cu_{20}, which corresponds to a electronic closed-shell “magic” cluster,(34) is generally not favorable for S adsorption. Furthermore, the differences in adsorption energies on different sites are particularly pronounced and have a high correlation with the shapes of the highest occupied MO (HOMO) and lowest unoccupied MO (LUMO).

The paper is organized as follows. In Section 2, computational details are described for DFT calculations using both an atomic basis set (NWChem(35) and GAMESS(36, 37)) and a plane-wave basis set (VASP(38, 39)). In Section 3, basic results for the S adsorption energy versus Cu cluster size are presented for two types of 3-fold hollow (3fh) sites on (111) facets.

With regard to cluster geometry, we focus on the Cu(111) surface and consider various truncations of tetrahedral clusters. Results for S adsorption on octahedral clusters are also given. A comparison of energies from different DFT methods and functionals is provided for selected cases. In addition, the site projected density of states (SDOS) of the adsorbed S and crystal orbital Hamilton population (COHP) analysis of its interactions with the Cu cluster are given in Section 3.2. The mechanism of the size dependence is analyzed in Section 4. Further discussion and conclusions are given in Section 5.

2 Computational Details: DFT Analysis via NWChem, GAMESS, and VASP

Plane-wave DFT calculations are performed using the VASP code(38, 39) (version 5.3.5) with the projector augmented-wave (PAW)(40, 41) method. The energy cutoff for plane-wave basis set is 280 eV. For cluster calculations, Gaussian smearing with σ = 0.2 eV is used as the default. For periodic slab calculations, the Methfessel–Paxton(42) method with the same σ value is used as the default. All calculations are conducted without spin polarization, except for analysis of the S_2 dimer in vacuum which provides a reference energy for the S species. In Appendix A, we also show some results from spin polarized calculations.

For cluster calculations with VASP, each cluster is contained in a supercell which is repeated with a simple cubic periodicity. The size of the supercell is so chosen that the closest separation between the edges of periodic images of the cluster is at least 12 Å. Because the periodicity has no physical meaning, a (1 × 1 × 1) or Γ point only *k*-points grid is used. For a slab geometry, the (111) surface is modeled by supercells with shape and size so chosen that along the z direction, the slabs are separated by 12 Å, whereas perpendicular to the z direction, the computational supercell vectors correspond to various multiples of those for the primitive unit cell of the (111) surface.

Our primary interest here is in characterizing and understanding the variation of the S-metal interaction with the size of the cluster, rather than in modeling any particular physical realization of nanocluster geometries (e.g., for supported versus unsupported cases). To facilitate more extensive analysis with respect to both the size range of the clusters and also with respect to different methodologies, the relative positions of atoms in the Cu clusters are fixed at their bulk positions. In other words, the clusters can be thought of as cut from a bulk face-centered cubic (fcc) solid with no relaxation allowed. The lattice constant used is 3.641 Å, obtained from bulk calculations, which corresponded to 2.574 Å for nearest-neighbor Cu–Cu distance. The S atom is allowed to relax upon the frozen substrate, with energy minimization under the criterion that the maximal force is less than 0.02 eV/Å. In Appendix A, we show results from calculations with fully relaxed clusters.

The adsorption energy of S on a cluster is calculated using:

$$E_b(\mathrm{S}) = E(\mathrm{S} + \mathrm{cluster}) - E(\mathrm{cluster}) - E(\mathrm{S}_2, \mathrm{gas})/2$$

where $E(\mathrm{S} + \mathrm{cluster})$ is the total energy of the cluster plus S adsorbate system, $E(\mathrm{cluster})$ is the energy of the cluster itself, and $E(\mathrm{S}_2, \mathrm{gas})$ is the energy of a S_2 molecule (spin-polarized).

Additional plane-wave VASP-based analyses includes calculation of the site-projected density of states (DOS). Also, the crystal orbital Hamilton population (COHP) analysis is applied to gain some understanding of bond strengths.(33)

DFT calculations with an atomic basis set are performed with NWChem(35) and GAMESS(36, 37) using PBE(26) and PBE0(43) functionals. The basis sets used are Los Alamos National Laboratory double-ζ (LANL2DZ) with effective core potentials (ECP's)(44-46) for Cu and 6-311++G(d,p) for S.(47-49) All basis sets are taken from the EMSL basis set exchange Web site.(50) The geometries for the calculations were those from the planewave DFT calculations. The multiplicity of a cluster is either a singlet for an even number of Cu or a doublet for an odd number. The S_2 dimer energy was calculated in a triplet state with a restricted open-shell. Molecular orbitals were analyzed using MacMolplt.(51)

3 Results for Adsorption Energy and Bonding Characterization

3.1 Variation of Adsorption Energy with Cluster Size

Clusters with tetrahedral (T_d) symmetry are a natural choice for the study of adsorption on (111) surfaces. Figure 1(a−d) shows several examples of the T_d clusters considered. One subclass denoted by m0 corresponds to perfect tetrahedra bounded by four equilateral triangular surfaces. Another class m1 represents T_d clusters with the apex atom at the bottom removed. Clusters with an atom removed from each vertex (a total of four removed), are denoted by m4, and clusters with 4 atoms removed from each vertex (a total of 16 removed) are denoted by m16. Below, $N_{\mathrm{Cu}} = n$ will denote the number of Cu atoms in the cluster.

We then calculate the adsorption energy of S on clusters of various sizes in these classes. For extended (111) surfaces of fcc crystals, there are two types of 3-fold hollow (3fh) sites. The first type corresponds to a site where atoms would reside when extending the bulk fcc lattice, and is thus named fcc site. Directly beneath an fcc site, one finds a hollow site in the second layer, and an atom in the third layer. The second type has an atom directly beneath it in the second layer, and a hollow site in the third layer. They are called hcp site, because the top three layers mimic the stacking sequence of hexagonal close packed crystals.

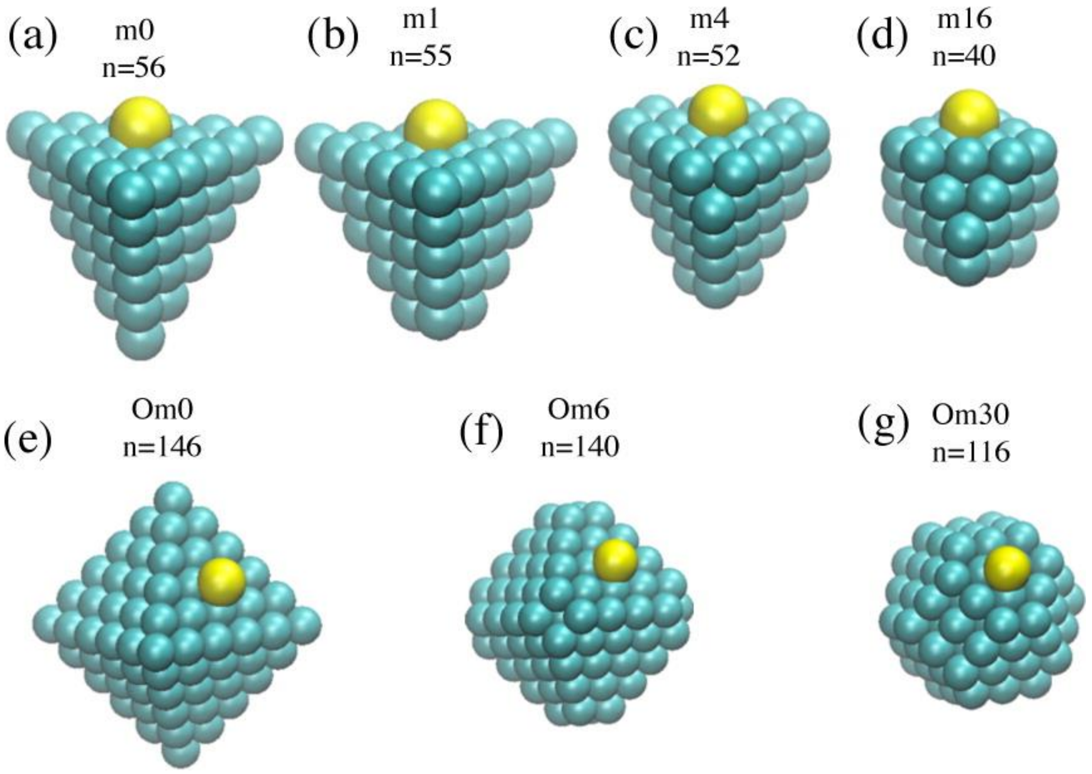

Figure 1. Top panels: Various classes of tetrahedral (T_d) clusters. (a) Perfect tetrahedron (class m0), (b) tetrahedron with the bottom apex atom removed (class m1), (c) with all four apex atoms removed (class m4), and (d) with four atoms from each vertex removed (class m16). Bottom panels: clusters with octahedral (O_h) symmetry: (e) perfect octahedron (class Om0), (f) octahedron with the apex atom from each vertex removed (class Om6), and (g) four atoms from each vertex removed (class Om30).

We first consider S adsorption at fcc sites. Note that for m0 clusters, only in cases where the number of layers is a multiple of three (corresponding to n = 10, 56, 165, ...) does the center of each face correspond to an fcc site. Figure 2 shows results from our plane-wave DFT analysis using VASP for the adsorption energy E_b on fcc sites that are closest to the center for various clusters. Very large variations in E_b are observed for all types of clusters. The variation has a damped oscillatory form and with near constant period when plotted against $n^{1/3}$ which reflects the linear dimension of the cluster recalling that $n = N_{Cu}$ is the number of Cu atoms in the cluster. The oscillation amplitude remains significant (around 0.3 eV) even for clusters as large as 200 atoms.

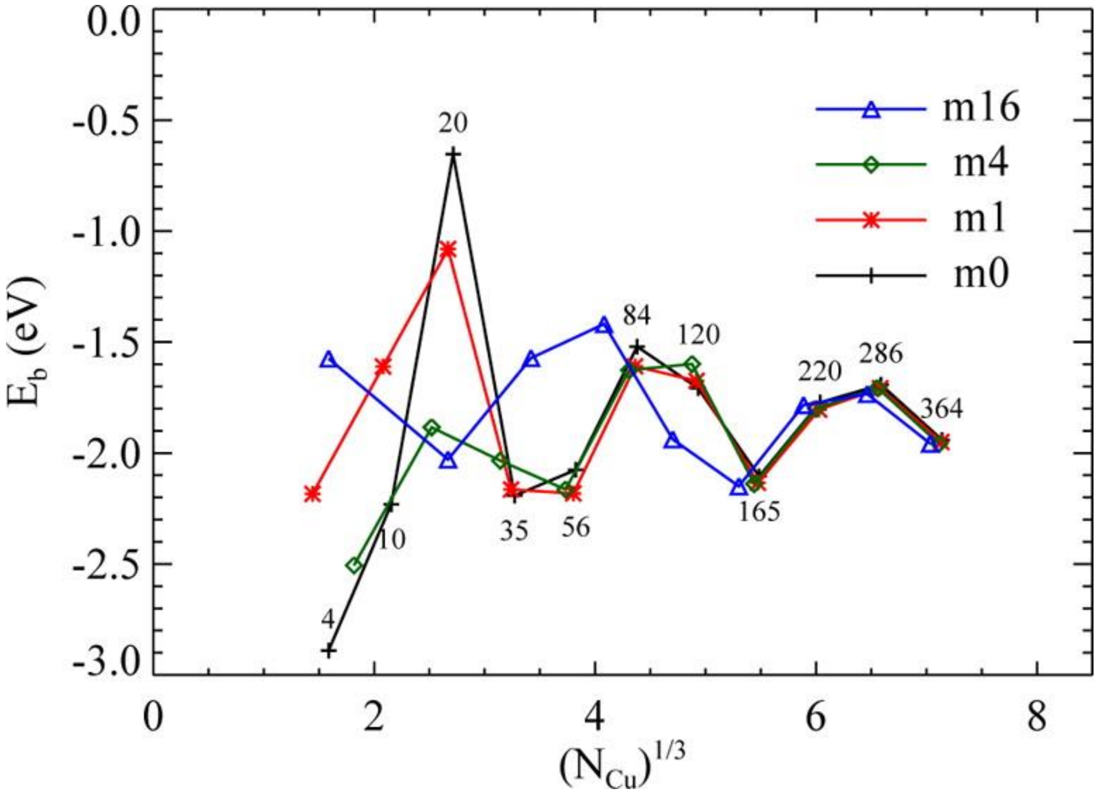

Figure 2. Plane-wave DFT results for the adsorption energy of S on Cu clusters on the fcc site closest to the center of a cluster of various sizes and shapes. Lines with various colors connects clusters of various classes shown in Figure 1.

Another observation from Figure 2 is that for clusters that are smaller than $n = 20$, which consists of four layers of Cu for the m0 cluster, just removing one apex atom from the bottom of the cluster significantly affects the adsorption energy. This suggests that the electronic interaction between S and the cluster is highly nonlocal. Only for clusters that are larger than 200 does the choice of truncation at the cluster corners far away from the S atoms have a minimal effect on the adsorption energy.

There are some advantages in using atomic versus plane-wave basis sets for cluster calculations, since the latter suffers from several artifacts, such as periodicity, thermal smearing of the occupancy function, and so forth. Therefore, we also perform multiple sets of calculations with an atomic basis set using NWChem and GAMESS. For these sets of calculation, we consider only m0 clusters (untruncated tetrahedrons). For clusters with $n = 4$, 35, 120, the adsorption sites at the facet centers are hcp sites. For all other clusters, the adsorption site is the fcc site at or closest to the center. Results for the S adsorption energy from these analyses are compared with each other and with the results obtained from the plane-wave analysis in Figure 3.

The results for adsorption energy from these various methods of calculation generally agree quite well with each other. Not surprisingly, GAMESS-PBE and NWChem-PBE calculations agree with each other perfectly because they use both the same basis set and functionals. Results from atomic basis sets for E_b generally predict stronger binding than the plane-wave VASP results. We have also performed calculations with the hybrid PBE0 functional(43) using NWChem. Results are generally consistent with the PBE functional, with slightly stronger binding for $n = 4$, 10, and 84, and weaker binding for $n = 20$, 35, and 56.

All adsorption energies reported in this paper neglect zero point energies (ZPE). Using frozen substrates, we estimate ZPE to be 0.041, 0.036, 0.033, 0.041, and 0.040 eV for the first five data points in Figure 3, which shows a slight compensatory effect in the sense that ZPE is higher in clusters with stronger bonding. However, it is insignificant compared with the overall oscillations in E_b.

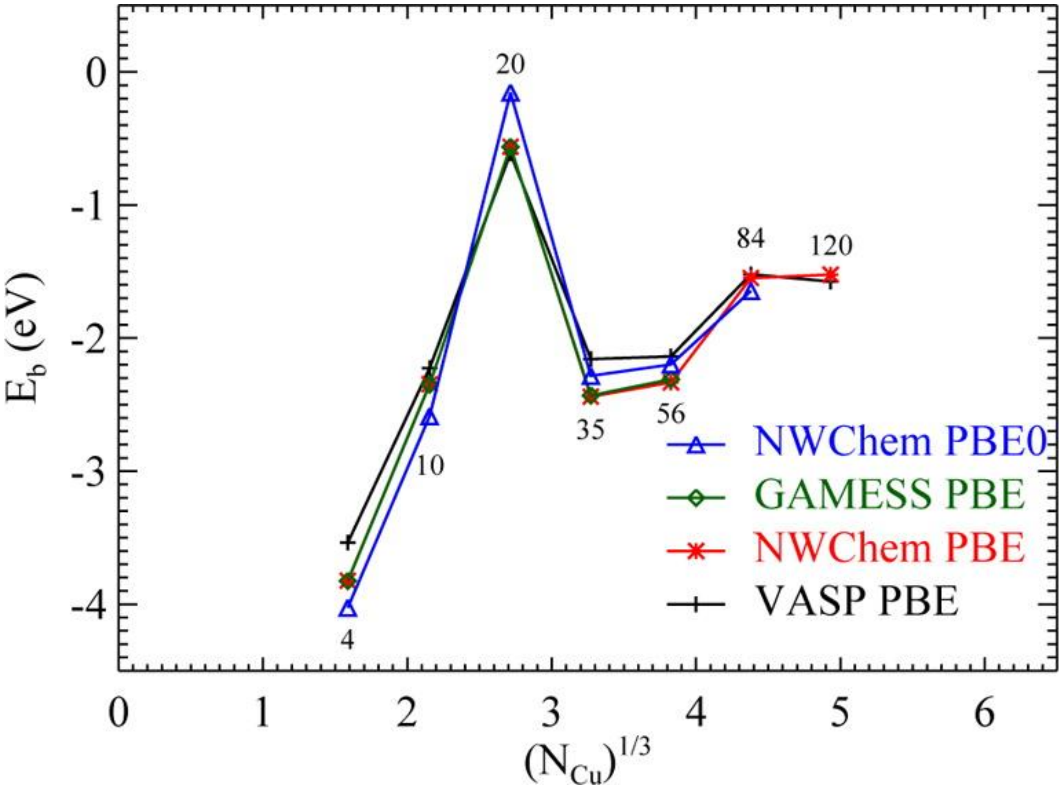

Figure 3. Comparison of the size dependence of E_b on 3fh sites on the m0 clusters calculated using different methods.

Finally, for comparison with the above analysis of S adsorption on clusters with tetrahedral symmetry, we more briefly consider the case of octahedral symmetry restricting our considerations to plane-wave DFT analysis. Analogous to above, we consider different classes of geometries corresponding to a perfect octahedron (Om0), clusters with one Cu atoms removed from each vertex (Om6), and clusters with 5 Cu atoms removed from each vertex (Om30).

See Figure 1. Results for the S adsorption energies are shown in Figure 4. For untruncated Om0 clusters, compared with results for untruncated tetrahedral clusters, the variations for small to medium clusters are not as dramatic. With the exception of the Om6 *n* = 13 cluster, no exceptionally large deviation from the bulk value are observed. On the other hand, the expectation that more compact clusters converge faster is not universally true. There is still a variance of 0.4 eV for Om30 clusters, which are the most compact, for *n* > 200. This indicates that the oscillation is intrinsic regardless of the geometric shape of the cluster.

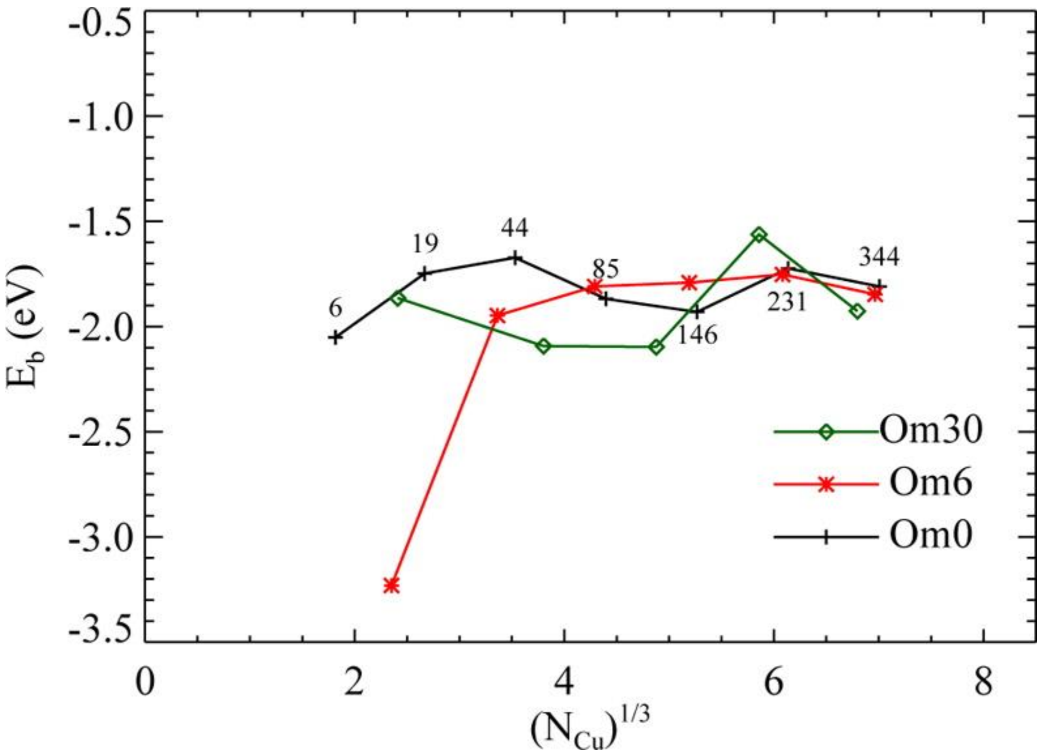

Figure 4. Adsorption energy of S on octahedral Cu clusters on the fcc site closest to the center of a cluster of various sizes and shapes. Lines connect clusters of various classes shown in Figure 1.

3.2 DOS, COHP, and MO Analysis

Figure 5 shows the site-projected density of states (SDOS) of the S adatom on various m0 clusters from plane-wave DFT VASP calculations. To avoid complications arising from different symmetries, we focus on clusters for which the adsorption site at the center of the facets are 3fh sites. Specifically, these include hcp sites for *n* = 4, 35, 120, and fcc sites for *n* = 10, 56, 165. Plots are shifted vertically so that various SDOS curves are distinguishable, and the energies are shifted according to the Fermi energy E_F. Also plotted at the bottom is the SDOS of the S adatom calculated using the slab geometry. Not shown on this plot is a very low lying peak centered around 12.7 eV below the Fermi level. Two distinct regions of significant SDOS can be observed. The first region is between 3 and 5 eV below E_F. The second region is closer to the Fermi level. Significant size variations persist for all clusters shown in this plot. Although some degree of convergence can be argued to emerge for the lower region, the region closer to the Fermi level shows no sign of convergence as cluster size increases.

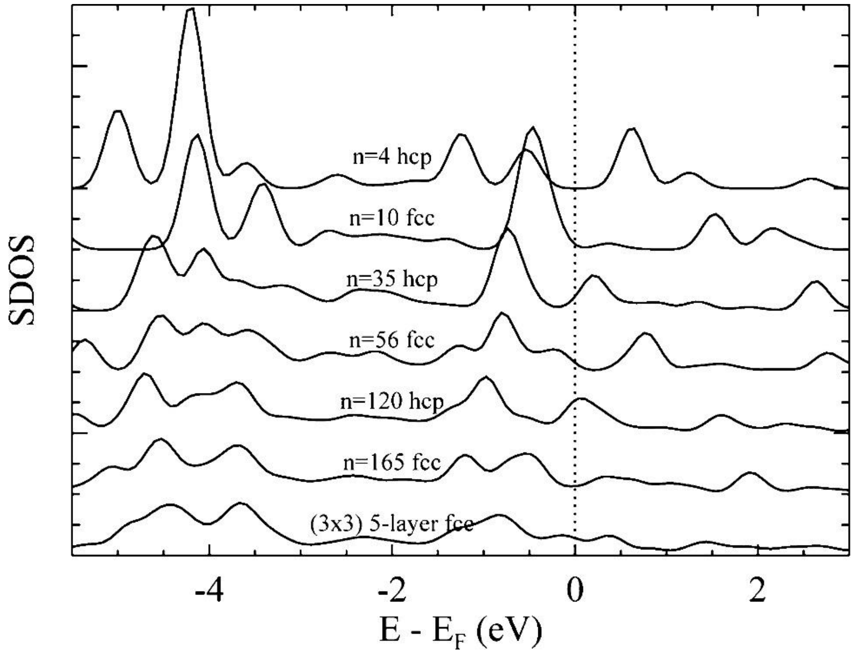

Figure 5. Site projected density of states (SDOS) of the S on various clusters and a slab.

For plane-wave DFT calculations, the nature of the binding of S with the cluster can be more clearly demonstrated by crystal orbital Hamilton population (COHP) analysis.(33) Results of a COHP analysis for S on the same set of clusters analyzed in Figure 5 are plotted in Figure 6. Negative (positive) COHP values, corresponding to higher (lower) portions of curves in Figure 6, suggest bonding (antibonding) interactions. It is clear from this analysis that the orbitals around −4.5 eV below E_F are mostly bonding, whereas the orbitals close to E_F are mostly antibonding. Similar to the SDOS analysis, we find slow convergence of the bonding orbitals with increasing cluster size, and no sign of convergence for the antibonding orbitals.

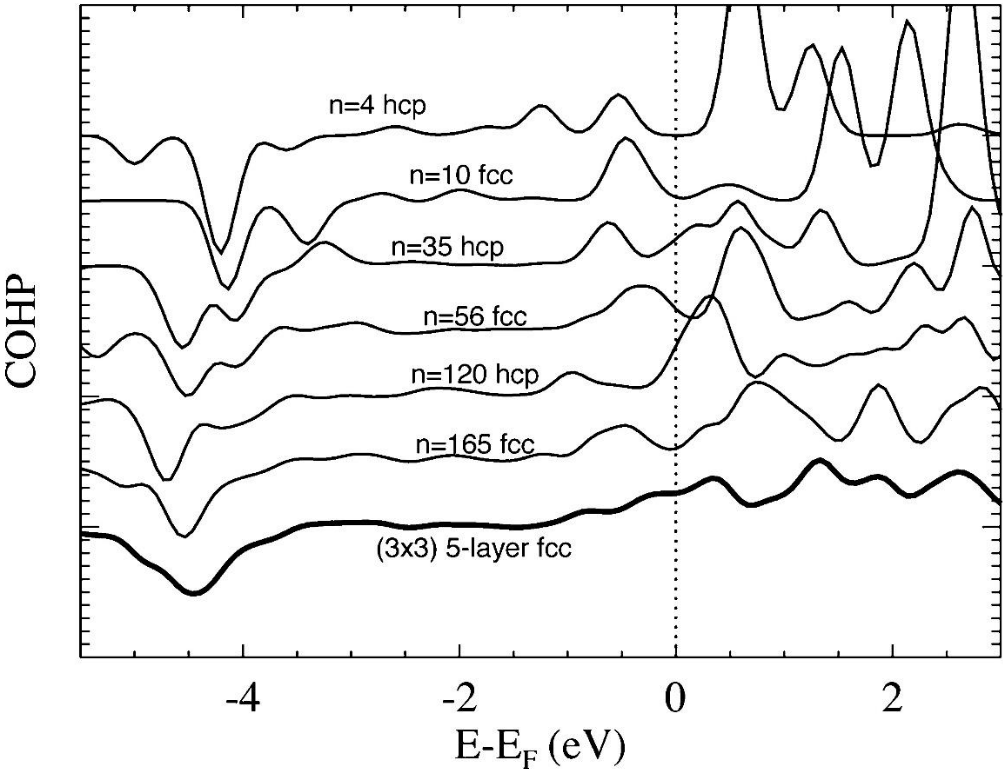

Figure 6. COHP of S with the three closest Cu atoms on tetrahedral clusters of various sizes, and on a five layer slab in a (3 × 3) supercell.

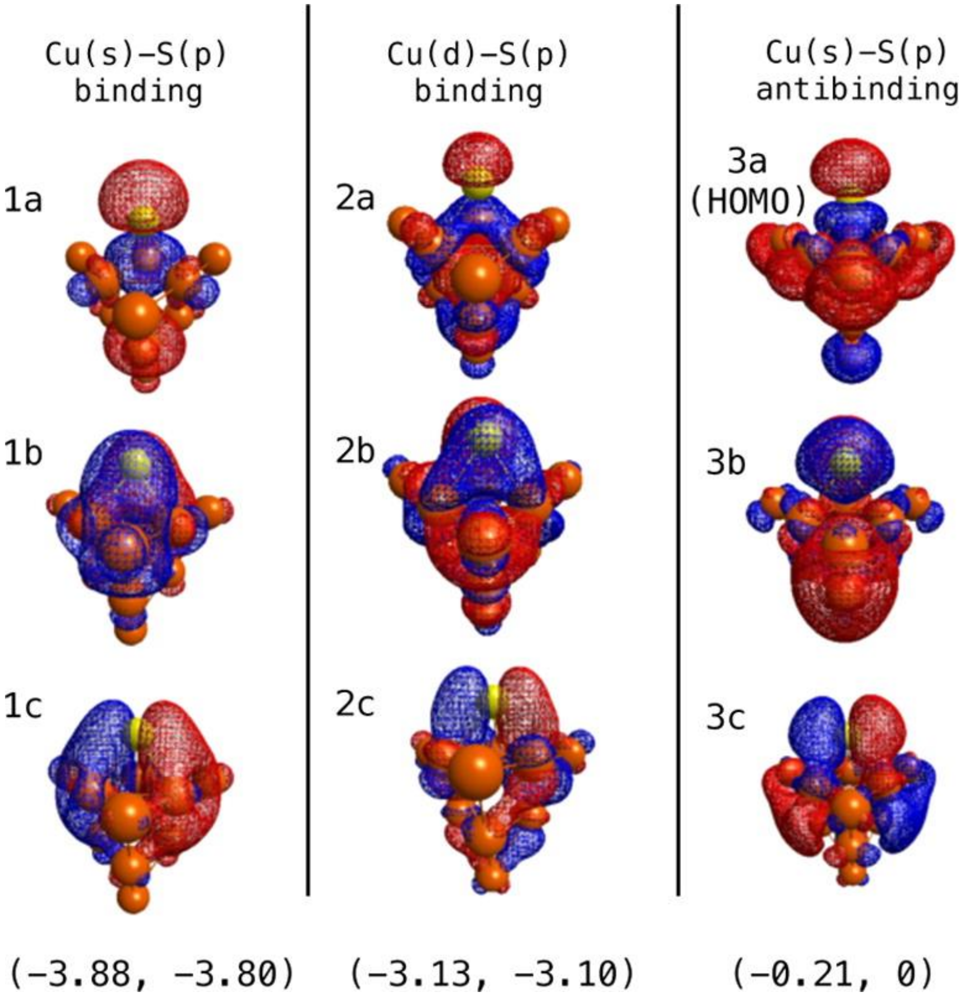

Figure 7. Molecular orbitals (MOs) that contribute the most to interactions between S and Cu on Cu_{10} clusters, using GAMESS and MacMolPlt. The energies of MOs relative to the HOMO energy are indicated below the orbitals.

Figure 7 shows three families of MOs that represent the three most visible peaks for S on the fcc site of Cu_{10} clusters, for both SDOS and COHP. The first set of three MOs have energy 3.88 to 3.80 eV below the HOMO energy. The interactions are binding and can be mostly characterized by Cu(s)–S(p). The second set of MOs are at 3.10 to 3.13 eV below the HOMO energy. They are also attractive and can be mostly characterized by Cu(d)–S(p). The third set is antibonding, including the HOMO and two other MO that lies 0.21 eV below the HOMO energy. They can be mostly characterized by Cu(s)–S(p). The character of some of the MOs can be more easily seen if one views the Cu cluster as a whole. If one compares 1a with 3a, the phases of the S p_z orbital are the same, whereas the phases of the orbitals encompassing the Cu cluster are reversed. Similar observations can be made for 1b and 3b as well as 1c and 3c. Thus, the Cu(d)–S(p) couplings are mostly bonding, whereas Cu(s) and S(p) couplings contribute both to bonding and antibonding.

4 Relationship of the S Binding Energy and Shell-Structure of Cu Clusters

The oscillatory behavior in E_b is most likely due to the quantum confinement in nanoclusters.(28, 29) Previous studies related to QSE generally focused on the energetics and stabilities of pure metal clusters(28, 29) or thin films.(30, 31) DFT studies of a deformable jellium model by Reimann et al.(34) found the first shells at n = 2, 8, 20, 40, 70, and 112 for clusters with tetrahedral deformations. For univalent metal clusters such as Cu, tetrahedral clusters of those sizes are expected to have a closed-shell electronic structure, as far as the s electron is concerned. Perfect tetrahedrons, which correspond to the m0 class of clusters in Figure 1, can be considered to exhibit geometric "magic" numbers, n = 4, 10, 20, 35, 56, ... The case of n = 20 is especially interesting, as it is a magic number for both electronic and geometric structures.

As Figure 2 shows, adsorption of S on the fcc site near the center of the face of a n = 20 tetrahedral cluster is especially weak. This is perhaps not surprising, considering that it is often argued that the closed-shell clusters should have a low chemical reactivity. This is analogous to the low reactivity of noble gases, their atomic counterparts. Indeed, Au_{20} clusters are found(52) to possess a tetrahedral structure, with an exceptionally large gap between the highest occupied molecular orbital (HOMO) and lowest unoccupied molecular orbital (LUMO). We find a similarly large HUMO-LUMO gap (1.22 eV from VASP, 1.34 eV from NWChem) for the tetragonal Cu_{20}cluster. The next largest gap for the T_d m0 class clusters with $10 < n < 364$ is about five times smaller at $n = 120$ (0.27 eV from VASP, 0.24 eV from NWChem). As far as we know, no previous experimental or theoretical study(53, 54) has shown the tetrahedral Cu_{20} being more stable than other competing structures. On the other hand, Ag nanocrystals have been shown to form spontaneously as stacking-fault tetrahedrons in Ag(111) films.(55)

To obtain a more comprehensive picture of the interaction between S and the Cu_{20} tetrahedral cluster, we explore the adsorption energy as a function of adsorption site location on the (111) facet. Results are shown in Figure 8a. There are two types of hcp sites: the ones closer to the center (hcp) and the ones near the corners (hcp1). For fcc sites, only the ones near the center (fcc) are 3-fold coordinated. Moving further away from the center results in fcc sites that are on the edge. Adsorption energies on all sites are less negative than the converged large cluster limit (around −1.75 eV). This is consistent with the conjecture of lower reactivity of closed-shell systems. However, the fcc sites in the middle are exceptionally unstable sites. In fact, the fcc site on the edge is more favorable toward S adsorption, in contrast to the general picture that S prefer higher coordinated adsorption sites. Further insights can be obtained from a molecular orbital analysis. Figure 8b shows the isodensity plot for the HOMO and LUMO of the clean Cu_{20} cluster and the cluster with S on the fcc and hcp sites near the center. For the clean cluster, the electron density of the HOMO is concentrated near the edges, and the LUMO density is concentrated at the corners. The HOMO and LUMO of the S-adsorbed clusters reflect coupling of the $p_{x,y}$ and $p_z$orbitals and the HOMO of the Cu_{20} cluster. The fcc site is close to a nodal point of both the HOMO and LUMO of the clean cluster, whereas the other adsorption sites are located in regions of higher electron density. Thus, the shape of the frontier orbitals of the clean cluster correlates with the strength of the binding.

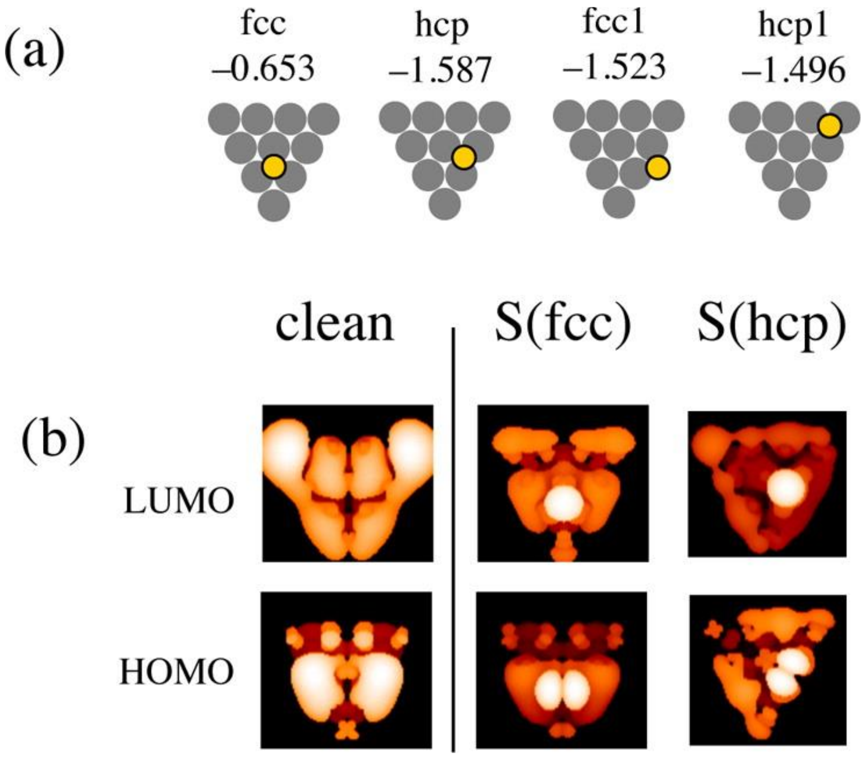

Figure 8. (a) E_b(S) (in eV) for S on various adsorption sites of the tetrahedral Cu_{20} cluster. (b) HOMO and LUMO of the clean Cu_{20} cluster, with a S on the fcc and hcp site near the center.

5 Discussions and Conclusions

We systematically calculate the interaction of S on 3fh sites of Cu clusters with tetrahedral geometry of various sizes and find strong oscillation in the adsorption energy, persisting to the largest clusters calculated (up to 364 atoms). There is good agreement between results obtained from plane-wave and atomic orbital basis set calculations. Strong oscillations in the adsorption energy have their origin in the shell structure of the Cu cluster due to quantum confinement. Furthermore, for the “magic” Cu_{20} cluster with closed-shell electronic structure, a large HOMO–LUMO gap gives rise to both an overall weaker binding, and particularly weak binding at certain 3fh sites near the (111) facet center.

Although extensive DFT studies of chemisorption on metal clusters exist, results presented here are still somewhat surprising. It is generally expected that quantum size effects (QSE) for chemisorption are significant when the energy levels are discrete with gaps on the order of several electronvolts near the Fermi level; therefore, they should diminish for clusters on the order of several hundred atoms.(2) However, we find that at least for the particular system of S on tetrahedral Cu clusters, the expectation of reaching thermodynamic scaling regime for clusters of a few hundred atoms is not justified. Using the more compact octahedral clusters reduces the variation with size to some extent, but significant oscillatory behavior still exists. This variation is not due to the discrete nature of MOs in finite clusters, which is a narrower interpretation of QSE. As shown in Section 3.2, a DOS and COHP description of the interaction between S and Cu clusters already emerges for clusters of 35 atoms. Larsen et al.(5) calculated and analyzed the electronic structure of Au clusters up to 200 atoms using real-space DFT with optimized structures (up to 60 with DFT, and up to 200 with effective medium theory). They also calculated the chemisorption energy of O, F, and H/Li on cuboctahedral clusters. Results for O should be more directly comparable with S. In this analysis, adsorption on clusters with $n = 34$, 58, 92, and 138, which correspond to closed-shell magic numbers, are particularly unfavorable. Our results are consistent with their observation that closed-shell clusters are less favorable for chemisorption but also reveal much larger variation of the adsorption energy for different adsorption site locations for closed-shell clusters.

Appendix A

Effects of Cluster Relaxation and Spin Polarization.

In order to reveal the generic feature of the size dependence of S-binding, we assume that the Cu atoms are fixed at their bulk positions. There can be questions as to what extent substrate relaxation can affect the results. We also calculate the S adsorption energy $E_b(S)$ assuming the substrate cluster can fully relax, by comparing the energies of a fully relaxed S-adsorbed cluster, and a fully relaxed clean cluster. The comparison with fixed substrate is given in Figure 9.

Also the VASP results presented in the main text are obtained without spin polarization (except for the S_2 dimer). For small clusters, the ground state may have nonzero magnetic moment. Results with spin polarization are also given in Figure 9, denoted by dotted lines, for both fixed and relaxed substrate. For small clusters, there are some differences due to different spin states, but the differences are small and generally decrease as the clusters grow larger. The comparison suggests the general feature of the size dependence is very robust.

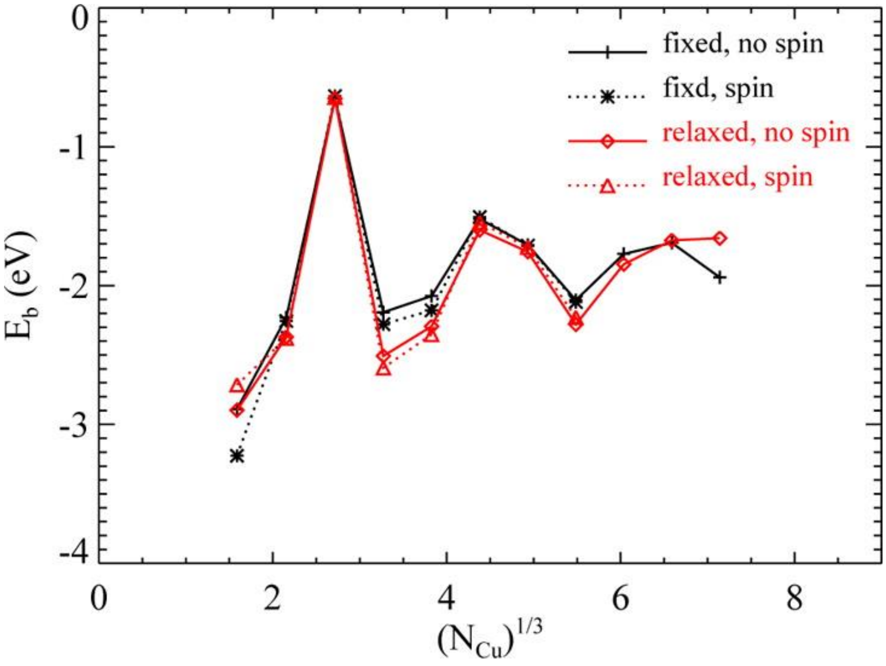

Figure 9. Comparison of the size dependence of E_b on fcc sites on the m0 tetrahedral clusters with different assumptions using plane-wave basis sets. Results with fixed substrate and no spin polarization are represented by diamonds, fixed substrate, and with spin polarization are represented by triangles, relaxed substrate with no spin polarization by pluses, and relaxed substrate with spin polarization by asterisks.

Acknowledgement

This work was supported by the U.S. Department of Energy (U.S. DOE), Office of Basic Energy Sciences, Division of Chemical Sciences, Geosciences, and Biosciences through the Ames Laboratory Chemical Physics program. We acknowledge use of NERSC computational resources. The work was performed at Ames Laboratory, which is operated for the U.S. DOE by Iowa State University under Contract No. DE-AC02-07CH11358.

References

1. Soini, T. M.; Rösch, N. Size-dependent properties of transition metal clusters: from molecules to crystals and surfaces - computational studies with the program PARAGAUSS *Phys. Chem. Chem. Phys.* **2015**, 17,28463– 28483, DOI: 10.1039/C5CP04281J

2. Kleis, J.; Greeley, J.; Romero, N. A.; Morozov, V. A.; Falsig, H.; Larsen, A. H.; Lu, J.; Mortensen, J. J.;Dułak, M.; Thygesen, K. S. Finite Size Effects in Chemical Bonding: From Small Clusters to Solids *Catal. Lett.* **2011**, 141, 1067– 1071, DOI: 10.1007/s10562-011-0632-0

3. Li, L.; Larsen, A. H.; Romero, N. A.; Morozov, V. A.; Glinsvad, C.; Abild-Pedersen, F.; Greeley, J.; Jacobsen, K. W.; Nørskov, J. K. Investigation of Catalytic Finite-Size-Effects of Platinum Metal Clusters *J. Phys. Chem. Lett.* **2013**, 4, 222– 226, DOI: 10.1021/jz3018286

4. Hu, Q.-M.; Reuter, K.; Scheffler, M. Towards an exact treatment of exchange and correlation in materials: application to the "CO adsorption puzzle" and other systems *Phys. Rev. Lett.* **2007**, 98, 176103, DOI: 10.1103/PhysRevLett.98.176103

5. Larsen, A. H.; Kleis, J.; Thygesen, K. S.; Nørskov, J. K.; Jacobsen, K. W. Electronic shell structure and chemisorption on gold nanoparticles *Phys. Rev. B: Condens. Matter Mater. Phys.* **2011**, 84, 245429, DOI: 10.1103/PhysRevB.84.245429

6. Yudanov, I. V.; Genest, A.; Schauermann, S.; Freund, H.-J.; Rösch, N. Size Dependence of the Adsorption Energy of CO on Metal Nanoparticles: A DFT Search for the Minimum Value *Nano Lett.* **2012**, 12, 2134–2139, DOI: 10.1021/nl300515z

7. Yudanov, I. V.; Metzner, M.; Genest, A.; Rösch, N. Size-Dependence of Adsorption Properties of Metal Nanoparticles: A Density Functional Study on Palladium Nanoclusters *J. Phys. Chem. C* **2008**, 112, 20269–20275, DOI: 10.1021/jp8075673

8. Yudanov, I. V.; Sahnoun, R.; Neyman, K. M.; Rösch, N. Metal nanoparticles as models of single crystal surfaces and supported catalysts: Density functional study of size effects for CO/Pd(111) *J. Chem. Phys.***2002**, 117, 9887– 9896, DOI: 10.1063/1.1516798

9. Soini, T. M.; Krüger, S.; Rösch, N. The DFT+Umol method and its application to the adsorption of CO on platinum model clusters *J. Chem. Phys.* **2014**, 140, 174709, DOI: 10.1063/1.4872037

10. Huang, Y.-W.; Lee, S.-L. Hybrid DFT and hyper-GGA DFT studies of the CO adsorption on Pt nanoclusters: Effects of the cluster size and better CO LUMO description *Chem. Phys. Lett.* **2010**, 492, 98– 102, DOI: 10.1016/j.cplett.2010.04.026

11. Jacob, T.; Muller, R. P.; Goddard, W. A., III Chemisorption of atomic oxygen on Pt(111) from DFT studies of Pt-clusters *J. Phys. Chem. B* **2003**, 107, 9465– 9476, DOI: 10.1021/jp030716r

12. Xie, Y.-P.; Gong, X.-G. First-principles studies for CO and O_2 on gold nanocluster *J. Chem. Phys.* **2010**, 132,244302, DOI: 10.1063/1.3455714

13. Ackermann, L.; Rösch, N. Chemisorption of sulfur on nickel: A study of cluster convergence in the linear combination of Gaussian-type orbitals local density functional approach *J. Chem. Phys.* **1994**, 100, 6578–6590, DOI: 10.1063/1.467067

14. Wahlström, E.; Ekvall, I.; Kihlgren, T.; Olin, H.; Lindgren, S.-Å.; Walldén, L. Low-temperature structure of S/Cu(111) *Phys. Rev. B: Condens. Matter Mater. Phys.* **2001**, 64, 155406, DOI: 10.1103/PhysRevB.64.155406

15. Ling, W. L.; Bartelt, N. C.; Pohl, K.; de la Figuera, J.; Hwang, R. Q.; McCarty, K. F. Enhanced Self-Diffusion on Cu(111) by Trace Amounts of S: Chemical-Reaction-Limited Kinetics *Phys. Rev. Lett.* **2004**, 93, 166101,DOI: 10.1103/PhysRevLett.93.166101

16. Liu, D.-J.; Walen, H.; Oh, J.; Lim, H.; Evans, J. W.; Kim, Y.; Thiel, P. A. Search for the Structure of a Sulfur-Induced Reconstruction on Cu(111) *J. Phys. Chem. C* **2014**, 118, 29218– 29223, DOI: 10.1021/jp505351g

17. Walen, H.; Liu, D.-J.; Oh, J.; Lim, H.; Evans, J. W.; Aikens, C. M.; Kim, Y.; Thiel, P. A. Cu_2S_3 complex on Cu(111) as a candidate for mass transport enhancement *Phys. Rev. B: Condens. Matter Mater. Phys.* **2015**,91, 045426, DOI: 10.1103/PhysRevB.91.045426

18. Shen, M.; Liu, D.-J.; Jenks, C. J.; Thiel, P. A.; Evans, J. W. Accelerated coarsening of Ag adatom islands on Ag(111) due to trace amounts of S: Mass-transport mediated by Ag-S complexes *J. Chem. Phys.* **2009**, 130,094701, DOI: 10.1063/1.3078033

19. Russell, S. M.; Kim, Y.; Liu, D.-J.; Evans, J. W.; Thiel, P. A. Communication: Structure, formation, and equilibration of ensembles of Ag-S complexes on an Ag surface *J. Chem. Phys.* **2013**, 138, 071101, DOI: 10.1063/1.4790571

20. Walen, H.; Liu, D.-J.; Oh, J.; Yang, H. J.; Kim, Y.; Thiel, P. A. Long-range Displacive Reconstruction of Au(110) Triggered by Low Coverage of Sulfur *J. Phys. Chem. C* **2015**, 119, 21000– 20010, DOI: 10.1021/acs.jpcc.5b06559

21. Biener, M. M.; Biener, J.; Friend, C. M. Sulfur-induced mobilization of Au surface atoms on Au(111) studied by real-time STM *Surf. Sci.* **2007**, 601, 1659– 1667, DOI: 10.1016/j.susc.2007.01.041

22. Maksymovych, P.; Voznyy, O.; Dougherty, D. B.; Sorescu, D. C., Jr.; Yates, J. T. Gold adatom as a key structural component in self-assembled monolayers of organosulfur molecules on Au(111) *Prog. Surf. Sci.***2010**, 85, 206– 240, DOI: 10.1016/j.progsurf.2010.05.001

23. Bailie, J. E.; Hutchings, G. J. Promotion by sulfur of gold catalysts for crotyl alcohol formation from crotonaldehyde hydrogenation *Chem. Commun.* **1999**, 21, 2151– 2152, DOI: 10.1039/a906538e

24. Vericat, C.; Vela, M. E.; Benitez, G.; Carro, P.; Salvarezza, R. C. Self-assembled monolayers of thiols and dithiols on gold: new challenges for a well-known system *Chem. Soc. Rev.* **2010**, 39, 1805– 1834, DOI: 10.1039/b907301a

25. Häkkinen, H. The gold-sulfur interface at the nanoscale *Nat. Chem.* **2012**, 4, 443– 455, DOI: 10.1038/nchem.1352

26. Perdew, J. P.; Burke, K.; Ernzerhof, M. Generalized Gradient Approximation Made Simple *Phys. Rev. Lett.***1996**, 77, 3865– 3868, DOI: 10.1103/PhysRevLett.77.3865, Erratum-ibid. 1997, **78**, 1396.

27. Liu, D.-J. Density functional analysis of key energetics in metal homoepitaxy: quantum size effects in periodic slab calculations *Phys. Rev. B: Condens. Matter Mater. Phys.* **2010**, 81, 035415, DOI: 10.1103/PhysRevB.81.035415

28. de Heer, W. A. The Physics of simple metal clusters: experimental aspects and simple models *Rev. Mod. Phys.* **1993**, 65, 611– 676, DOI: 10.1103/RevModPhys.65.611

29. Brack, M. The physics of simple metal clusters: self-consistent jellium model and semiclassical approaches *Rev. Mod. Phys.* **1993**, 65, 677– 732, DOI: 10.1103/RevModPhys.65.677

30. Schulte, F. K. A Theory of thin metal films: electron density, potentials and work function *Surf. Sci.* **1976**, 55,427– 444, DOI: 10.1016/0039-6028(76)90250-8

31. Miller, T.; Chou, M. Y.; Chiang, T.-C. Phase Relations Associated with One-Dimensional Shell Effects in Thin Metal Films *Phys. Rev. Lett.* **2009**, 102, 236803, DOI: 10.1103/PhysRevLett.102.236803

32. Lopez-Acevedo, O.; Kacprzak, K. A.; Akola, J.; Häkkinen, H. Quantum size effects in ambient CO oxidation catalysed by ligand-protected gold clusters *Nat. Chem.* **2010**, 2, 329– 334, DOI: 10.1038/nchem.589

33. Dronskowski, R.; Blöchl, P. E. Crystal Orbital Hamilton Populations(COHP). Energy-Resolved Visualization of Chemical Bonding in Solids Based on Density-Functional Calculations *J. Phys. Chem.* **1993**, 97, 8617–8624, DOI: 10.1021/j100135a014

34. Reimann, S. M.; Koskinen, M.; Häkkinen, H.; Lindelof, P. E.; Manninen, M. Magic triangular and tetrahedral clusters *Phys. Rev. B: Condens. Matter Mater. Phys.* **1997**, 56, 12147– 12150, DOI: 10.1103/PhysRevB.56.12147

35. Valiev, M.; Bylaska, E.; Govind, N.; Kowalski, K.; Straatsma, T.; van Dam, H.; Wang, D.; Nieplocha, J.; Apra, E.; Windus, T. NWChem: a comprehensive and scalable open-source solution for large scale molecular simulations *Comput. Phys. Commun.* **2010**, 181, 1477– 1489, DOI: 10.1016/j.cpc.2010.04.018

36. Schmidt, M. W.; Baldridge, K. K.; Boatz, J. A.; Elbert, S. T.; Gordon, M. S.; Jensen, J. H.; Koseki, S.;Matsunaga, N.; Nguyen, K. A.; Su, S. *J. Comput. Chem.* **1993**, 14, 1347– 1363, DOI: 10.1002/jcc.540141112

37. Gordon, M. S.; Schmidt, M. W. In *Theory and Applications of Computational Chemistry, the first forty years*; Dykstra, C. E.; Frenking, G.; Kim, K. S.; Scuseria, G. E., Eds.; Elsevier: Amsterdam, **2005**; pp 1167– 1189.

38. Kresse, G.; Hafner, J. Ab initio molecular dynamics for liquid metals *Phys. Rev. B: Condens. Matter Mater. Phys.* **1993**, 47, R558– R561, DOI: 10.1103/PhysRevB.47.558

39. Kresse, G.; Furthmüller, J. Efficiency of ab-initio total energy calculations for metals and semiconductors using a plane-wave basis set *Comput. Mater. Sci.* **1996**, 6, 15– 50, DOI: 10.1016/0927-0256(96)00008-0

40. Blöchl, P. E. Projector augmented-wave method *Phys. Rev. B: Condens. Matter Mater. Phys.* **1994**, 50,17953– 17979, DOI: 10.1103/PhysRevB.50.17953

41. Kresse, G.; Joubert, D. From ultrasoft pseudopotentials to the projector augmented-wave method *Phys. Rev. B: Condens. Matter Mater. Phys.* **1999**, 59, 1758– 1775, DOI: 10.1103/PhysRevB.59.1758

42. Methfessel, M.; Paxton, A. T. High-precision sampling for Brillouin-zone integration in metals *Phys. Rev. B: Condens. Matter Mater. Phys.* **1989**, 40, 3616– 3621, DOI: 10.1103/PhysRevB.40.3616

43. Adamo, C.; Barone, V. Toward reliable density functional methods without adjustable parameters: The PBE0 model *J. Chem. Phys.* **1999**, 110, 6158– 6170, DOI: 10.1063/1.478522

44. Hay, P. J.; Wadt, W. R. *Ab initio* effective core potentials for molecular calculations. Potentials for the transition metals atoms Sc to Hg *J. Chem. Phys.* **1985**, 82, 270– 283, DOI: 10.1063/1.448799

45. Wadt, W. R.; Hay, P. J. *Ab initio* effective core potentials for molecular calculations. Potentials for the main group elements Na to Bi *J. Chem. Phys.* **1985**, 82, 284– 298, DOI: 10.1063/1.448800

46. Hay, P. J.; Wadt, W. R. *Ab initio* effective core potentials for molecular calculations. Potentials for K to Au including the outermost core orbitals *J. Chem. Phys.* **1985**, 82, 299– 310, DOI: 10.1063/1.448975

47. McLean, A. D.; Chandler, G. S. Contracted Gaussian basis sets for molecular calculations. I. Second row atoms, $Z = 11–18$ *J. Chem. Phys.* **1980**, 72, 5639– 5648, DOI: 10.1063/1.438980

48. Krishnan, R.; Binkley, J. S.; Seeger, R.; Pople, J. A. Self-consistent molecular orbital methods. XX. A basis set for correlated wave functions *J. Chem. Phys.* **1980**, 72, 650– 654, DOI: 10.1063/1.438955

49. Clark, T.; Chandrasekhar, J.; Spitznagel, G. W.; von Ragué Schleyer, P. Efficient diffuse function-augmented basis sets for anion calculatons. III. The 3-21+G basis set for first-row elements, Li-F *J. Comput. Chem.***1983**, 4, 294– 301, DOI: 10.1002/jcc.540040303

50. Schuchardt, K.; Didier, B.; Elsethagen, T.; Sun, L.; Gurumoorthi, V.; Chase, J.; Li, J.; Wi ndus, T. L. Basis set exchange: a commnunity database for computational sciences *J. Chem. Inf. Model.* **2007**, 47, 1045– 1052,DOI: 10.1021/ci600510j

51. Bode, B. M.; Gordon, M. S. *J. Mol. Graphics Modell.* **1998**, 16, 133– 138, DOI: 10.1016/S1093-3263(99)00002-9

52. Li, J.; Li, X.; Zhai, H.-J.; Wang, L.-S. Au_{20}: a tetrahedral cluster *Science* **2003**, 299, 864– 867, DOI: 10.1126/science.1079879

53. Kabir, M.; Mookerjee, A.; Bhattacharya, A. K. Structure and stability of copper clusters: A tight-binding molecular dynamics study *Phys. Rev. A: At., Mol., Opt. Phys.* **2004**, 69, 043203, DOI: 10.1103/PhysRevA.69.043203

54. Calaminici, P.; Pérez-Romero, M.; Vásquez-Pérez, J. M.; Köster, A. M. On the ground state structure of neutral Cu_n ($n = 12, 14, 16, 18, 20$) clusters *Comput. Theor. Chem.* **2013**, 1021, 41– 48, DOI: 10.1016/j.comptc.2013.06.014

55. Schouteden, K.; Haesendonck, C. V. Lateral Quantization of Two-dimensional Electron States by Embedded Ag Nanocrystals *Phys. Rev. Lett.* **2012**, 108, 076806, DOI: 10.1103/PhysRevLett.108.076806

CHAPTER 3. COMPARISON OF S-ADSORPTION ON (111) AND (100) FACETS OF CU NANOCLUSTERS

A paper published in the *Journal of Chemical Physics*, 2016, 145(16), 164312

Jeffery S. Boschen, Jiyoung Lee, Theresa L. Windus, James W. Evans, Patricia A. Thiel and
Da-Jiang Liu

JSB and JL were responsible for the atomic orbital basis results, DJL contributed the plane wave basis results.

ABSTRACT

In order to gain insight into the nature of chemical bonding of sulfur atoms on coinage metal surfaces, we compare the adsorption energy and structural parameters for sulfur at four-fold hollow (4fh) sites on (100) facets and at three-fold hollow (3fh) sites on (111) facets of Cu nanoclusters. Consistent results are obtained from localized atomic orbital and plane-wave based density functional theory using the same functionals. PBE and its hybrid counterpart (PBE0 or HSE06) also give similar results. 4fh sites are preferred over 3fh sites with stronger bonding by ~0.6 eV for nanocluster sizes above ~280 atoms. However, for smaller sizes there are strong variations in the binding strength and the extent of the binding site preference. We show that suitable averaging over clusters of different sizes, or smearing the occupancy of orbitals, provide useful strategies to aid assessment of the behavior in extended surface systems. From site-projected density of states analysis using the smearing technique, we show that S

adsorbed on a 4fh site has similar bonding interactions with the substrate as that on a 3fh site, but with much weaker antibonding interactions.

I. INTRODUCTION

The favored site of a surface adsorbate, and the reasons for that site preference, are among the most fundamental types of insight into any surface chemical system. In that vein, early studies of sulfur (S) adsorption on and reconstruction of Cu(111) surfaces indicated a particular stability of structural motifs where a S adatom resides on the four-fold-hollow (4fh) site of a planar square Cu_4 unit. This, in turn, suggested an energetic preference for adsorption of S at more highly coordinated 4fh sites versus lower-coordinated 3fh sites on Cu surfaces.[1]More recent density functional theory (DFT) analysis indicated that reconstructions for the S/Cu(111) system can be stabilized by such motifs.[2] Along this line, a comprehensive integrated experimental and DFT analysis of step edge decoration and reconstruction for S on stepped Cu(111) surfaces consistently indicated a preference for S at 4fh sites. Specifically, (111) micro-faceted steps, which do not present natural 4fh sites, underwent a complex S-induced reconstruction in which Cu atoms shift from their original sites and thereby form a Cu atom base which enables S adsorption at 4fh-type sites.[3]

As an aside, S on other metal(111) surfaces appear to exhibit a similar behavior. S-induced reconstructions on Ni(111) have been observed to incorporate presumed stable Ni_4S units.[4] Ag–S complexes which form on Ag(111) at low temperature, including $Ag_{16}S_{13}$ and larger elongated complexes, consist of overlapping units of $Ag_{16}S_{13}$, also incorporate prominent Ag_4S motifs.[5]

The determination and comparison of the binding energies for S on extended (100) and (111) surfaces of Cu is most naturally performed with plane-wave DFTanalysis utilizing a slab geometry with periodic boundary conditions. Stabilities of both chemisorbed sulfur atoms and Cu–S complexes have been studied using this method.[6–8] A series of calculations with increasing lateral unit cell size with one adsorbate per unit cell enables estimation of the behavior in the limit of zero coverage (or infinite cell size). Unfortunately, such slab calculations often exhibit a surprisingly strong dependence of energetics on the choice of slab thickness, i.e., they can suffer somewhat slow convergence to a limiting behavior for infinite thickness (corresponding to the semi-infinite surface system of interest). It has been proposed that appropriate averaging of results over slab thicknesses can eliminate such quantum size effects (and also *k*-points and/or basis sets convergence issues).[8,9] We return to this theme below.

In this contribution, to provide a more extensive analysis of the adsorption site dependence of S bonding than the above type of slab calculations, we consider the behavior for sequences of square pyramidal nanoclusters with exposed base (100) facets, as well as tetrahedral nanoclusters with exposed (111) facets. As an aside, such analysis is potentially also relevant for characterization of chemisorption on supported metal nanoclusters. For sufficiently large clusters above ~280 atoms, we find a consistently strong preference for binding at 4fh sites on (100) facets versus 3fh sites on (111) facets by ~0.6 eV. However, highly accurate DFT calculations show variations in binding of around 0.4 eV for clusters as large as 200 Cu atoms. Furthermore, there is no sign of the often-anticipated[10] simple exponential decay in the size dependence of the adsorption energy, even for systems with linear size as large as 3 nm. As a consequence, this brings into question a picture of the S–Cu chemical bond as being local in nature.

The above observations highlight two related challenges in understanding these adsorption systems. As emphasized above, adsorption energetics for clusters of finite size (or for slabs of finite thickness) can exhibit strong deviations from the behavior on extended surfaces. This derives in part from the lack of localization in chemical bonding which in turn complicates the characterization of such bonding, including the understanding of the difference in bonding between 3fh and 4fh adsorption sites. Actually, it has been long recognized, but perhaps under-appreciated, that locality arises from cancellation of different phases of the Bloch states in extended systems.[11–13] This type of cancellation should not be expected to occur for calculations performed on a single cluster with simple geometric shape, even with hundreds of atoms, as coherent interference can occur between electron waves scattering from the different cluster surfaces. Elimination of the strong size dependence and associated enhancement of localization should occur by introducing some type of randomization into the system, e.g., by incorporating random defects, or by introducing rough surfaces. Below, we describe two strategies to mimic such randomization which we propose will reduce the size-dependence of energetics, thus making binding strength and site preference better match those for the extended semi-infinite surface.

Suitably averaging over the energetics of clusters of different sizes is one way to introduce the cancellation effect described above. We find that by averaging results for a range of cluster sizes, N_{Cu} measured in atoms (roughly speaking in the range from $N_{\mathrm{Cu}} = 100$ to 400), one can achieve essentially the same adsorption energies using finite clusters as those from slab geometry calculations.

A more efficient method to assess the behavior in extended surfaces is to utilize partial (fractional) occupancies, which are implemented in many DFT codes, to smear out the effect of the Fermi (HOMO) energy. In Sec. IV, we explore the effects of broadening the occupancy function and show that much faster convergence to energetics for the semi-infinite surface system can be achieved by judiciously choosing the broadening parameter. Furthermore, comparing the density of states (DOS's) projected onto the adsorbate using the broadened occupancy, the role of antibonding orbitals is clarified, thus facilitating understanding of the difference in adsorption energy between the 3fh and 4fh sites.

Section II briefly summarizes the computational methods used in this paper. The main results comparing S binding on (111) and (100) facets of clusters of various sizes and averaging over large cluster sizes are presented in Sec. III. Results obtained by broadening the occupancy function, and the associated understanding of the difference in bonding at 3fh and 4fh sites, are presented in Sec. IV. Further discussion and conclusions are provided in Sec. V.

II. COMPUTATIONAL DETAILS

DFT calculations are performed using both plane-wave (VASP[14,15] version 5.4.1) and Gaussian (NWChem[16]) basis sets. More technical details can be found in a previous paper.[17] All calculations are without spin polarization, except for the S_2dimer in vacuum. PBE[18] functionals are used in VASP and NWChem calculations. The hybrid PBE0 functional[19] is also used in NWChem calculations, and its screened version (HSE06[20]) is used in VASP calculations. For VASP calculations, the PAW potentials for Cu and S that are optimized for the PBE functional are used.[21] The cutoff energy for the plane-wave basis set is 280 eV. For NWChem, basis sets are Los Alamos National Laboratory double zeta with effective core potential (LANL2DZ ECP) for Cu[22] and 6-311++G(d,p) for S.[23–25] Some results are also checked with the larger basis sets def2-QZVP and def2-QZVPPD.[26,27]

Calculations of S adsorption are performed using VASP for both slab and cluster geometries. For slab calculations, surfaces are simulated by periodic slabs of various thicknesses separated by 1.2 nm of vacuum. Supercells are chosen so that two of the basis vectors are that of superlattices of Cu(100) or Cu(111) surface, and the third is perpendicular to the slab surface. For clusters, orthorhombic supercells are used so that each supercell contains one Cu cluster, separated by 1.2 nm of vacuum in all three directions. NWChem calculations are performed for clusters only, but with open boundaries.

III. ANALYSIS OF S ADSORPTION ON ISOLATED CLUSTERS

All clusters considered in this paper are formed by truncation of bulk fcc Cu. One can regard them as being constructed by starting from a single atom and then adding various numbers of layers with suitable structure and increasing areas. The S atom will be adsorbed near the center of the last largest layer added. Two classes of clusters are thereby constructed. To mimic adsorption on a (111) surface, we add hexagonally close-packed equilateral triangular layers with side lengths 2, 3, up to l (in atoms). This generates a series of clusters of tetrahedral (T_d) symmetry. The number of Cu atoms N_{Cu} in a cluster can be written as $N_{\mathrm{Cu}} = l(l + 1)(l + 2)/6$. For $l = 3m + k$, where $m \geq 0$ and $0 \leq k \leq 2$ are integers, the center of the facet is a fcc site, hcp site, or top site, if $k = 0, 1,$ or 2, respectively. For the 3fh site, we choose the center fcc and hcp sites when $k = 0$ and 1, and the fcc site closest to the center when $k = 2$.

To mimic adsorption on the (100) surface, we instead add square layers with side lengths 2, 3, up to l (in atoms). The clusters thus generated can be viewed as octahedral clusters cut in half, thereby denoted as O_h^2 clusters and $N_{\mathrm{Cu}} = l(l + 1)(2l + 1)/6$. Only for $l = 2m$, the center of the top layer is a 4fh site, so for $l = 2m + 1$ we choose the 4fh site closest to the center. Examples of clusters of both 3fh and 4fh sites are shown as insets in Fig. 1.

A. Comparison of different methods and functionals

Table I shows results of the adsorption energy, E_b determined with different methods and exchange-correlation functionals. The adsorption energy E_b is calculated by:

$$E_b(\mathrm{S}) = E(\mathrm{S} + \mathrm{Cu}_n) - E(\mathrm{Cu}_n) - E(\mathrm{S}_2)/2$$

where $E(\mathrm{S} + \mathrm{Cu}_n)$ is the total energy of the Cu cluster with a single S atom adsorbed, $E(\mathrm{Cu}_n)$ is the total energy of the Cu cluster itself, and $E(\mathrm{S}_2)$ is the energy of a S_2 molecule in vacuum. For VASP calculations, the Gaussian smearing of width 0.02 eV is used. There is no smearing in NWChem calculations. Using the same PBE exchange-correlation functional, the difference between E_b obtained from plane-wave and Gaussian basis sets is generally within 0.10 eV, i.e., there is excellent agreement between the two approaches. This validation process is important, since medium to large size metal clusters are not the natural environment for either plane-wave or atomic basis set DFT codes. The agreement between the two different methods gives confidence that results presented below do not reflect numerical artifacts.

Results using the PBE0 and HSE06 functionals also generally agree well with the PBE results, the difference usually being within 0.1 eV. However, there are certain clusters (e.g., 30-atom O_h^2, 20-atom T_d) where the difference is significantly larger. Also the consistency of results for PBE0 obtained with different Gaussian basis sets is not as good as for PBE. The largest differences in the Gaussian basis sets show up in the 5-atom O_h^2 cluster and the 20-atom $T_d$cluster.

TABLE 1**.** Adsorption energy E_b(eV) of S on clusters of different shapes and sizes. PAW potentials and plane-wave basis set with energy cutoff of 280 eV are used for VASP. For NWChem, the superscripts a and b denote combinations of LANL2DZ/6-311++G(d,p) and def2-QZVP/def2-QZVPPD for Cu/S, respectively. Geometries of all clusters are from the VASP/PBE optimized structure.

	PBE			HSE06	PBE0	
N_{Cu}	VASP	NW^a	NW^b	VASP	NW^a	NW^b
S on 4fh sites, O_h^2 clusters						
5	-1.717	-1.827	-1.872	-1.885	-2.048	-2.356
14	-2.001	-1.921	-2.054	-1.989	-2.018	-2.094
30	-2.001	-1.934	-2.146	-1.969	-2.311	-2.239
55	-2.322	-2.361		-2.357	-2.480	
91	-2.626	-2.554			-2.487	
S on 3fh sites, T_d clusters						
4	-3.537	-3.825	-3.909	-3.931	-4.026	-4.081
10	-2.231	-2.349	-2.328	-2.403	-2.587	-2.555
20	-0.611	-0.564	-0.662	-0.350	-0.155	-0.425
35	-2.327	-2.442		-2.347	-2.417	
56	-2.160	-2.335		-2.261	-2.330	
84	-1.489	-1.551		-1.493	-1.647	

B. Comparison of 3fh vs 4fh adsorption energy vs cluster size

Figure 1 shows the adsorption energy E_b of S on 3fh sites on T_d clusters and 4fh sites on O_h^2 clusters of various sizes from VASP calculations. Two sets of data are calculated for each geometry. The first set, represented by solid lines in Figure 1, has the Cu atoms in the cluster fixed at their bulk positions, allowing only the S atom to relax. The second set, represented by dotted lines, allows all atoms to relax. Results are obtained using the plane-wave basis set.

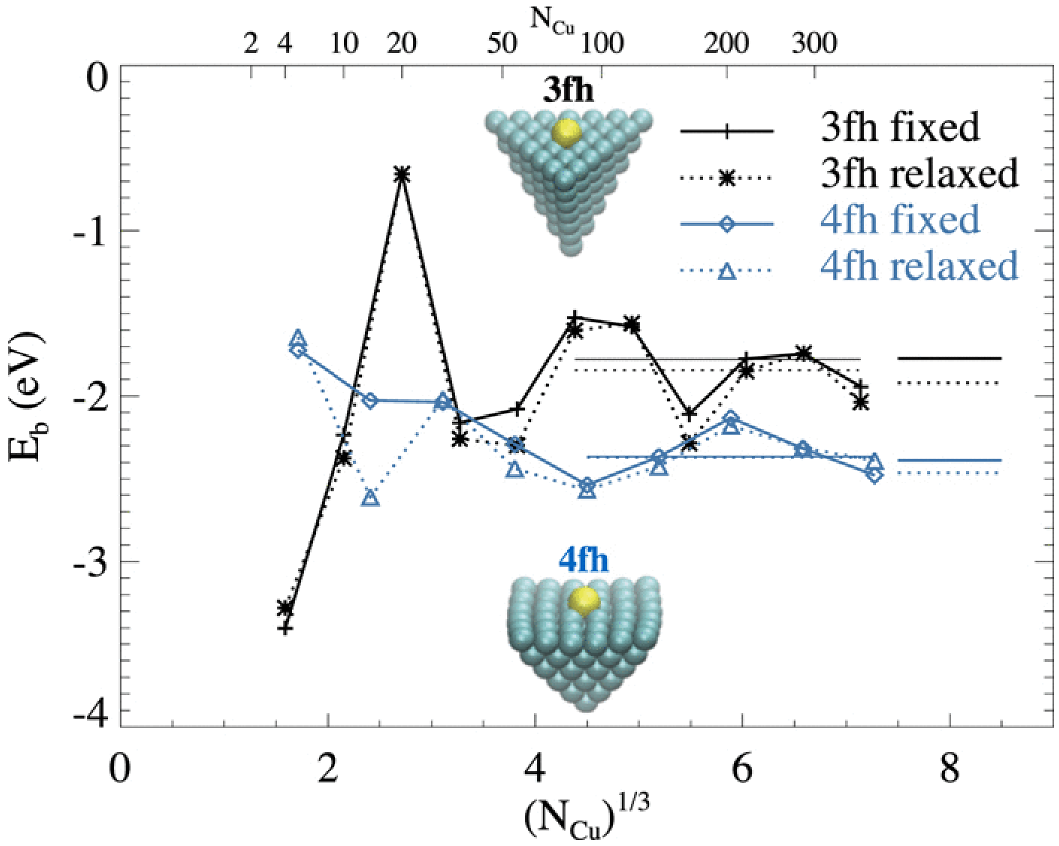

FIG. 1. Adsorption energy of S on 3fh and 4fh sites, with fixed and fully relaxed substrates. The insets show S adsorbed on a 3fh site of an 84-atoms T_d cluster, and a 4fh site of a 91-atom O_h^2 cluster, with full geometric relaxation. Note the more significant relaxation of the O_h^2 cluster. The longer horizontal lines show the values of E_b averaging over results for the larger clusters. The shorter horizontal lines represent results obtained from slab calculations. See text for more details. Data for 3fh sites are taken from Ref. 17.

The somewhat surprising result in Figure 1 is that not only is there a very large size dependence in E_b, but also the preference for 4fh over 3fh only emerges for very large clusters. For $N_{\mathrm{Cu}} < 100$, E_b is very sensitive to the cluster size, and the variation with N_{Cu} dominates over any site preference. Even for $N_{\mathrm{Cu}} > 100$, E_b can be very close for the two types of adsorption sites for clusters of similar sizes, although the preference towards 4fh sites does emerge as a trend.

Results with the fully relaxed clusters are mostly in line with the counterparts for a fixed substrate. For some of the smaller O_h^2 clusters, however, larger deviations are observed. This can be explained by the observation that the exposed (100) surface is much less thermodynamically stable and will sometimes reconstruct from the pristine (100) structure. Also for O_h^2 clusters, sometimes the clean and S-adsorbed clusters can relax into different shapes. For these occasions, we choose the more stable S-adsorbed configuration as the starting point and redo the calculation for the metal cluster with an S atom removed. In most cases, relaxation lowers the value of E_b slightly, although some exceptions can be found for S on 4fh sites of O_h^2 clusters.

As indicated in Sec. I, by suitably averaging binding energies over a range of (larger) cluster sizes, one might be able to efficiently assess the adsorption behavior on extended surfaces. In general, binding energy displays quasi-periodic variation as a function of *linear* cluster size, which arises from the interference of the cluster boundaries and the electronic wave functions. Thus, it is natural and appropriate to average over a number of periods in order to extract a limiting large-size behavior. We note that the period depends on the cluster geometry and indeed is different for our analysis of binding at 3fh versus 4fh sites. For 3fh sites, averaging over N_{Cu} from 84 to 364 which corresponds to roughly two periods of oscillation yields $E_b = -1.78 \pm 0.04$ eV for unrelaxed substrates and -1.84 ± 0.05 eV for relaxed substrates. The errors are estimated using the standard deviations of the data divided by the number of samples, thus reflecting the general expectation that by averaging a larger range of cluster sizes, one can better approach the limiting behavior. For 4fh sites, averaging over N_{Cu} from 91 to 385 which corresponds to roughly one period of oscillation yields $E_b = -2.36 \pm 0.03$ eV for unrelaxed substrates and -2.37 ± 0.03 eV for relaxed substrates. These results are shown in Fig. 1 as horizontal solid lines running through data points that are used for the averaging.

We also calculate independently the S adsorption energy using a periodic slab geometry. For the (100) surface, large oscillations in E_b as a function of the slab thickness are found. These are due to the 2D quantum confinement effect. Appendix B illustrates these effects through an analysis with (2 × 2) supercells (1/4 ML S coverage). To obtain bulk adsorption energies, we average over DFT results for slab thicknesses from 7 to 12 layers and obtain $E_b = -2.400 \pm 0.002$ eV with $\theta_S = 1/16$ ML for an unrelaxed substrate and $E_b = -2.468 \pm 0.006$ eV with $\theta_S = 1/20$ ML for a relaxed substrate. For the (111) surface, less thickness dependence is found, and we calculate the bulk adsorption energy by averaging slab thicknesses from 4 to 7 layers to obtain $E_b = -1.778 \pm 0.003$ eV with $\theta_S = 1/12$ ML for an unrelaxed substrate and $E_b = -1.926 \pm 0.004$ eV with $\theta_S = 1/16$ ML for a relaxed substrate. At the right side of Figure 1, we show the calculated E_b for fcc sites on Cu(111) and 4fh sites on Cu(100) with the periodic slab geometry. Consistent with the trend established for large Cu clusters, S adsorption on the 4fh site is stronger than the 3fh site in the slab geometry calculations. Note that with averaging, the cluster results are completely consistent with the slab results for unrelaxed substrates, while some deviations exist for relaxed substrates.

Note that here we focus on 3fh and 4fh sites. For S on extended Cu surfaces, other adsorption sites are significantly less favorable. DFT-PBE calculations show that the adsorption of a sulfur atom on a bridge site is 0.95 eV weaker than the 4fh site on the

Cu(100) surface. Adsorption on a top site is even less favorable, being 1.54 eV weaker than the fcc site on the Cu(111) surface. Thus bridge sites and top sites have negligible population.

We conclude this subsection with some remarks about the averaging procedure. In the free electron picture, the quasi-periodic behavior of E_b arises from interference of the wave functions reflected by cluster or slab boundaries. If one can make the linear size l of the system a continuous variable, e.g., using a jellium model, then E_b and other physical quantities can be described as piece-wise continuous curves, with periodicity $\lambda_F/2$ for $l \rightarrow \infty$,[28] where λ_F is the Fermi wavelength. For the averaging procedure to be effective, the phases of the data points on this oscillatory curve should be incoherent, or in other words, more or less evenly distributed among the hills and valleys of the curve. If this condition is satisfied, then the average will not be very sensitive to the range of sizes used and also approach the limiting value rather quickly. We find that this is generally true for the systems studied here. However, there are systems, e.g., (110) surfaces of coinage metals, where the phase incoherence requirement is not met.[29] In this case, the averaging procedure is not very effective in eliminating the quantum size effect, even averaging over slabs of up to 12 layers.[30]

C. Comparison of bond length for 3fh vs 4fh adsorption sites

Figure 2 shows the bond length between S and its nearest-neighbor Cu atoms from VASP for the same sets of configurations as those in Fig. 1. Unlike the adsorption energy, the respective S–Cu bond lengths for S at the 3fh and 4fh sites converge rather quickly, basically reaching their bulk limits for $N_{\mathrm{Cu}} > 100$. Furthermore, the bond length for S on 3fh sites is about 3% shorter than on 4fh sites. The convergence to the bulk value, as plotted at the right side of the figure, is also quite apparent. The asymptotic value of 0.229 nm for Cu–S bond length at the 4fh site is slightly larger than the 0.226 nm value obtained from an experimental photoemission study.[31] This is consistent with the general level of accuracy of DFT/PBE.

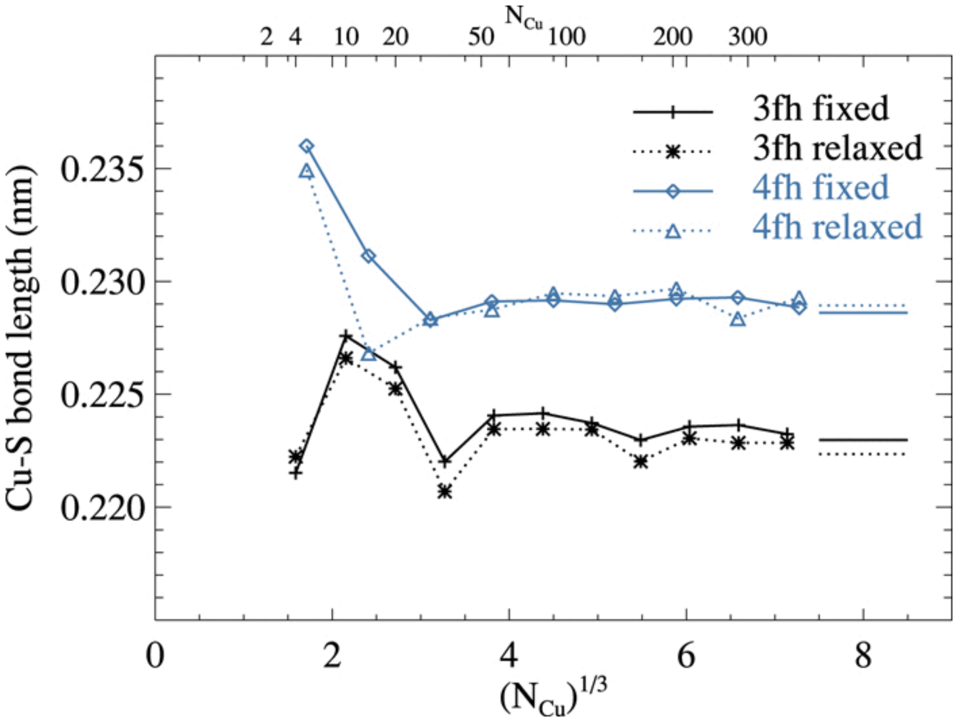

FIG. 2. Average bond length of S on 3fh and 4fh sites, with fixed and fully relaxed substrates.

It is interesting to note that the bond length predicted by optimization of the S with a fixed substrate using the Gaussian basis sets of LANL2DZ (Cu) and 6-311++G(d,p) (S) is about 3.5% longer than the VASP prediction. This is likely due to the shortcomings of the 6-311++G(d,p) basis set for treating S. Using def2-QZVPPD for S instead predicts bond-lengths which are only 0.5% longer than the VASP values. However, a combination of LANL2DZ and def2-QZVPPD results in an unbalanced description of the system, with a much larger basis set on S than on Cu, which causes overbinding. A combination of def2-QZVP (Cu) and def2-QZVPPD (S) gives good agreement with VASP results for both adsorption energy and bond lengths (see Table I).

IV. EFFECTS OF BROADENING THE OCCUPANCY FUNCTION

As shown in Sec. III, for an isolated cluster, quantum confinement of electrons introduces a correction to the large-size limit of the adsorption energy that does not decay exponentially with the system size. We also find that removing one or more atoms from the corners of a cluster can change the adsorption energy by as much as 0.4 eV for a cluster of about 100 atoms.[17] As mentioned in Sec. I, these features reflect a lack of locality of chemical bonding in metallic solids. In our case, the clusters consist of a few flat surfaces (together with some edges and corners), which can create coherent interference in the wave functions. Again, localization and thus minimization of size effects come from cancellation of the phase of Bloch waves which can be produced by introducing randomness into the system. Our proposal here is that by introducing such effects to reduce size dependence, we can more efficiently assess the energetics of the semi-infinite extended surface system. Further validation of this idea is provided below.

Specifically, in this section, we explore the technique of partial (or fractional) occupancy that has been implemented in many DFT codes as a way to introduce the above-mentioned phase cancellation. In real solid systems, the probability of occupancy of energy levels for electrons approaches that of a step function, but it is often more efficient numerically in solid state electronic calculations to broaden the step function (or, more exactly, the Fermi-Dirac distribution).[32] The key physics is that the position of the Fermi level, relative to the electronic band structure, is sensitive to the system size.[28] By adding noise to the exact position of the Fermi level, one can simulate randomness in a system. The smearing method, by broadening the occupancy function, adds uncertainty to the Fermi level and is thus a natural way to simulate “noisy” Fermi levels.

A. Adsorption energy versus cluster size

Figure 3 shows E_b calculated for unrelaxed metal substrates with Gaussian smearing but deliberately choosing a larger smearing width σ than the default value 0.2 eV used in Fig. 1. The size dependence is greatly reduced, and the convergence to the limiting large-size value of $E_b = -1.78$ (-2.39) eV for 3fh (4fh) sites is more apparent. The larger the σ values, the smaller the extent of size dependence. The dramatic reduction in size dependence is consistent with the above stated proposal that enhanced smearing mimics the introduction of randomization to the system which in turn enhances localization. Ideally, the more readily assessed limiting large-size behavior evident from this analysis provides an efficient assessment of binding on a semi-infinite extended surface.

One caveat is that with large σ, the detailed form of the smearing becomes relevant. Using the Methfessel-Paxton (MP) scheme,[32] for which the occupancy function approaches a step function faster than for Gaussian smearing as σ decreases, leads to somewhat different results for large σ. For example, using the first-order MP with $\sigma = 1.0$ eV, E_b on 4fh sites in O_h^2 clusters converges to -2.25 eV versus the -2.37 to -2.40 values obtained using the other three methods (averaging different cluster sizes, slab geometries, and Gaussian smearing with $\sigma = 1.0$ eV). For 3fh sites, the MP smearing with $\sigma = 1.0$ eV yields $E_b = -1.63$ eV, versus the -1.78 eV value obtained using the other methods. We conclude that Gaussian smearing is more appropriate for our purposes here.

Strictly speaking, even with Gaussian smearing, different σ values will lead to a different limiting behavior, and the physically relevant value should correspond to the limit of $\sigma \rightarrow 0$. With slab geometries and a relatively small (2 × 2) supercell, we find that between $\sigma = 0.2$ and 1.0 eV, the values of E_b for S/Cu(100) do deviate, but the differences are relatively small (about

0.025 eV). For S/Cu(111), on the other hand, the change due to σ is within numerical uncertainties. The optimal choice of the form and width of the smearing function is an open question at this stage.

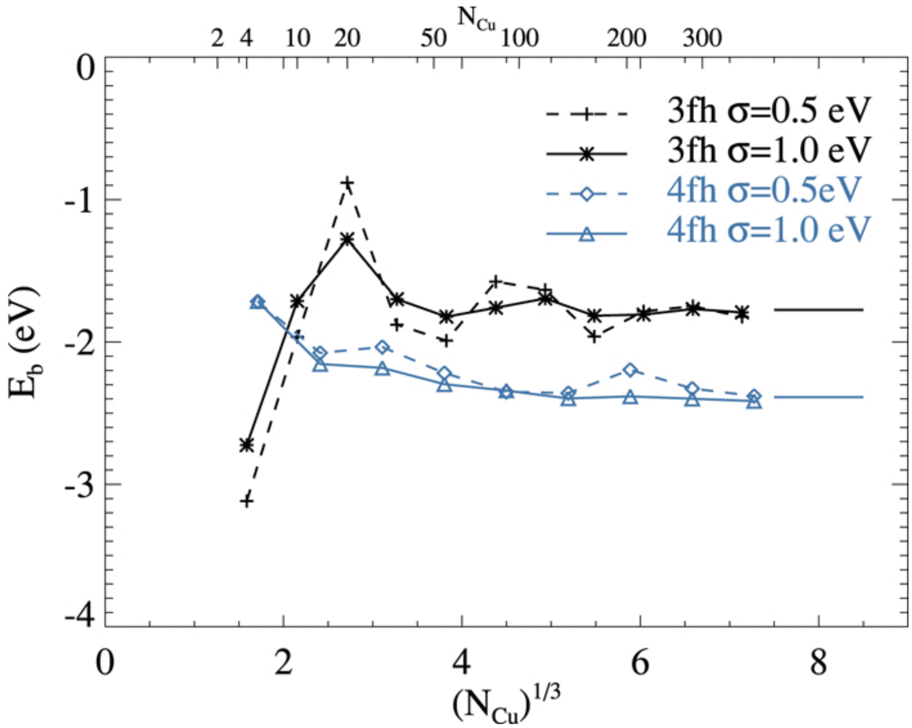

FIG. 3. The adsorption energy E_b as a function of the cluster size, with Gaussian smearing of the occupancy function with widths 0.5 eV and 1.0 eV. The two short horizontal lines represent the corresponding slab geometry calculation results, with frozen substrates.

B. Site-projected density of states analysis

Perhaps more important than potentially providing a more efficient method to estimate E_b for S on extended Cu surfaces from cluster calculations, we can also use the smearing of the occupancy function to elucidate the difference between the bonding of S in 3fh and 4fh sites. One way to visualize interactions between S and a cluster is through plotting the site-projected density of states (SDOS's) of individual atoms. Figure 4 shows the SDOS localized on the S on the center 4fh site of a 91-atom O_h^2 cluster, obtained using Gaussian smearing of different widths σ. With a small σ, the SDOS consists of many sharp spikes, each of which corresponds to one or more molecular orbitals. (As an aside, analogous sharp spikes appear in the SDOS for slab calculations.) The highly complex SDOS, especially near the Fermi level, is directly responsible for the large size dependence of binding seen in Sec. III A. It also makes it more difficult to obtain an intuitive picture of chemical bonding. By widening the smearing, a smoother SDOS can be achieved, which facilitates interpretation of bonding. It is significant to note that Feibelman[6] also used Gaussian-smearing of the DOS to obtain insights into Cu–S clusters on Cu(111) surfaces. In his case, the DOS was projected onto Cu atoms and his analysis used slab (rather than cluster) geometries.

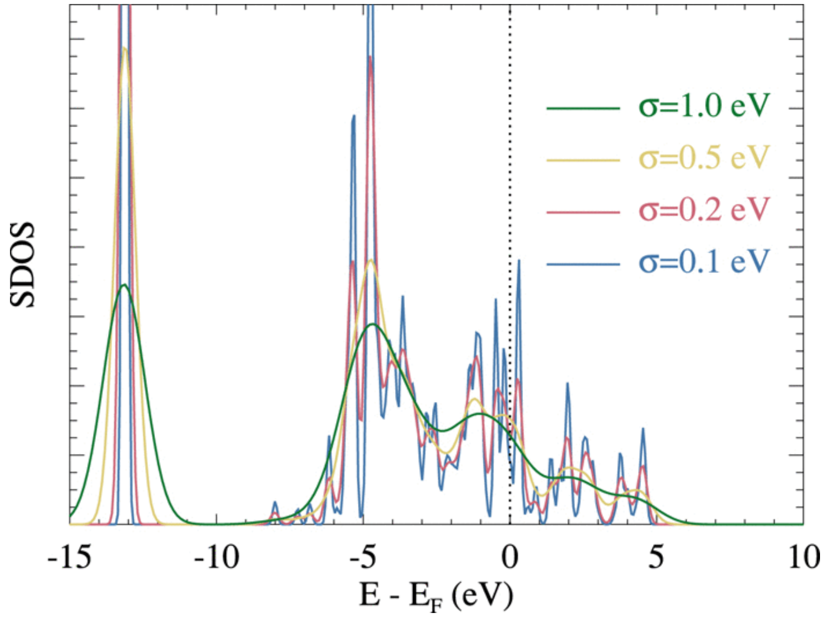

FIG. 4. Effects of smearing widths on SDOS for an S atom on a 4fh site in a O_h^2 cluster with 91 Cu atoms. Here the energies are shown relative to the Fermi energy, in contrast to Fig. 5.

The solid line in Fig. 5 shows the SDOS of a S atom on the 3fh site of a T_d cluster with 56 Cu atoms, with Gaussian smearing of 1.0 eV. Analysis of the electronic structures using the crystal orbital Hamilton population (COHP) method[33] shows that the peaks near −17 and −8 eV are mostly bonding, and the peak near −5 eV is mostly antibonding. (Note that in Fig. 5 the energy is relative to the reference configurations of individual atoms, rather than the Fermi energy as is the usual practice in solid state physics as in Fig. 4. This is done in order to make the comparison between S on different adsorption sites more transparent.) The dashed line is for an S atom on a 4fh site of the (100) face of a O_h^2 cluster with 91 Cu atoms. Compared with S on the 3fh site, the main difference in the SDOS is that the antibonding states are more spread out. This results in a higher Fermi energy, E_F, which in turn forces the bonding state deeper below the Fermi level, thus increasing the strength of binding. Thus the difference between S adsorption on the 4fh site and the 3fh site can be understood intuitively in the following way: on a 4fh site, with more neighboring Cu atoms, the S does not have to be as close to the Cu atoms as on the 3fh to maximize the bonding coupling between the S and Cu orbitals. This in turn leads to much smaller antibonding coupling between the S and Cu atoms, which is due to the faster decay of the antibonding interactions as the separation increases. Note that the linear sizes l for the two types of clusters shown in Fig. 5 are the same, and there can be less perfect matches when choosing different clusters. Nevertheless, the qualitative picture remains the same.

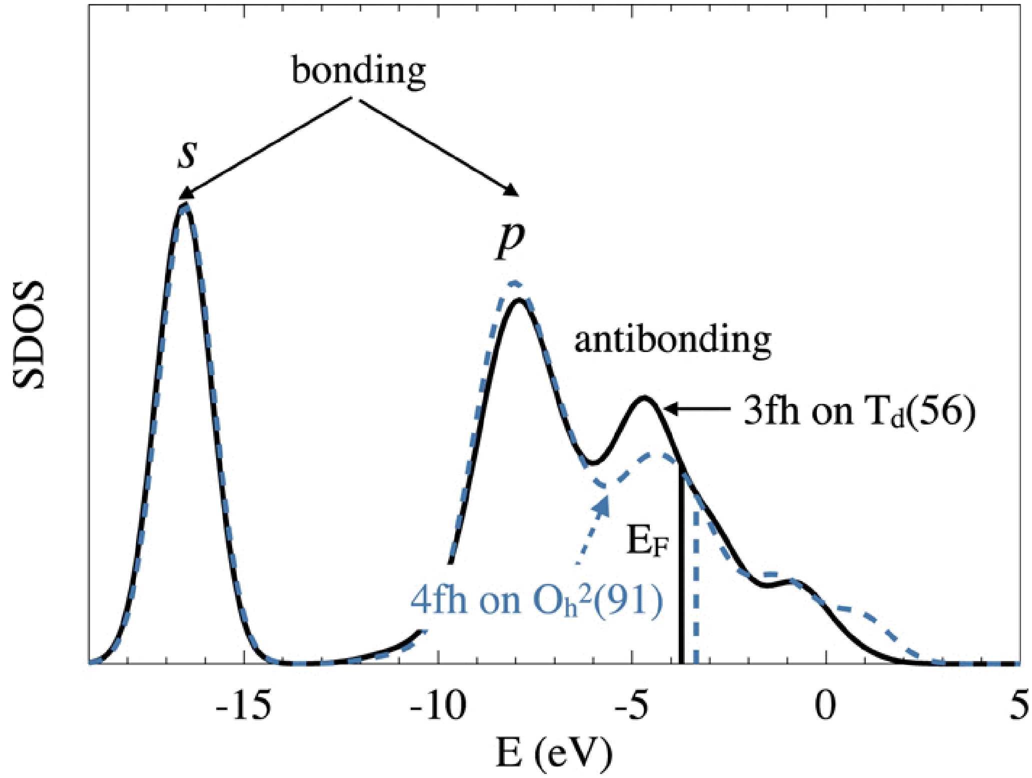

FIG. 5. Site-projected density of states (SDOS) of a S atom on a 3fh site of a T_d cluster with 56 Cu atoms (solid line), and a S atom on a 4fh site of a O_h^2 cluster with 91 atoms (dashed line). Gaussian smearing of width 1.0 eV is used. Energy is relative to individual atoms, rather than the Fermi energies, which are plotted as two distinct vertical lines. There are two broad peaks for bonding orbitals, from the sulfur *s* and *p* electrons respectively.

V. DISCUSSION AND CONCLUSION

Good agreement has been achieved between DFT codes employing plane-wave and Gaussian basis sets, regarding the adsorption of S on Cu clusters of various sizes. However, we find that the large size-dependence in the adsorption energies makes it challenging to estimate the limiting value of binding on an extended surface, and the associated delocalization makes it challenging to elucidate the nature of chemical bonds between the S adsorbate and the metal cluster. It has been long recognized that for small clusters (less than 50 atoms), the discreteness of the orbitals, especially the HOMO-LUMO gap, will lead to a behavior quite different from their bulk counterpart. Another issue, which is familiar in condensed matter physics, is that for an isolated cluster, interference of wave functions from the boundaries will lead to corrections that do not decay exponentially. For Cu clusters, the adsorption energy can be significantly affected (up to 0.6 eV) by what happens 1.5 nm away from the adsorption site.

A natural question is then, how can calculations on small to medium size clusters be relevant to adsorption on extended single-crystal surfaces? A simple but effective method is to average over results for clusters over a suitable range of sizes (as described in Sec. III). One could anticipate similar results from suitably averaging over different shapes, or by performing analysis for clusters with rough side surfaces. Another strategy which is particularly efficient for plane-wave methods is to utilize the partial occupancy technique which was originally developed for numerical efficiency. By choosing an appropriate smearing function (e.g., Gaussian), we can reliably assess binding on extended surfaces from calculations on medium size clusters.

By averaging contributions from different orbitals, we can understand the adsorption of S on metal clusters in a way that is both intuitive and also rests on firm quantitative grounds. We suggest that the stronger binding of S to 4fh sites is due to the weaker antibonding interactions compared with 3fh, while having similar bonding interactions. This interpretation of chemical bonds as a competition between bonding and antibonding interactions through interference energies, as advocated a long time ago by Ruedenberg,[34] is key to understanding the site preference of simple adsorbates.

ACKNOWLEDGMENTS

J.S.B., J.L., T.L.W., J.W.E., and D.J.L. performed the computations in this work and were supported for this work by the U.S. Department of Energy (USDOE), Office of Basic Energy Sciences, Division of Chemical Sciences, Geosciences, and Biosciences through the Ames Laboratory Chemical Physics program. Use of NERSC computational resources is acknowledged. PAT provided experimental insights into key issues for S adsorption systems and was supported for this work by NSF Grant No. CHE-1507223. The work was performed at Ames Laboratory which is operated for the USDOE by Iowa State University under Contract No. DE-AC02-07CH11358.

APPENDIX A: MODIFIED ADSORPTION AT AND NEAR STEPS

On fcc(111) surfaces, the so-called A-step creates microfacets resembling the (100) surface locally. Thus adsorption of S along an A-step may be akin to adsorption on a 4fh site. In order to study this via the cluster approach, we create steps on top of a cluster by adding an incomplete layer, or an island, on one face of the cluster. In Fig. 6, we consider two types of A-steps, one formed by an island that has its boundary as close as possible to the edge of the cluster, thus exposing a step edge with length $l - 2$ on a cluster with side length l. Note that the larger island with side length $l - 1$ consists of Cu atoms on hcp sites, rather than fcc sites. DFT-PBE results for S adsorption along this kind of step edge are shown in Fig. 6 as the black pluses. The average result for clusters with $l = 8$–12 is −2.52 eV, which is slightly lower than the equivalent value of −2.36 eV for the 4fh site on the (100) surface (Sec. III and Fig. 1). The other type of step has one row of Cu atoms removed from the island in the first type, thus one of the step edges is further removed from the edge of the cluster. See insets of Fig. 6 for illustrations.

Results for S adsorption on these types of steps are shown in Fig. 6 as red asterisks. The average value for $l = 8–12$ is −2.09 eV, which lies between −1.77 eV (3fh) and −2.36 eV (4fh) obtained in Sec. III. Therefore, the expectation that A-steps on Cu(111) are more favorable adsorption sites than flat terraces are met, although some differences are found depending on configurations further away from the step edges.

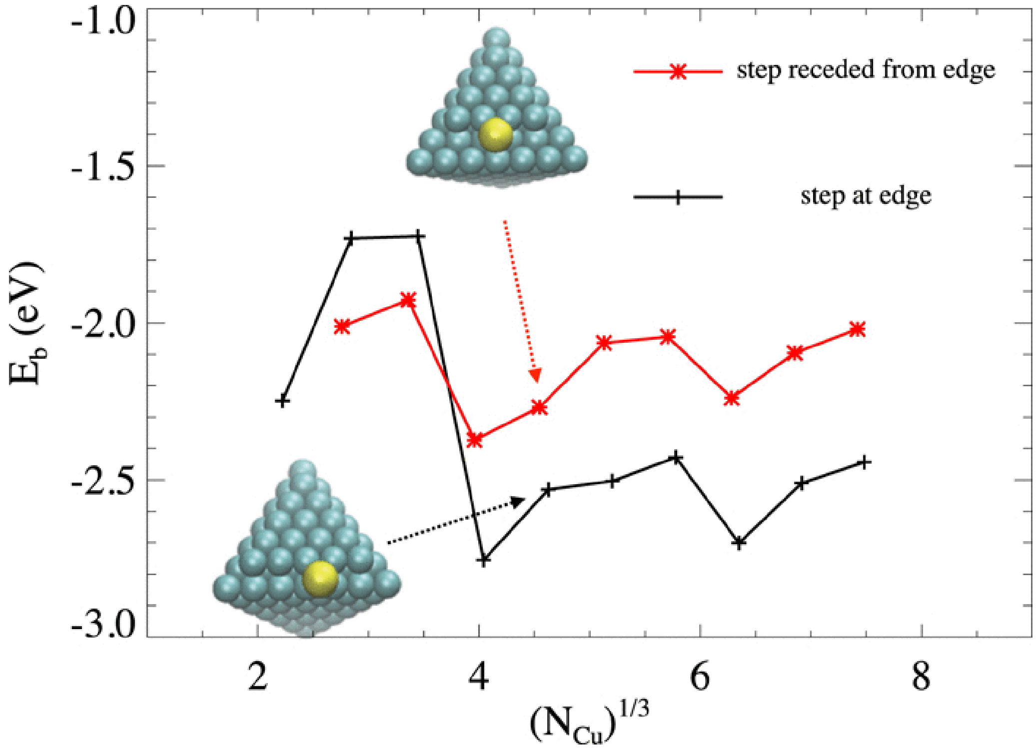

FIG. 6. Adsorption energy E_b for S at step edges. The pluses (connected by a black line) are for steps right on the edge, and the asterisks (connected by a red line) are for steps receded from the edge by one row of atoms.

APPENDIX B: DEPENDENCE OF THE ADSORPTION ENERGY ON THE SLAB THICKNESS

Here, we quantify how the S adsorption energy depends on the thickness of the slab in calculations with semi-infinite slab geometries. Table II lists the adsorption energy E_b for S on Cu(100) and Cu(111) surfaces, calculated using slabs of different thicknesses measured by the number of layers L. All atoms are allowed to relax except for the bottom layer of Cu atoms. Also listed are the average value $\langle E_b \rangle$ and the standard deviation δE_b for each L calculated using data up to L. For example, for $L = 12$, we use data from 7 to 12. While the extent of variations using slabs is much smaller than results using clusters, the convergence to the bulk limit is also slow. Also note that variations of a few meV can be due to numerical errors.

TABLE II. Adsorption energy E_b, average value $\langle E_b \rangle$, and standard deviation δE_b (in eV) for S on Cu(100) and Cu(111) with different slab thicknesses L, all with (2 × 2) supercells and (24 × 24 × 1) k-point grid.

L		1	2	3	4	5	6	7	8	9	10	11	12
	E_b	−2.733	−2.457	−2.340	−2.450	−2.404	−2.398	−2.424	−2.406	−2.436	−2.426	−2.420	−2.429
Cu(100)	$\langle E_b \rangle$				−2.395	−2.398	−2.417	−2.419	−2.408	−2.414	−2.418	−2.418	−2.423
	δE_b				0.078	0.055	0.028	0.023	0.011	0.016	0.015	0.014	0.010
	E_b	−1.252	−1.953	−1.842	−1.871	−1.854	−1.875	−1.861	−1.859	−1.859	−1.859	−1.849	−1.860
Cu(111)	$\langle E_b \rangle$				−1.857	−1.856	−1.867	−1.866	−1.863	−1.862	−1.863	−1.861	−1.858
	δE_b				0.021	0.015	0.011	0.009	0.009	0.008	0.007	0.008	0.004

REFERENCES

1. M. Foss, R. Feidenhans’l, M. Nielsen, E. Findeisen, T. Buslaps, R. L. Johnson, and F. Besenbacher, Surf. Sci. **388**, 5 (1997). https://doi.org/10.1016/S0039-6028(97)00071-X

2. D.-J. Liu, H. Walen, J. Oh, H. Lim, J. W. Evans, Y. Kim, and P. A. Thiel, J. Phys. Chem. C **118**, 29218 (2014). https://doi.org/10.1021/jp505351g

3. H. Walen, D.-J. Liu, J. Oh, H. Lim, J. W. Evans, Y. Kim, and P. A. Thiel, J. Chem. Phys. **142**, 194711 (2015). https://doi.org/10.1063/1.4921258

4. M. Foss, R. Feidenhans’l, M. Nielsen, E. Findeisen, R. L. Johnson, T. Buslaps, I. Stensgaard, and F. Besenbacher, Phys. Rev. B **50**, 8950 (1994). https://doi.org/10.1103/PhysRevB.50.8950

5. S. M. Russell, Y. Kim, D.-J. Liu, J. W. Evans, and P. A. Thiel, J. Chem. Phys. **138**, 071101 (2013). https://doi.org/10.1063/1.4790571

6. P. J. Feibelman, Phys. Rev. Lett. **85**, 606 (2000). https://doi.org/10.1103/PhysRevLett.85.606

7. D. R. Alfonso, A. V. Cugnini, and D. S. Sholl, Surf. Sci. **546**, 12 (2003). https://doi.org/10.1016/j.susc.2003.08.053

8. H. Walen, D.-J. Liu, J. Oh, H. Lim, J. W. Evans, C. M. Aikens, Y. Kim, and P. A. Thiel, Phys. Rev. B **91**, 045426 (2015). https://doi.org/10.1103/PhysRevB.91.045426

9. D.-J. Liu, Phys. Rev. B **81**, 035415 (2010). https://doi.org/10.1103/PhysRevB.81.035415

10. T. M. Soini and N. Rösch, Phys. Chem. Chem. Phys. **17**, 28463 (2015). https://doi.org/10.1039/C5CP04281J

11. C. Edmiston and K. Ruedenberg, Rev. Mod. Phys. **35**, 457 (1963). https://doi.org/10.1103/RevModPhys.35.457

12. *Electronic Structure of Alloys, Surfaces, and Clusters*, edited by A. Mookerjee and D. D. Sarma (Taylor & Francis, London, 2003).

13. N. Marzari, A. A. Mostofi, J. R. Yates, I. Souza, and D. Vanderbilt, Rev. Mod. Phys. **84**, 1419 (2012). https://doi.org/10.1103/RevModPhys.84.1419

14. G. Kresse and J. Hafner, Phys. Rev. B **47**, R558 (1993). https://doi.org/10.1103/PhysRevB.47.558

15. G. Kresse and J. Furthmüller, Comput. Mater. Sci. **6**, 15 (1996). https://doi.org/10.1016/0927-0256(96)00008-0

16. M. Valiev, E. Bylaska, N. Govind, K. Kowalski, T. Straatsma, H. van Dam, D. Wang, J. Nieplocha, E. Apra, T. Windus, and W. de Jong, Comput. Phys. Commun. **181**, 1477 (2010). https://doi.org/10.1016/j.cpc.2010.04.018

17. J. S. Boschen, J. Lee, T. L. Windus, J. W. Evans, and D.-J. Liu, J. Phys. Chem. C **120**, 10268 (2016). https://doi.org/10.1021/acs.jpcc.6b00829

18. J. P. Perdew, K. Burke, and M. Ernzerhof, Phys. Rev. Lett. **77**, 3865 (1996) https://doi.org/10.1103/PhysRevLett.77.3865
Erratum J. P. Perdew, K. Burke, and M. Ernzerhof, Phys. Rev. Lett. **78**, 1396 (1997). https://doi.org/10.1103/physrevlett.78.1396

19. C. Adamo and V. Barone, J. Chem. Phys. **110**, 6158 (1999). https://doi.org/10.1063/1.478522

20. J. Heyd, G. E. Scuseria, and M. Ernzerhof, J. Chem. Phys. **118**, 8207 (2003) https://doi.org/10.1063/1.1564060
Erratum J. Heyd, G. E. Scuseria, and M. Ernzerhof, J. Chem. Phys. **124**, 219906 (2006). https://doi.org/10.1063/1.2204597

21. G. Kresse and D. Joubert, Phys. Rev. B **59**, 1758 (1999). https://doi.org/10.1103/PhysRevB.59.1758

22. P. J. Hay and W. R. Wadt, J. Chem. Phys. **82**, 270 (1985). https://doi.org/10.1063/1.448799

23. A. D. McLean and G. S. Chandler, J. Chem. Phys. **72**, 5639 (1980). https://doi.org/10.1063/1.438980

24. R. Krishnan, J. S. Binkley, R. Seeger, and J. A. Pople, J. Chem. Phys. **72**, 650 (1980). https://doi.org/10.1063/1.438955

25. T. Clark, J. Chandrasekhar, G. W. Spitznagel, and P. von Ragué Schleyer, J. Comput. Chem. **4**, 294 (1983). https://doi.org/10.1002/jcc.540040303

26. F. Weigend and R. Ahlrichs, Phys. Chem. Chem. Phys. **7**, 3297 (2005). https://doi.org/10.1039/b508541a

27. D. Rappoport and F. Furche, J. Chem. Phys. **133**, 134105 (2010). https://doi.org/10.1063/1.3484283

28. F. K. Schulte, Surf. Sci. **55**, 427 (1976). https://doi.org/10.1016/0039-6028(76)90250-8

29. Y. Han and D.-J. Liu, Phys. Rev. B **80**, 155404 (2009). https://doi.org/10.1103/PhysRevB.80.155404

30. H. Walen, D.-J. Liu, J. Oh, H. J. Yang, Y. Kim, and P. A. Thiel, J. Phys. Chem. C **119**, 21000 (2015). https://doi.org/10.1021/acs.jpcc.5b06559

31. C. C. Bahr, J. J. Barton, Z. Hussain, S. W. Robey, J. G. Tobin, and D. A. Shirley, Phys. Rev. B **35**, 3773 (1987). https://doi.org/10.1103/PhysRevB.35.3773

32. M. Methfessel and A. T. Paxton, Phys. Rev. B **40**, 3616 (1989). https://doi.org/10.1103/PhysRevB.40.3616

33. R. Dronskowski and P. E. Blöchl, J. Phys. Chem. **97**, 8617 (1993). https://doi.org/10.1021/j100135a014

34. K. Ruedenberg, Rev. Mod. Phys. **34**, 326 (1962). https://doi.org/10.1103/RevModPhys.34.326

CHAPTER 4. ACCURATE *AB INITIO* POTENTIAL ENERGY CURVES AND SPECTROSCOPIC PROPERTIES OF THE FOUR LOWEST SINGLET STATES OF C_2

A paper published in *Theoretical Chemistry Accounts*, 2014, 133(2), 1425

Jeffery S. Boschen, Daniel Theis, Klaus Ruedenberg, and Theresa L. Windus

Abstract

The diatomic carbon molecule has a complex electronic structure with a large number of low-lying electronic excited states. In this work, the potential energy curves (PECs) of the four lowest lying singlet states ($X^1\Sigma^+{}_g$, $A^1\Pi_u$, $B^1\Delta_g$, and $B'^1\Sigma^+{}_g$) were obtained by high level *ab initio* calculations. Valence electron correlation was accounted for by the correlation energy extrapolation by intrinsic scaling (CEEIS) method. Additional corrections to the PECs included core-valence correlation and relativistic effects. Spin-orbit corrections were found to be insignificant. The impact of using dynamically weighted reference wave functions in conjunction with CEEIS was examined and found to give indistinguishable results from the even weighted method. The PECs showed multiple curve crossings due to the $B^1\Delta_g$ state as well as an avoided crossing between the two ${}^1\Sigma^+{}_g$ states. Vibrational energy levels were computed for each of the four electronic states, as well as rotational constants and spectroscopic parameters. Comparison between the theoretical and experimental results showed excellent agreement overall. Equilibrium bond distances are reproduced to within 0.05%. The dissociation energies of the states agree with experiment to within ~0.5 kcal/mol, achieving "chemical accuracy". Vibrational energy levels show average deviations of ~20 cm^{-1} or less. The $B^1\Delta_g$ state shows the best

agreement with a mean absolute deviation of 2.41 cm^{-1}. Calculated rotational constants exhibit very good agreement with experiment, as do the spectroscopic constants.

1 Introduction

Diatomic carbon has been studied spectroscopically in sources such as stars [1], comets [2], the interstellar medium [3], and hydrocarbon combustion reactions [4]. The molecule has a large number of low-lying excited states which have been probed in numerous studies [5-19]. One band system of note is the Swan system, which involves the $d^3\Pi_g$ - $a^3\Pi_u$ transitions. The high intensity transitions of this system led to the early inference that the $a^3\Pi_u$ state was the ground state [5]. However, the $X^1\Sigma^+{}_g$ state was later identified as the ground state with only 700 cm^{-1} separating the two states [6]. C_2 also has several low-lying singlet states, among which the Phillips system ($A^1\Pi_u$ - $X^1\Sigma^+{}_g$) is well studied. On the basis of these data, the quality of theoretical potential energy curves (PECs) can be assessed by comparing the theoretical rotational-vibrational levels with the experimental values. At the present state of the art, theoretical PECs that reproduce the ro-vibrational levels to spectroscopic accuracy (~1 cm^{-1}) or near spectroscopic accuracy (~10 cm^{-1}) are considered highly accurate.

From a theoretical perspective, the complex electronic structure of C_2 offers a challenge to *ab initio* methods [20-41]. The large number of low-lying excited states leads to several avoided crossings. Even for the ground state PEC, a reasonable description of C_2 must account for the strong multi-reference character. Indeed, the fundamental nature of the bonding in C_2 is still an active area of discussion in the literature [36,40]. By virtue of these attributes, C_2 represents a good system for testing new *ab initio* methods.

Recently, ground state PECs have been calculated using the full configuration interaction quantum Monte Carlo (FCIQMC) method [37], and the explicitly correlated internally contracted multi-reference coupled cluster method (ic-MRCCSD(F12*)) [41]. The multi-reference correlation consistent composite approach (MR-ccCA) [38] has been applied to the $X^1\Sigma^+_g$, $B^1\Delta_g$, and $B'^1\Sigma^+_g$ states. A comparison of internal contraction schemes in multi-reference configuration interaction (ic-MRCI) [39] was performed on the $X^1\Sigma^+_g$ and $B'^1\Sigma^+_g$ states. Shi *et al*. [34,35] recently performed MRCI calculations to obtain the PECs for several ($X^1\Sigma^+_g$, $A^1\Pi_u$, $B^1\Delta_g$, $B'^1\Sigma^+_g$, $C^1\Pi_g$, $D^1\Sigma^+_u$, $E^1\Sigma^+_g$, and $1^1\Delta_u$) electronic states of C_2.

An accurate description of this molecule must account for both static correlation at the reference level as well as dynamic correlation using a highly correlated method. To account for static correlation within a group of states (ground state and excited states), state-averaged multi-configurational self-consistent field (SA-MCSCF) calculations are commonly used. Often, the states are weighted evenly. However, to ensure smoothly varying reference PECs, dynamically weighted (DW-MCSCF) [42] procedures are also used. The impact of using dynamical weighting versus even weighting on the dynamic correlation will be examined in this work.

In order to recover dynamic correlation, the present study uses the method of Correlation Energy Extrapolation by Intrinsic Scaling (CEEIS) [43-45]. This approach has been used to obtain highly accurate ground state PECs for the first-row diatomics B_2, O_2, F_2, from which rotational-vibrational energy levels with near spectroscopic accuracy were obtained [46-48]. In contrast to the other *ab initio* approaches used recently for C_2, the present approach focuses on recovering the correlation energy of higher excitation levels by CEEIS extrapolation for smaller basis sets, and then extrapolating to the complete basis set limit. Using a generalized form of this method that extrapolates correlation energies for multiple electronic states, the PECs of the four lowest energy singlet states of C_2 ($X^1\Sigma^+{}_g$, $A^1\Pi_{u}$, $B^1\Delta_g$, $B'^1\Sigma^+{}_g$) are obtained in this study. The spectroscopic constants and rotational-vibrational levels corresponding to these curves are compared to the experimental values.

2 Method

The PEC calculations for the dissociation of C_2 in this work follow the general method developed by Bytautas *et al.* in earlier studies on the diatomics F_2, O_2, and B_2 [46,49,50,47,51,48]. In addition to the $X^1\Sigma^+{}_g$ ground state, PECs are calculated for the three lowest lying excited singlet states: $A^1\Pi_u$, $B^1\Delta_g$, and $B'^1\Sigma^+{}_g$. The calculations rely on the CEEIS method to obtain the valence correlation to near full configuration interaction (FCI) accuracy. Additional corrections due to core-valence correlation and relativistic effects are added to achieve near spectroscopic accuracy. Where feasible, complete basis set (CBS) extrapolations are performed. All *ab initio* electronic structure calculations were completed using the GAMESS program suite [52].

2.1 Zeroth order wave function

An accurate description of the C_2 dissociation requires a multi-reference wave function to capture the static correlation of the system. Of particular note is the strong multi-configurational character of the ground state even at the experimental equilibrium distance of 1.242 Å where the primary determinant is $\left|(core)2s_g^2 2s_u^2 1p_{x_u}^2 1p_{y_u}^2\right\rangle$. However, a doubly excited configuration $\left|(core)2\sigma_g^2 1\pi_{x_u}^2 1\pi_{y_u}^2 3\sigma_g^2\right\rangle$ has a coefficient of 0.37, which is unusually large for a ground state molecule at equilibrium. The excited states also show multi-configurational character (see the

Supporting Information for more details). Therefore, the reference energies and orbitals for all subsequent calculations were obtained from MCSCF calculations in the full valence configuration space. In C_2, the valence space consists of the full optimized reaction space (FORS) [53-56] of eight electrons in eight orbitals (CAS(8,8) in the complete active space notation [57]). The core consists of four electrons in two core orbitals. In the D_{2h} symmetry group used by GAMESS for calculations on linear molecules, three of the investigated states ($X^1\Sigma^+_g$, $B^1\Delta_g$, and $B'^1\Sigma^+_g$) belong to the fully symmetric A_g irreducible representation (irrep). The reference functions of these states were obtained by state-averaged MCSCF (SA-MCSCF) calculations. The $A^1\Pi_u$ state (B_{2u} irrep in D_{2h}) was calculated separately by a state-specific MCSCF.

In addition to the evenly weighted SA-MCSCF calculations over the three states (referred to as SA-MCSCF for the rest of the paper), dynamically weighted MCSCF (DW-MCSCF) functions were also optimized at various bond distances. The DW-MCSCF method of Deskevich *et al*. [42] minimizes a weighted average of the state energies. The weight assigned to state i is given by the formula:

$$w_i = sech^2[-\beta(E_i - E_0)] = 4/(2 + e^{2\beta(E_i - E_0)} + e^{-2\beta(E_i - E_0)})$$

where β is an adjustable parameter, E_i is the energy of state i, and E_0 is the ground state energy. The reported results used β^{-1} = 2.0 eV (chosen from the recommended range of values from Deskevich *et al.*), other values were tested and showed similar results. DW-MCSCF has been shown to reduce discontinuities and smooth out potential energy surfaces. The impact of using dynamically weighted reference orbitals with the highly correlated CEEIS method will be examined below.

The reference calculations were performed using Dunning's series of correlation consistent basis sets, cc-pVXZ [58,59] where $X = 4, 5,$ and 6. The reference energies were extrapolated to the complete basis set limit using the three point formula [60,61]:

$$E(X) = E(CBS) + aexp(-\alpha X)$$

where the three unknowns [$E(CBS)$, a, and α] are determined by calculating $E(X)$ for each of the three different basis sets.

2.2 Valence correlation

CEEIS method for a single state

The dynamic valence correlation was determined using the CEEIS method, developed by Ruedenberg and Bytautas [43-45] to approximate the FCI energy. Only a brief description of the method is included here for context. The FCI energy is expressed as a sum of contributions from higher and higher levels of configurational excitation, until all possible configurations have been included. However, since the rapid increase in the number of configurations with increasing system size makes full CI calculations prohibitively expensive for most applications, excitation levels beyond the doubles are typically ignored in favor of the truncated CISD method. The CEEIS method estimates the higher excitation energy contributions from these truncated calculations by means of an extrapolation technique.

The CEEIS procedure can be carried through with respect to single determinant Hartree-Fock reference functions or multi-determinant MCSCF reference functions. A set of correlating virtual orbitals is needed *that is ordered according to decreasing importance*. To this end, the pseudo-natural orbitals [62], i.e. the natural orbitals from a multi-reference CISD calculation (MR-CISD), ordered by their occupation numbers have been found to provide an effective set for the CEEIS procedure. The pseudo-natural orbitals used are produced by diagonalizing only the virtual block of the one-particle density matrix. For the rest of this paper, these orbitals will be referred to as natural orbitals even though the full density matrix has not been diagonalized. The number of correlating orbitals, M, is equal to the total number of virtual orbitals.

In the CEEIS procedure, the values of the contributions from the double and triple excitations are used to estimate the energy changes due to the higher excitation levels $x = 4, 5, 6$ etc., i.e. quadruple, quintuple, and sextuple excitations etc. Note that x is used to denote the excitation level whereas X was used above to denote the basis set size. Let $E(x)$ be the CI energy when all configurations up to and including excitation level x are taken into account. The *incremental* energy contributions due to the inclusion of excitation level x are then defined as

$$\Delta E(x) = E(x) - E(x-1) \qquad \text{for } x > 2$$

e.g., $\Delta E(3)$ would be the difference between the CISDT and CISD energies.

Bytautas and Ruedenberg [43] found that the energy change $\Delta E(x)$ can be related to the energy change from excitations two levels lower, i.e. $\Delta E(x\text{-}2)$. For example, the energy change due to quadruple excitations can be estimated from that due to double excitations. The relation is established by considering correlation energy increments that are analogous to $\Delta E(x)$, but are instead obtained from CI calculations with excitations into smaller subsets of m ($<M$) virtual orbitals. If these increments are denoted as

$$\Delta E(x|m) = E(x|m) - E(x-1|m)$$

then $\Delta E(x|m)$ manifestly becomes $\Delta E(x)$ when $m \rightarrow M$. Bytautas and Ruedenberg showed that, in all systems that were examined, the following linear relationship holds *with respect to the variation of m:*

$$\Delta E(x|m) = a_x \Delta E(x-2|m) + c_x$$

The linear relationship is not observed at very small values of m, but is seen to hold for m running from some threshold m_0 to M. Consequently, the following extrapolation is found to be effective. Values of $\Delta E(x|m)$ and $\Delta E(x\text{-}2|m)$ are calculated *for a range of m values considerably smaller than M*. From these data, the coefficients a_x and c_x in the linear relation are determined by a least-mean-squares fit. The known value of $\Delta E(x\text{-}2)$ is then inserted into the linear equation for $\Delta E(x\text{-}2|m{=}M)$ and, thereby, an extrapolated value is produced for the unknown value of $\Delta E(x) = \Delta E(x|m{=}M)$. The extrapolations must be performed with calculations involving at least m_0 virtual orbitals. Careful selection of the range of m values is necessary to ensure an extrapolation of high accuracy. Detailed information on the choice of effective ranges can be found in past work describing the CEEIS method [43-47].

The contributions from the singles and double excitations [$\Delta E(x{=}2) = E(x{=}2) - E(x{=}0)$] are computed exactly. If practical, this is also done for the contributions from the triple excitations. If, however, a prohibitive effort is required for the latter, then the value of $\Delta E(x{=}3)$ is also obtained by extrapolation from the singles and double excitations by an analogous linear extrapolation. The range of m for this extrapolation typically extends to higher values.

CEEIS method for a set of several states

Bytautas et al. [48] also showed that the CEEIS method can be applied simultaneously to several states of the same symmetry. Building upon that observation, the analogous multiple state CEEIS approach has been developed further in considerable detail and has been incorporated into GAMESS [63]. Appropriate reference functions are obtained from a SA-MCSCF calculation that includes all the states of interest in the state averaging. Correlating virtual orbitals are obtained from a preliminary MRCISD calculation. In contrast to the single state case, the one-particle density matrices of the MRCISD wave functions are averaged over the states of interest and the virtual block is diagonalized to give state averaged natural orbitals. These averaged natural orbitals form the set of M correlating virtual orbitals used in the multistate CEEIS procedure. Multiple-root CI calculations with higher excitations (CISDT, CISDTQ, …) are then computed for a prespecified range of m-values as in the single-state case. The eigenvalues of these calculations provide the values $\Delta E_k(x|m)$ for each of the states $|k\rangle$ under investigation, which are then used to extrapolate the total contribution that excitation x will make to the full CI energy for each state. The computation and extrapolation of the multiple states has been automated within GAMESS. However, the user still needs to be careful to correctly identify the CI states when the states are very close in energy. The energy order of near degenerate states may change as calculations are performed throughout the range of correlating orbitals, m. Therefore, one must ensure that all of the energy differences used in the extrapolations are associated with the same reference wave function (*i.e.* have the same dominant electronic configurations).

CEEIS procedure for C_2

For the CEEIS calculations on C_2, the full valence CASSCF(8,8) wave functions described above are used as a reference. The correlating virtual orbitals used are the natural orbitals from MR-CISD calculations with respect to the CASSCF(8,8) references. For the reference functions of the three states $X^1\Sigma^+_g$, $B^1\Delta_g$, and $B'^1\Sigma^+_g$, which are obtained from a SA-MCSCF calculation in the A_g irrep, the correlating orbitals are obtained from the virtual block of the state-averaged density matrix. The number of virtual orbitals is $M = 50$ and $M = 100$ for the cc-pVTZ and cc-pVQZ basis sets, respectively.

The double and triple excitation contributions were calculated exactly in all cases, except for the triple excitations in the cc-pVQZ basis, which was too expensive. These were obtained by extrapolation from the double excitations, as discussed above. The range of virtual orbitals used for the extrapolation of the triples contribution was *m*:{18-25,30,35}.

The CEEIS procedure was performed up to sextuple excitations. For the extrapolation of the quadruples contribution, the range of correlating virtual orbitals used was *m:*{18-25}. For the quintuple and sextuple excitations, the ranges were *m:*{13-17} and {10-14} respectively. In addition, it is important to note that *m* is chosen so that degenerate orbitals remain paired.

CBS extrapolation of the correlation energy was performed using the cc-pVXZ bases and the two point formula [64,65]:

$$\Delta E_{CORR}(X) = \Delta E_{CORR}(CBS) + a_c X^{-3}$$

where ΔE_{CORR} is the difference between the reference and the estimated FCI energy. Using X=3 and 4, the CBS limit for the correlation energy was determined. Addition of the CBS correlation energy to the CBS reference energy yielded the valence correlated approximate FCI PECs. The uncertainty in the CEEIS energies was estimated to be ~0.1 millihartree**.**

2.3 Corrections to the PECs

Past studies [50,51] have shown that reproducing the rotational-vibrational energy levels to near spectroscopic accuracy requires additional corrections to the valence correlated PECs. The first contribution is the inclusion of core electron correlation. As in previous studies, these effects were captured using MRCISD calculations including the Davidson correction (+Q) [66]. The Dunning triple-zeta basis set modified for core-valence effects, cc-pCVTZ [58], was used. The reference orbitals for the MRCISD+Q calculations were taken from a full valence

CASSCF(8,8) calculation. In the valence only MRCISD+Q, excitations are only allowed from the original CAS(8,8) space. The valence plus core MRCISD+Q calculation allowed single and double excitations from a CAS(12,10) space that included the core orbitals. The core-valence correlation correction is obtained from the difference between these two energies.

Relativistic effects are accounted for by two corrections. The first is the scalar relativistic contribution, which was obtained using the one-electron Douglas-Kroll (DK) method [67]. The transformation to third order (DK3) [68,69] approach was applied at the CASSCF(8,8) level. A modified DK-contracted basis, cc-pCVQZ [70] was used. The second relativistic correction is due to the spin-orbit (SO) coupling. SO coupling effects were computed using the full one- and two-electron Breit-Pauli operator [71]. Equivalent orbitals were obtained through SA-MCSCF calculations over the 18 states with $M_S = 0$ that dissociate to the ground state ^{3}P atomic terms. The active space for these calculations was a reduced valence space including only the molecular orbitals that arise from the 2p atomic orbitals (CAS(4,6)). These CAS-CI states form the basis for the SO calculation. Addition of the Breit-Pauli operator introduces off-diagonal terms into the Hamiltonian matrix, which generate the spin-orbit couplings between states. Diagonalizing the Hamiltonian produces spin-mixed states. The energy lowering of these states relative to the CAS-CI states provides the SO correction to the PECs. The cc-pVQZ basis was used for these calculations. A more detailed description of the procedure has been given for the molecules F_2 and O_2 [49,51]. Adding all corrections to the energies calculated with the CEEIS method yields the final potential energy curves.

2.4 Fitting Continuous Functions to PECs

In order to determine spectroscopic constants and rotational-vibrational levels for comparison with experiment, the potential energy curves must be fitted to a continuous function. Bytautas and Ruedenberg have used even-tempered Gaussian functions to fit PECs of the diatomics O_2, F_2, and B_2 [50,51,48]. The terms of the expansion are found using linear least squares regression. This approach yielded analytic curves that show high quality fits with two of the states of interest: $A^1\Pi_u$ and $B^1\Delta_g$ (mean absolute deviations of 0.044 and 0.037 millihartree).

However, the even-tempered Gaussian functions fit to the two Σ^+_g states showed mean absolute deviations (MADs) an order of magnitude greater (0.219 and 0.296 millhartree). Increasing the number of Gaussians in the expansion did not change the quality of the fit to the *ab initio* data. The even-tempered Gaussian expansions proved incapable of capturing the irregular shape of the Σ^+_g curves due to an avoided crossing which occurs near 1.70 Å on the PECs. Presumably, these local distortions are difficult to represent in terms of reasonably simple analytic (i.e. everywhere infinitely differentiable) functions. As an alternative, cubic splines were fitted to the *ab initio* data using the module VIBROT within MOLCAS [72]. The PECs were constructed from 44 *ab initio* calculations along the dissociation path. The points range from 0.9 to 6.0 Å with an additional point at 20.0 Å to determine the dissociated values. The points were chosen to adequately describe both the minimum and the avoided crossing region of the potential and to provide a sufficient density of points to fit the cubic spline.

2.5 Calculation of Rotational-Vibrational Energy Levels

The rotational-vibrational energy levels are found by solving the nuclear Schrödinger equation for the analytical representations of the PECs. When the analytical function was an even-tempered Gaussian expansion, the discrete variable representation (DVR) method [73] was used to solve for the rotational-vibrational levels. For the functions using cubic splines, the Schrödinger equation was solved using Numerov's method [74] (in the program VIBROT) [72]. The two different approaches yielded similar results for the $^1\Pi_u$ and B $^1\Delta_g$ states (deviations ~1 cm^{-1} and ~10 cm^{-1} respectively). However, the energy levels obtained from an even-tempered Gaussian fit and a cubic spline for the $\Sigma^+{}_g$ states show large disagreement (~100 cm^{-1}). This supports the inference that the even-tempered Gaussian expansion cannot describe the avoided crossing exhibited by the $\Sigma^+{}_g$ states. The spectroscopic constants were determined by least-mean-squares fitting to the rotational-vibrational levels [9].

3 Results

3.1 Potential energy curves

The *ab initio* PECs curves are presented in Figure 1. These energies include the CBS extrapolated reference energies, the CBS extrapolated CEEIS valence correlation energies, the core-valence correlation, and the relativistic corrections. These curves reveal the complexity of the electronic structure of C_2. At distances longer than about 1.6 Å, all four states are close in energy. The $B^1\Delta_g$ state is seen to drop below both the $X^1\Sigma^+{}_g$ and $A^1\Pi_u$ states near 1.6 Å. Another aspect of interest is the avoided crossing between the two $\Sigma^+{}_g$ states which occurs in the region of R = 1.6 Å. This avoided crossing is accompanied by a change in the dominant configurations of the two states as well as a distortion of the shapes of the curves. This distortion is the likely explanation for the failure of the even-tempered Gaussian expansion to accurately fit the $\Sigma^+{}_g$ states. As the two atoms separate, all four of the states become degenerate, dissociating to the two carbon atoms in their ^3P ground states.

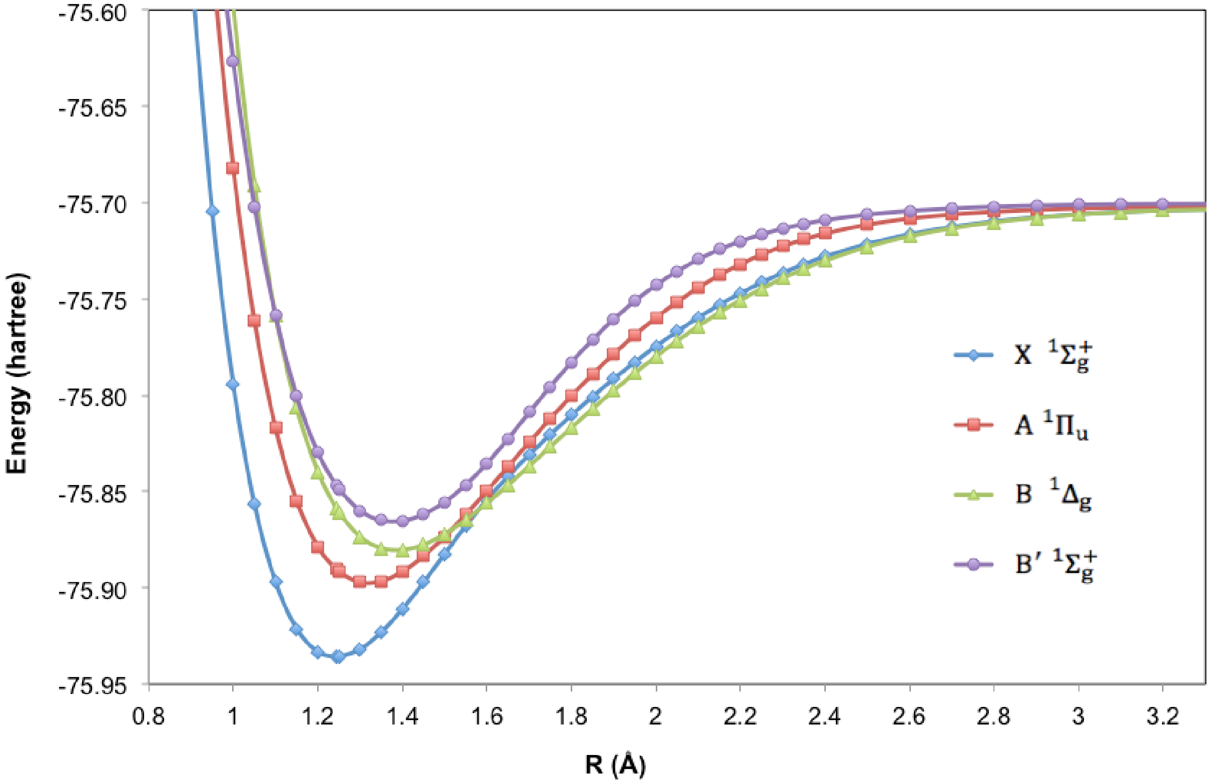

Fig. 1 *Ab initio* PECs of the lowest energy singlet states of C_2, energies obtained using CBS extrapolated reference and CEEIS valence correlation energy with core-valence correlation and relativistic corrections.

3.2 Dynamic versus even weighting in averaging the reference states

The impact of using DW-MCSCF versus SA-MCSCF reference orbitals with the CEEIS method was examined. CEEIS energies were calculated using the cc-pVTZ basis and DW reference orbitals at 10 points along the dissociation curve. The energy differences between the SA and DW calculations are reported in Table 1. While the reference energies at the MCSCF level are very sensitive to the weighting scheme, the CEEIS energies including dynamic correlation are not significantly changed. Furthermore, the DW weights quickly converge to a near even weighted SA due to the decrease in energy differences between states as the separation distance increases. The maximum impact on the CEEIS energies (~0.2 millihartree) is of the same order as the uncertainty in the CEEIS extrapolations. For most of the PEC, the change due to using a DW-MCSCF reference is well below the uncertainty in the CEEIS method. Since the FCI energy is independent of the reference wave function, the observed insensitivity to the weighting of states in determining the reference orbitals confirms the soundness of the CEEIS method.

Table 1 Energy differences[a] (millihartree) between SA and DW at the MCSCF reference and CEEIS level.

	MCSCF			CEEIS		
R (Å)	$X^1\Sigma^+_g$	$B^1\Delta_g$	$B'^1\Sigma^+_g$	$X^1\Sigma^+_g$	$B^1\Delta_g$	$B'^1\Sigma^+_g$
1.0	13.720	-50.437	-33.531	-0.016	-0.213	-0.079
1.2	12.151	-28.189	-23.413	0.024	-0.199	-0.166
1.25	9.534	-15.148	-12.203	0.028	-0.147	-0.118
1.4	2.507	-1.935	-1.368	0.017	-0.034	-0.026
1.6	0.092	-0.057	-0.037	0.016	-0.018	0.001
1.8	0.023	0.074	-0.101	0.003	0.003	-0.001
2.0	0.042	0.071	-0.118	0.003	0.003	-0.001
2.4	0.007	0.009	-0.016	0.000	0.000	0.000
2.8	0.001	0.001	-0.002	-0.004	0.004	0.000
3.2	0.000	0.000	0.000	-0.005	0.005	0.000

[a] Reported here as the E(SA) – E(DW).

These results are in agreement with Zeng *et al*. [75] who found little difference between DW- and SA-MCSCF orbitals when used in conjunction with multi-configurational quasidegenerate perturbation theory (MCQDPT). Their work on the Sn_2^+ dissociation showed minimal change in the spectroscopic constants and vibrational energy levels. Based on this previous study and the aforementioned results, the C_2 PECs used in the present study were obtained using SA-MCSCF orbitals.

3.3 Contributions to the PECs

As described above, the PECs include three additional corrections beyond the valence correlated CEEIS method. Tables with complete information for each contribution at each point on the PECs are provided in the Supporting Information. In the following, all energies are given relative to the value at dissociation.

The most significant correction is the inclusion of the core-valence correlation. Each of the four states exhibits the same qualitative trend in and similar quantitative contributions from the core-valence correlation. The following discussion will therefore focus on the ground state. The core-valence correction grows as the atoms move closer together, and the largest value in these calculations was -6.870 millihartree at 0.9 Å. At equilibrium (1.24244 Å) the correction was -2.906 millihartree.

Of the two relativistic corrections, the scalar Douglas-Kroll method has a greater impact on the shape of the PECs. At most bond distances, the DK3 correction is positive relative to the value at dissociation. For the ground state, this repulsive effect is strongest at 1.4 Å where the value is 0.335 millihartree. As the bond length increases the correction smoothly decreases. As the bond length decreases from 1.4 Å, the DK3 correction decreases and eventually drops below the dissociated value as the repulsive wall of the PEC is approached. This trend is observed in all the calculated states, although the energy changes are somewhat smaller for the excited states.

The second relativistic contribution, the spin-orbit coupling, causes no significant change in the shape of the PECs. For every state the contribution is effectively zero inside the potential wells. The SO effects do become nonzero at bond lengths longer than 2.3 Å. As the carbon atoms become well separated, the SO effect lowers the energy of the system. However, even at the dissociation limit, the energy difference is quite small. For the ground state the difference in energy due to SO coupling between equilibrium and dissociation is only 0.246 millihartree. The impact is slightly smaller for the other three states but on the same order of magnitude.

3.4 Comparison of theoretical and experimental results

Equilibrium bond distance and electronic energies

Table 2 reports the experimental and theoretical values for the equilibrium bond distance (R_e), for the dissociation energy from the potential curve minimum (D_e), and for the adiabatic electronic excitation energy from the ground state (T_e). Excellent agreement between experiment and theory is seen for the equilibrium bond distances (percent differences of 0.05% or less). The experimental value of D_e for the excited states is obtained by adding the experimental values for T_e to the experimentally determined ground state D_e. The theoretical dissociation energies deviate from experiment by less than 0.6 kcal/mol, demonstrating "chemical accuracy". The dissociation energies in this work show better agreement with the most recent experimental values [76] than other recent high level *ab initio* studies [34,35,38]. The theoretical adiabatic excitation energies are in close agreement with experiment, showing percent differences of 0.27, 0.66 and 0.11% for the $A^1\Pi_u$, $B^1\Delta_g$, and $B'^1\Sigma^+_g$ states, respectively.

Table 2 Experimental[a] and theoretical spectroscopic constants of C_2 singlet states

$X^1\Sigma^+_g$

	Experiment	Theory	Difference
R_e (Å)	1.24244	1.2431	0.00066
D_e (kcal/mol)[b]	147.8	147.42	-0.38
T_e (cm^{-1})	-	-	-
ω_e (cm^{-1})	1855.01	1850.91	-4.10
$\omega_e x_e$ (cm^{-1})	13.5547	10.5857	-2.969
B_e (cm^{-1})	1.82010	1.82008	-0.00002
α_e (cm^{-1})	0.018012	0.0177588	-0.0002532
D_{rot} (10^{-6} cm^{-1})	6.9640	6.8950	-0.0690
β_e (10^{-8} cm^{-1})	6.41	9.59	3.18

$A^1\Pi_u$

	Experiment	Theory	Difference
R_e (Å)	1.318311	1.3176	-0.000711
D_e (kcal/mol)[c]	123.8	123.41	-0.39
T_e (cm^{-1})	8391.4085	8413.9989	22.5904
ω_e (cm^{-1})	1608.20	1616.52	8.32
$\omega_e x_e$ (cm^{-1})	12.0597	13.1386	1.0789
B_e (cm^{-1})	1.61663	1.61693	0.00030
α_e (cm^{-1})	0.0169691	0.0168091	-0.00016
D_{rot} (10^{-6} cm^{-1})	6.5086	6.4856	-0.0230
β_e (10^{-8} cm^{-1})	2.53	3.12	0.59

Table 2 continued

$B^1\Delta_g$

	Experiment	Theory	Difference
R_e (Å)	1.38548	1.3851	-0.00038
D_e (kcal/mol)[c]	113.3	112.73	-0.57
T_e (cm^{-1})	12082.3360	12162.6256	80.2896
ω_e (cm^{-1})	1407.47	1403.23	-4.24
$\omega_e x_e$ (cm^{-1})	11.47937	9.7608	-1.71857
B_e (cm^{-1})	1.46369	1.46342	-0.00027
α_e (cm^{-1})	0.0168161	0.0156176	-0.0011985
D_{rot} (10^{-6} cm^{-1})	6.3188	6.3475	0.0287
β_e (10^{-8} cm^{-1})	1.492	0.559	-0.933

$B'^1\Sigma^+_g$

	Experiment	Theory	Difference
R_e (Å)	1.37735	1.3771	-0.00025
D_e (kcal/mol)[c]	103.8	103.43	-0.37
T_e (cm^{-1})	15409.139	15425.9939	16.8549
ω_e (cm^{-1})	1424.12	1413.15	-10.97
$\omega_e x_e$ (cm^{-1})	2.57113	1.62016	-0.95097
B_e (cm^{-1})	1.481006	1.48053	-0.00048
α_e (cm^{-1})	0.011752	0.012027	0.000275
D_{rot} (10^{-6} cm^{-1})	6.8596	6.4618	-0.3978
β_e (10^{-8} cm^{-1})	-15.81	-19.55	-3.74

Table 2 continued

[a] Experimental values from references [11,12] unless otherwise noted

[b] Experimental values from reference [76]

[c] Experimental value obtained by adding ground state D_e plus excited state T_e

Vibrational spectrum

Table 3 shows a comparison between the experimental vibrational levels [11,12] and the theoretical results obtained in this work. The energy levels reported are given relative to the minimum of the PEC of each respective state. The MADs of the four states are on the order of 10-20 cm^{-1}, demonstrating the near-spectroscopic accuracy of the *ab initio* PECs. However, there is a clear trend of decreasing accuracy with increasing v. Particularly good agreement (MAD = 2.41 cm^{-1}) is obtained for the $B^1\Delta_g$ state, while the worst agreement is seen for the $B'^1\Sigma^+_g$ state. Also included in Table 3 are the energy differences between the vibrational levels ($G(v)$ - $G(v\text{-}1)$). These vibrational spacings show smaller deviations between theory and experiment, however they cumulatively lead to the larger deviations observed in the absolute vibrational levels. In Table 4, additional *ab initio* vibrational levels for each state (up to v = 24) are reported. The higher vibrational levels currently lack experimental values for comparison. All bound vibrational levels for each PEC are listed in the Supporting Information: 57 levels for the $X^1\Sigma^+_g$, 54 for the $A^1\Pi_u$ states, 49 for the $B^1\Delta_g$ state, and 36 for the $B'^1\Sigma^+_g$ state.

Table 3 Comparison of theoretical and experimental[a] vibrational energy levels of C_2 singlet states (Energies in cm^{-1})

	$G(v)$			$G(v)$ - $G(v\text{-}1)$		
$X^1\Sigma^+_g$						
v	Experiment	Theory	Difference	Experiment	Theory	Difference
0	923.98	919.49	-4.49	-	-	-
1	2751.47	2749.85	-1.62	1827.48	1830.36	2.88
2	4550.67	4555.98	5.31	1799.20	1806.13	6.93
3	6320.57	6330.44	9.87	1769.91	1774.46	4.55
4	8060.33	8071.98	11.65	1739.76	1741.54	1.78
5	9768.11	9782.08	13.97	1707.77	1710.10	2.33
6	11441.95	11458.92	16.97	1673.84	1676.84	3.00
MAD			9.12			3.58
$A^1\Pi_u$						
v	Experiment	Theory	Difference	Experiment	Theory	Difference
0	801.10	806.64	5.54	-	-	-
1	2385.15	2394.98	9.83	1584.05	1588.34	4.29
2	3944.97	3959.64	14.67	1559.83	1564.66	4.83
3	5480.53	5499.90	19.37	1535.56	1540.26	4.70
4	6991.74	7014.93	23.19	1511.21	1515.03	3.82
5	8478.54	8504.38	25.84	1486.79	1489.45	2.66
MAD			16.41			4.06
$B^1\Delta_g$						
v	Experiment	Theory	Difference	Experiment	Theory	Difference
0	700.95	699.57	-1.38	-	-	-
1	2085.49	2081.44	-4.05	1384.54	1381.87	-2.67
2	3447.16	3445.98	-1.18	1361.67	1364.54	2.87
3	4786.03	4786.06	0.03	1338.87	1340.08	1.21
4	6102.15	6104.61	2.46	1316.12	1318.55	2.43
5	7395.60	7400.96	5.36	1293.45	1296.35	2.90
MAD			2.41			2.42

Table 3 continued

$B'^1\Sigma^+_g$

v	Experiment	Theory	Difference	Experiment	Theory	Difference
0	712.74	706.83	-5.91	-	-	-
1	2133.23	2116.28	-16.95	1420.48	1409.45	-11.03
2	3552.75	3527.01	-25.74	1419.52	1410.73	-8.79
3	4974.08	4936.74	-37.34	1421.34	1409.73	-11.61
MAD			21.48			10.48

[a] Experimental values from references [11,12]

The theoretical vibrational levels of this work for the $X^1\Sigma^+_g$ and $A^1\Pi_u$ states show reduced deviations compared to work by Zhang *et al*. [34] (MADs of 13.1 and 27.60 cm^{-1} for the $X^1\Sigma^+_g$ and $A^1\Pi_u$ states, respectively, for the Zhang work). However, the same group [35] reports vibrational levels for the $B^1\Delta_g$ and $B'^1\Sigma^+_g$ states which show better agreement to experiment (MADs of 1.37 and 5.15 cm^{-1}, respectively) than this work. Kokkin *et al*. [30] have obtained vibrational levels for the $X^1\Sigma^+_g$ state which are of similar accuracy (MAD 8.43 cm^{-1}) to this work, while their results for the $A^1\Pi_u$ state show better accuracy (MAD 0.77 cm^{-1}) than this work. All of these other studies employed internally contracted MRCISD calculations using the aug-cc-pV6Z basis and included core-valence correlation and scalar relativistic corrections.

It is worth noting the contribution that each additional correction (core-valence correlation and relativistic effects) makes towards achieving accurate vibrational levels. Including core-valence correlation leads to a ~10-20 cm^{-1} reduction in the MAD for each of the states. The scalar relativistic correction (DK3) is less important, with a ~1 cm^{-1} improvement in the MAD of the vibrational levels. Finally the SO contribution was seen to make no difference in the vibrational levels of the C_2 singlet states. This is not surprising given the magnitude of the

SO correction, and the distances at which the contribution becomes significant. The low levels of the vibrational manifold are not strongly impacted by the SO effects that arise near dissociation. The unimportance of SO effects for determining the vibrational levels of C_2 was also seen by Kokkin *et al*. [30] in calculations on the $X^1\Sigma^+_g$ and $A^1\Pi_u$ states.

Table 4 – Theoretical vibrational levels of C_2 singlet states. (Energies in cm^{-1}, relative to the potential curve minimum of each state)

v	$X^1\Sigma^+_g$	$A^1\Pi_u$	$B^1\Delta_g$	$B'^1\Sigma^+_g$
0	919.49	806.64	699.57	706.83
1	2749.85	2394.98	2081.44	2116.28
2	4555.98	3959.64	3445.98	3527.01
3	6330.44	5499.90	4786.06	4936.74
4	8071.98	7014.93	6104.61	6344.88
5	9782.08	8504.38	7400.96	7749.06
6	11458.92	9968.70	8674.54	9146.88
7	13100.36	11408.50	9924.90	10535.60
8	14702.82	12823.87	11152.23	11911.95
9	16261.81	14214.39	12356.91	13271.97
10	17773.27	15579.26	13539.17	14611.66
11	19234.77	16918.24	14698.87	15927.89
12	20646.17	18231.53	15835.77	17219.13
13	22009.10	19519.03	16949.92	18484.20
14	23326.85	20780.33	18041.63	19721.42
15	24603.22	22015.14	19110.63	20929.34
16	25841.91	23223.37	20156.30	22106.73
17	27046.53	24404.87	21179.08	23252.29
18	28219.42	25559.47	22180.00	24364.26
19	29362.03	26687.03	23158.49	25440.71
20	30475.54	27787.42	24113.15	26480.12
21	31561.58	28860.20	25044.74	27481.17
22	32620.69	29904.57	25954.80	28442.21
23	33652.70	30919.72	26842.17	29361.71
24	34658.45	31905.30	27704.66	30238.18

Rotational Constants

Table 5 reports the rotational constants (B_v and D_v) from both experiment [11,12] and this work. The rotational energy can be expanded [9] as

$$F_v(J) = B_v[J(J+1)] - D_v[J(J+1)]^2 + \cdots$$

A least squares fit to the lowest 10 rotational levels at each vibrational level was used to determine the theoretical values of B_v and D_v. The overall agreement between the rotational constants of this work and experiment is quite good. For B_v the largest deviation of the theoretical values from the experimental ones are ~0.1-0.2 percent, while most of the deviations are smaller than this. The D_v values are significantly smaller than B_v (reported in 10^{-6} cm^{-1}) and are therefore expected to be less accurate on a percent basis. The agreement between theory and experiment is still very good, with the exception of the highest energy $B'^1\Sigma^+_g$ state (with a 16% deviation). For the other states, the percent difference between the values is at worst ~1% and for most values is significantly lower.

Spectroscopic Constants

The relationship between the ro-vibrational levels and the spectroscopic constants is given by the Dunham expansion in terms of (v + 1/2) [9]:

$$G(v) = \omega_e\left(v+\frac{1}{2}\right) - \omega_e x_e\left(v+\frac{1}{2}\right)^2 + \cdots$$

$$B_v = B_e - \alpha_e\left(v+\frac{1}{2}\right) + \cdots$$

$$D_v = D_{rot} + \beta_e\left(v+\frac{1}{2}\right) + \cdots$$

Using this expansion, the equilibrium spectroscopic constants given in Table 2 were obtained by a least mean squares fitting to the energy levels in Table 3 and the rotational constants in Table 5. The fittings were calculated using VIBROT [72].

The theoretical values for the first terms in each of the expansions: ω_e, B_e, and D_{rot}, exhibit very small deviations from experiment (average percent differences of 0.45, 0.02, and 1.9% respectively). The B_e results in particular show excellent agreement. The average percent difference for D_{rot} is 0.6% if the $B'^1\Sigma^+_g$ state is excluded. The second terms in the expansions are less accurate since the values themselves are quite small to begin with. However the qualitative trends are correct, and the agreement for the α_e values is still quite good (average difference 3.0%), while the differences for $\omega_e x_e$ and β_e exhibit average differences of 21 and 40%, respectively.

The accuracy of the spectroscopic constants in Table 2 is comparable to other recent high level *ab initio* studies. Some of these studies (using ic-MRCISD and MR-ccCA) [30,34,38] have determined the ground state harmonic frequency (ω_e) with absolute deviations from experiment of 1.5 cm^{-1} or less, while others using ic-MRCISD and ic-MRCCSD(F12*) methods [32,41] have shown deviations of ~6-8 cm^{-1}. The deviation in the present work is 4.1 cm^{-1}. The first anharmonicity ($\omega_e x_e$) of the $X^1\Sigma^+_g$ state in this work shows slightly worse agreement with experiment (3 cm^{-1} difference) than the previous [30,34,39,41] theoretical results (~1 cm^{-1} or better). In the $A^1\Pi_u$ state, the 8 cm^{-1} deviation in the current results for ω_e matches the deviation in reference 34, while two previous studies [30,38] have achieved ~1 cm^{-1} deviations from experiment. The $\omega_e x_e$ result for the $A^1\Pi_u$ state in this work (Table 2) is of a similar quality to past work [30,34]. The current results for the two highest energy states studied ($B^1\Delta_g$ and $B'^1\Sigma^+_g$) also compare well with the previous work [35,38]. All theoretical harmonic frequencies exhibit small

Table 5 Comparison of theoretical and experimental[a] rotational constants of the C_2 singlet states

(Energies of B_v in cm^{-1}, D_v in 10^{-6} cm^{-1})

	B_v			D_v		
$X^1\Sigma^+_g$						
v	Experiment	Theory	Difference	Experiment	Theory	Difference
0	1.81107	1.81106	-0.00001	7.00315	7.00540	0.00225
1	1.79288	1.79329	0.00041	7.05398	6.98626	-0.06772
2	1.77434	1.77397	-0.00037	7.0944	7.12137	0.02697
3	1.75540	1.75534	-0.00006	7.2066	7.25091	0.04431
4	1.73590	1.73590	0.00000	7.2941	7.27346	-0.02064
5	1.71570	1.71601	0.00031	7.499	7.40893	-0.09007
6	1.69381	1.69553	0.00172			
$A^1\Pi_u$						
v	Experiment	Theory	Difference	Experiment	Theory	Difference
0	1.60813	1.60871	0.00058	6.52569	6.51101	-0.01468
1	1.59109	1.59113	0.00004	6.53614	6.52156	-0.01458
2	1.57397	1.57475	0.00078	6.5731	6.55940	-0.01370
3	1.55676	1.55747	0.00071	6.6026	6.59281	-0.00979
4	1.53945	1.54010	0.00065	6.6289	6.63691	0.00801
5	1.52205	1.52265	0.00060	6.657	6.65359	-0.00341
$B^1\Delta_g$						
v	Experiment	Theory	Difference	Experiment	Theory	Difference
0	1.45527	1.45548	0.00021	6.3259	6.37096	0.04506
1	1.43843	1.43964	0.00121	6.34196	6.30755	-0.03441
2	1.42155	1.42346	0.00191	6.3575	6.41764	0.06014
3	1.40464	1.40646	0.00182	6.3671	6.33773	-0.02937
4	1.38772	1.38928	0.00156	6.4035	6.35229	-0.05121
5	1.37074	1.37223	0.00149	6.3883	6.39922	0.01092
$B'^1\Sigma^+_g$						
v	Experiment	Theory	Difference	Experiment	Theory	Difference
0	1.47531	1.47472	-0.00059	6.781	6.39399	-0.38701
1	1.46482	1.46337	-0.00145	6.6208	6.12939	-0.49141
2	1.45614	1.45375	-0.00239	6.744	5.96153	-0.78247
3	1.44786	1.44437	-0.00349	6.881	5.79821	-1.08279

[a] Experimental values from references [11,12]

deviations, especially in terms of percent differences. The first anharmonicities for the $B^1\Delta_g$ and $B'^1\Sigma^+_g$ states from this work are somewhat less accurate than the values found in references 34 and 35.

The constants derived from the rotational energy levels (B_e, α_e, *and* D_{rot}) were only reported in three recent studies [30,34,35]. These theoretical studies, as well as this work, reproduce the experimental B_e values to a high level of accuracy for all states. Good agreement is also seen in the α_e results with the exception of the $B^1\Delta_g$ state where the results of this work differ from experiment and the results of reference 35 by 7%. D_{rot} values from this work and references 34 and 35 differ from the experiment by ~1% or less except for the $B'^1\Sigma^+_g$ state, where all theoretical results deviate by ~5%.

It is worth noting that all of the previous studies with the highest accuracies employed MRCISD calculations with basis sets up to aug-cc-pV6Z. In contrast, the present work uses only basis sets up to and including cc-pVQZ, but recovers the full correlation up to sextuple excitations by CEEIS and complete basis set extrapolations. Core-valence correction and scalar relativistic effects were included in the previous and the present studies. In general, the present theoretical work and past studies agree very well for the values of the spectroscopic constants. The deviations are on the order of a few cm^{-1}, with percent differences being notably small in most cases.

4 Conclusions

The previous CEEIS methodology for calculating diatomic ground state PECs has been extended to the simultaneous determination of ground and excited states. As was the case for the calculations on ground states, CBS extrapolated CEEIS energies, with the addition of the corrections due to core-valence correlation and relativistic effects have been shown to yield highly accurate PECs for the excited electronic states.

With this method, *ab initio* PECs of the four lowest lying singlet states ($X^1\Sigma^+_g$, $A^1\Pi_u$, $B^1\Delta_g$, and $B'^1\Sigma^+_g$) have been calculated. In contrast to previous studies that have used MRCISD with aug-cc-pV6Z basis sets, the present work has obtained the extrapolated full correlation energy up to and including sextuple excitations using up to cc-pVQZ basis sets, followed by complete basis set extrapolation. The effect of using dynamically weighted versus evenly weighted MCSCF reference functions was found to be negligible once the dynamical correlation was accounted for by the CEEIS procedure. The calculated PECs exhibit the interesting, complex structure of the low-lying singlet states of C_2, involving multiple curve crossings and the avoided crossing between the two $^1\Sigma^+_g$ states. This avoided crossing causes distortions in the shapes of the $^1\Sigma^+_g$ PECs that make it difficult to fit these curves by analytic functions.

The theoretical PECs show very good agreement with the experimental results. For all four states, equilibrium bond distances, dissociation energies, excitation energies and spectroscopic constants are obtained with high accuracy. The calculated dissociation energy of the ground state deviates from experiment by only -0.38 kcal/mol, exhibiting "chemical accuracy". After fitting the *ab initio* energies to an analytical form or to cubic splines, the nuclear Schrödinger equation was solved to obtain ro-vibrational levels and spectroscopic parameters. The previously unreported full spectra of all bound vibrational states are reported in the Supporting Information for all four electronic states. Comparisons with the available experimental data on the vibrational manifolds (which are limited to 4 to 7 levels) show MADs of ~10-20 cm^{-1} for the vibrational energy levels, or "near spectroscopic accuracy". Spectroscopic constants were obtained by expanding the vibrational and rotational energy levels in terms of powers of (v + ½) and [J(J+1)]. The calculated rotational constants (B_v and D_v) show excellent agreement with experiment. The lower order constants of the vibrational expansions also show excellent agreement with the experimental results, while the higher order terms are less accurate.

Acknowledgements

The authors thank Dr. Laimutis Bytautas and Dr. Luke Roskop for helpful discussions related to this work. This research is supported by the U.S. Department of Energy, Office of Basic Energy Sciences, Division of Chemical Sciences, Geosciences, and Biosciences through the Ames Laboratory. The Ames Laboratory is operated for the U.S. Department of Energy by Iowa State University under Contract No. DE-AC02-07CH11358.

References

1. Vardya MS (1970) Ann Rev Astron Astr 8:87-114

2. Mayer P, O'Dell CR (1968) Astrophys J 153:951-962

3. Souza SP, Lutz BL (1977) Astrophys J 216 (1):L49-L51

4. Bleekrode R, Nieuwpoort WC (1965) J Chem Phys 43 (10):3680-3687

5. Fox JG, Herzberg G (1937) Phys Rev 52 (6):0638-0643

6. Ballik EA, Ramsay DA (1959) J Chem Phys 31 (4):1128-1128

7. Ballik EA, Ramsay DA (1963) Astrophys J 137 (1):84-101

8. Marenin IR, Johnson HR (1970) J Quant Spectrosc Radiat Transfer 10 (4):305-309

9. Huber KP, Herzberg G (1979) Molecular spectra and molecular structure IV. Constants of diatomic molecules. Van Nostrand Reinhold, New York

10. Amiot C (1983) Astrophys J Suppl S 52 (3):329-340

11. Douay M, Nietmann R, Bernath PF (1988) J Mol Spectrosc 131 (2):250-260

12. Douay M, Nietmann R, Bernath PF (1988) J Mol Spectrosc 131 (2):261-271

13. Davis SP, Abrams MC, Phillips JG, Rao MLP (1988) J Opt Soc Am B: Opt Phys 5 (10):2280-2285

14. Martin M (1992) J Photochem Photobiol A 66 (3):263-289

15. Gong MX, Bao YH, Urdahl RS, Jackson WM (1994) Chem Phys Lett 217 (3):210-215

16. Wakabayashi T, Ong AL, Kratschmer W (2002) J Chem Phys 116 (14):5996-6001

17. Chan MC, Yeung SH, Wong YY, Li YF, Chan WM, Yim KH (2004) Chem Phys Lett 390 (4-6):340-346

18. Tanabashi A, Hirao T, Amano T, Bernath PF (2007) Astrophys J Suppl S 169 (2):472-484

19. Brooke JSA, Bernath PF, Schmidt TW, Bacskay GB (2013) J Quant Spectrosc Radiat Transfer 124:11-20

20. Fougere PF, Nesbet RK (1966) J Chem Phys 44 (1):285-298

21. Langhoff SR, Sink ML, Pritchard RH, Kern CW, Strickler SJ, Boyd MJ (1977) J Chem Phys 67 (3):1051-1060

22. Chabalowski CF, Peyerimhoff SD, Buenker RJ (1983) Chem Phys 81 (1-2):57-72

23. Kraemer WP, Roos BO (1987) Chem Phys 118 (3):345-355

24. Bruna PJ, Wright JS (1991) Chem Phys 157 (1-2):111-121

25. Peterson KA (1995) J Chem Phys 102 (1):262-277

26. Boggio-Pasqua M, Voronin AI, Halvick P, Rayez JC (2000) J Mol Struct (Theochem) 531:159-167

27. Muller T, Dallos M, Lischka H, Dubrovay Z, Szalay PG (2001) Theor Chem Acc 105 (3):227-243

28. Abrams ML, Sherrill CD (2004) J Chem Phys 121 (19):9211-9219

29. Sherrill CD, Piecuch P (2005) J Chem Phys 122 (12):124104

30. Kokkin DL, Bacskay GB, Schmidt TW (2007) J Chem Phys 126 (8):084302

31. Mahapatra US, Chattopadhyay S, Chaudhuri RK (2008) J Chem Phys 129 (2)

32. Varandas AJC (2008) J Chem Phys 129 (23)

33. Purwanto W, Zhang SW, Krakauer H (2009) J Chem Phys 130 (9)

34. Zhang X-N, Shi D-H, Sun J-F, Zhu Z-L (2011) Chin Phys B 20 (4)

35. Shi D, Zhang X, Sun J, Zhu Z (2011) Mol Phys 109 (11):1453-1465

36. Su PF, Wu JF, Gu JJ, Wu W, Shaik S, Hiberty PC (2011) J Chem Theory Comput 7 (1):121-130

37. Booth GH, Cleland D, Thom AJW, Alavi A (2011) J Chem Phys 135 (8)

38. Jiang W, Wilson AK (2011) J Chem Phys 134 (3)

39. Angeli C, Cimiraglia R, Pastore M (2012) Mol Phys 110 (23):2963-2968

40. Shaik S, Danovich D, Wu W, Su P, Rzepa HS, Hiberty PC (2012) Nat Chem 4 (3):195-200

41. Liu W, Hanauer M, Koehn A (2013) Chem Phys Lett 565:122-127

42. Deskevich MP, Nesbitt DJ, Werner HJ (2004) J Chem Phys 120 (16):7281-7289

43. Bytautas L, Ruedenberg K (2004) J Chem Phys 121 (22):10905-10918

44. Bytautas L, Ruedenberg K (2004) J Chem Phys 121 (22):10919-10934

45. Bytautas L, Ruedenberg K (2005) J Chem Phys 122 (15):154110

46. Bytautas L, Nagata T, Gordon MS, Ruedenberg K (2007) J Chem Phys 127 (16):164317-164317

47. Bytautas L, Ruedenberg K (2010) J Chem Phys 132 (7)

48. Bytautas L, Matsunaga N, Scuseria GE, Ruedenbereg K (2012) J Phys Chem A 116 (7):1717-1729

49. Bytautas L, Matsunaga N, Nagata T, Gordon MS, Ruedenberg K (2007) J Chem Phys 127 (20):204301-204301

50. Bytautas L, Matsunaga N, Nagata T, Gordon MS, Ruedenberg K (2007) J Chem Phys 127 (20):204313-204313

51. Bytautas L, Matsunaga N, Ruedenberg K (2010) J Chem Phys 132 (7):074307-074307

52. Schmidt MW, Baldridge KK, Boatz JA, Elbert ST, Gordon MS, Jensen JH, Koseki S, Matsunaga N, Nguyen KA, Su SJ, Windus TL, Dupuis M, Montgomery JA (1993) J Comput Chem 14 (11):1347-1363

53. Cheung LM, Sundberg KR, Ruedenberg K (1979) Int J Quantum Chem 16 (5):1103-1139

54. Ruedenberg K, Schmidt MW, Gilbert MM, Elbert ST (1982) Chem Phys 71 (1):41-49

55. Ruedenberg K, Schmidt MW, Gilbert MM (1982) Chem Phys 71 (1):51-64

56. Ruedenberg K, Schmidt MW, Gilbert MM, Elbert ST (1982) Chem Phys 71 (1):65-78

57. Roos BO, Taylor PR, Siegbahn PEM (1980) Chem Phys 48 (2):157-173

58. Dunning TH (1989) J Chem Phys 90 (2):1007-1023

59. Wilson AK, van Mourik T, Dunning TH (1996) J Mol Struct (Theochem) 388:339-349

60. Klopper W, Kutzelnigg W (1986) J Mol Struct (Theochem) 28:339-356

61. Kutzelnigg W (1994) Int J Quantum Chem 51 (6):447-463

62. Lowdin PO (1955) Phys Rev 97 (6):1474-1489

63. The multistate CEEIS method is included in all versions of GAMESS that occur after May 1, 2013

64. Helgaker T, Klopper W, Koch H, Noga J (1997) J Chem Phys 106 (23):9639-9646

65. Halkier A, Helgaker T, Jorgensen P, Klopper W, Koch H, Olsen J, Wilson AK (1998) Chem Phys Lett 286 (3-4):243-252

66. Langhoff SR, Davidson ER (1974) Int J Quantum Chem 8 (1):61-72

67. Douglas M, Kroll NM (1974) Ann Phys 82 (1):89-155

68. Fedorov DG, Nakajima T, Hirao K (2001) Chem Phys Lett 335 (3-4):183-187

69. Nakajima T, Hirao K (2005) Monatsh Chem 136 (6):965-986

70. de Jong WA, Harrison RJ, Dixon DA (2001) J Chem Phys 114 (1):48-53

71. Fedorov DG, Gordon MS (2000) J Chem Phys 112 (13):5611-5623

72. Aquilante F, De Vico L, Ferre N, Ghigo G, Malmqvist P-A, Neogrady P, Pedersen TB, Pitonak M, Reiher M, Roos BO, Serrano-Andres L, Urban M, Veryazov V, Lindh R (2010) J Comput Chem 31 (1):224-247

73. Colbert DT, Miller WH (1992) J Chem Phys 96 (3):1982-1991

74. Blatt JM (1967) J Comput Phys 1 (3):382-396

75. Zeng T, Fedorov DG, Klobukowski M (2011) J Chem Phys 134 (2)

76. Urdahl RS, Bao YH, Jackson WM (1991) Chem Phys Lett 178 (4):425-428

CHAPTER 5. CORRELATION ENERGY EXTRAPOLATION BY MANY-BODY EXPANSION

A paper published in the *Journal of Physical Chemistry A*, 2017, 121(4), 836-844

Jeffery S. Boschen, Daniel Theis, Klaus Ruedenberg, and Theresa L. Windus

Abstract

Accounting for electron correlation is required for high accuracy calculations of molecular energies. The full configuration interaction (CI) approach can fully capture the electron correlation within a given basis, but it does so at a computational expense that is impractical for all but the smallest chemical systems. In this work, a new methodology is presented to approximate configuration interaction calculations at a reduced computational expense and memory requirement, namely the correlation energy extrapolation by many-body expansion (CEEMBE). This method combines a MBE approximation of the CI energy with an extrapolated correction obtained from CI calculations using subsets of the virtual orbitals. The extrapolation approach is inspired by, and analogous to, the method of correlation energy extrapolation by intrinsic scaling. Benchmark calculations of the new method are performed on diatomic fluorine and ozone. The method consistently achieves agreement with CI calculations to within a few mhartree and often achieves agreement to within ~1 mhartree or less, while requiring significantly less computational resources.

Introduction

Full configuration interaction (CI) calculations can capture the electron correlation within a given basis set exactly, but the exponential growth of the number of configurations with the system size makes its application infeasible for all but the smallest of molecules. However, it is also known that the CI correlation energy can be recovered to high accuracy with only a small percentage of the total configurations, thus reducing the overall computational expense and memory usage. The development of methods which can exploit this fact continues to be an active area of research.[1–8]

Relevant for the present approach are the many-body expansion (MBE) and the correlation energy extrapolation by intrinsic scaling (CEEIS).[9–11] MBE methods have been widely used in computational chemistry, particularly in fragment based methods,[12–14] and the approach has also been applied to capturing electron correlation in solids by the method of increments.[15,16] The CEEIS method has been able to recover diatomic potential energy surfaces with an accuracy of a fraction of a mhartree.[17–20] In the present work, MBE techniques are combined with an extrapolation that is inspired by the CEEIS procedure to obtain a reliable estimate for the CI energy. The new approach is called the correlation energy extrapolation by many-body expansion (CEEMBE). The CEEMBE approach uses (1) an approximate decomposition of the electron correlation energy into a number of independent and less expensive subproblems (the MBE approach) and (2) an extrapolation of the correlation energy using a linear relationship between the correlation energy and number of correlated virtual orbitals between the actual CI energies and the ones from the MBE approach (related to the CEEIS approach).

To formulate the MBE approximation of the CI energy, the valence orbitals are separated into groups, or “bodies”, each with a preset number of valence electrons (a configuration subspace). A set of “reduced” CI calculations is then performed by only considering electron excitations that occur out of (and between) limited subsets of these bodies (i.e. individual 1-, 2-, and 3-body calculations), where each calculation corresponds to a different combination of bodies. The reduced CI calculations are then used in the standard many-body expansion formulas to determine the MBE approximation.

The fundamental assumption behind the MBE approximation of the CI energy is that the contributions to the total energy resulting from excitations involving several different bodies of valence orbitals can be well approximated by appropriately combining the results of separate reduced CI calculations. Unfortunately, this assumption is often not valid and gives rise to large errors in the prediction of the CI energy. To correct these errors, a procedure is developed that extrapolates the plot of the actual CI energy changes versus the energy changes that occur in the MBE approximation when the dimension of the virtual orbital space is gradually increased. The virtual orbital spaces of lower dimension are obtained by pruning the full set of virtual orbitals into which the electrons can be excited. This type of extrapolation method is analogous to the one used in the CEEIS approach. The next section gives a more complete description of each of the basic steps in the method: determination of the bodies to be used, the MBE process, and the extrapolation using limited sets of virtual orbitals to obtain the final approximate energy.

In this work the CEEMBE method will be used to approximate the following multireference (MR) CI calculations:

- MR-CISD (includes configurations with single and double excitations from the reference)
- MR-CISDT (includes up to triple excitations)

- MR-CISDTQ (includes up to quadruple excitations)

For the sake of brevity, the “MR” prefix will be dropped in the remainder of the paper.

The goal of this paper is to explain the method and show its use to predict the correlation energy at isolated points on the potential energy surface as well as to give reliable energy differences at characteristic points on the potential energy surface. As with all methods that rely on a multi-reference approach, the applicability of the method to a complete potential energy surface will rely heavily on the choice of the active space and is not the focus of this paper. The accuracy of the CEEMBE approximation of various truncated CI energies will be tested on a portion of the F_2 dissociation potential energy curve, as well as on several points of interest for the 1^1A_1 and 2^1A_1 states of ozone.

Theoretical Methods - Correlation Energy Extrapolation by Many-Body Expansion

Selecting Orbital “Bodies”

Prior to running any CEEMBE calculations, it is necessary to define the bodies of the MBE by separating the valence orbitals into groups and assigning an initial number of electrons to each group. Ideally, each valence orbital would be treated as a distinct orbital group, allowing the CI calculations to consider excitations from specific orbitals rather than small groups of orbitals. However, it is necessary to group the orbitals in a manner that generates all the dominant electron configurations of the wave function (the configurations that contribute to the static electron correlation).

As an example, consider diatomic fluorine. F_2 has eight valence orbitals ($2\sigma_g$, $2\sigma_u$, $1\pi_{u,x}$, $1\pi_{u,y}$, $1\pi_{g,x}$, $1\pi_{g,y}$, $3\sigma_g$, and $3\sigma_u$) and 14 valence electrons, but only two electron configurations, $[He_2](2\sigma_g)^2(2\sigma_u)^2(1\pi_u)^4(1\pi_g)^4(3\sigma_g)^2$ and $[He_2](2\sigma_g)^2(2\sigma_u)^2(1\pi_u)^4(1\pi_g)^4(3\sigma_u)^2$, are needed to obtain a qualitatively correct potential energy surface for the F_2 ($X\ ^1\Sigma_g^+$) → 2F ($X\ ^2P$) dissociation. Images of the canonicalized forms of the eight valence orbitals from the complete active space self-consistent field CASSCF(2,2)/cc-pVQZ[21] wave function (when R_{FF} = 1.600 Å) are shown in Figure 1.

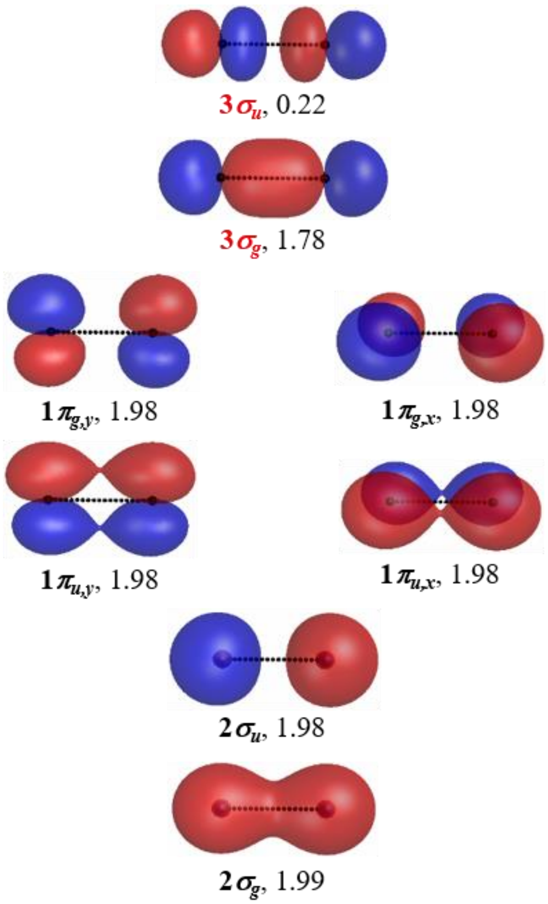

$3\sigma_u$, 0.22

$3\sigma_g$, 1.78

$1\pi_{g,y}$, 1.98
$1\pi_{g,x}$, 1.98

$1\pi_{u,y}$, 1.98
$1\pi_{u,x}$, 1.98

$2\sigma_u$, 1.98

$2\sigma_g$, 1.99

Figure 1. Canonical valence orbitals of the CASSCF(2,2)/cc-pVQZ wave function for the ground state of F_2 when R = 1.600 Å. Symmetry labels, as well as occupation numbers of the analogous natural orbitals are listed below each orbital. Red symmetry labels indicate the orbitals that must be included in the CASSCF active space to obtain a qualitatively correct potential energy surface for dissociation.

On the basis of the orbital occupations of the two dominant configurations of F_2 and to minimize the number of orbitals in each group, the valence orbitals are separated into the following seven groups: $G_1=\{2\sigma_g\}$; $G_2=\{2\sigma_u\}$; $G_3=\{1\pi_{u,x}\}$; $G_4=\{1\pi_{u,y}\}$; $G_5=\{1\pi_{g,x}\}$; $G_6=\{1\pi_{g,y}\}$; and $G_7=\{3\sigma_g,3\sigma_u\}$. The 14 valence electrons should then be distributed among the seven groups by assigning two electrons to each group.

Once the valence orbitals have been separated into groups, a series of reduced CI calculations are performed. The term "*reduced*" describes the pruning of the configuration space that occurs when excitations into the virtual orbitals only occur from a limited subset of the valence orbitals to be correlated. CI calculations that are performed on such configuration spaces are referred to as *reduced* CI calculations. The term "*exact*" is applied to *any* CI calculation that allows excitations from the full set of valence orbitals to be correlated.

Each calculation is identified by an excitation level, X, that denotes the maximum occupancy of the *virtual* orbital space (i.e., X = 2 corresponds to a CISD calculation), as well as a unique combination of indices i_1, i_2, …, i_γ that specify the orbital groups that can gain or lose electrons during the calculation (in this paper, those groups are referred to as *active* groups). The subscript γ that appears in the final index denotes the total number of active groups that contribute to the generation of the reduced active space. The energy determined for a reduced CI calculation at excitation level X is represented by the general expression $E_{i_1 i_2 \ldots i_\gamma}(X)$. For example, if two subscripts are given in the expression and X = 3, then this would represent a specific 2-body reduced CISDT calculation. From $E_{i_1 i_2 \ldots i_\gamma}(X)$, the correlation energy of the reduced active space, $\Delta E^{corr}_{i_1 i_2 \ldots i_\gamma}(X)$, is determined by subtracting $E_{i_1 i_2 \ldots i_\gamma}(X)$ by the energy of the reference space that generates the reduced active space, $E_{i_1 i_2 \ldots i_\gamma}(0)$.

The reference space corresponding to $E_{i_1 i_2 \ldots i_\gamma}(0)$ is constructed by distributing the valence electrons that were assigned to all of the active groups among the total set of orbitals that are associated with the i_1, i_2, …, i_γ active groups in a CAS manner. For example, if the valence orbitals of F_2 are grouped in the manner that was previously discussed, the expression $E_{1,7}(0)$ would denote the energy of the ground state wave function of the CAS(4,3) configuration space that is formed from the $2\sigma_g$, $3\sigma_g$, and $3\sigma_u$ orbitals and 4 valence electrons that were assigned to groups G_1 and G_7.

The configuration space needed to evaluate $E_{i_1 i_2 \ldots i_\gamma}(X)$ is generated from the reference space that determines $E_{i_1 i_2 \ldots i_\gamma}(0)$ by allowing up to X electrons to be excited from the active groups into the virtual orbital space. For F_2, the configuration space needed to evaluate $E_{1,7}(2)$, for example, is formed by expanding the CAS(4,3) space to include each unique configuration that is generated by exciting one or two electrons from orbitals $2\sigma_g$, $3\sigma_g$, and $3\sigma_u$ into the virtual orbitals.

Many-Body Expansion Approximation of the CI Energy

By treating each orbital group as a "body", many-body expansion techniques can be used to approximate the value of the correlation energy for the exact CI calculation, $\Delta E_{exact}^{corr}(X)$, from the correlation energies that are determined for the reduced CI calculations. Under the MBE approach, the approximate correlation energy is written as a sum of 1-body terms, 2-body terms, 3-body terms, *etc.*,

$$\Delta E_{nB}^{corr}(X) = \sum_{\gamma=1}^{n} \Delta E^{(\gamma)}(X) \quad (1)$$

where *n* specifies the maximum number of bodies that are considered and $\Delta E^{(\gamma)}(X)$ denotes the total γ-body contribution to the approximate correlation energy. $\Delta E^{(\gamma)}(X)$ can be decomposed into contributions from each unique combination of γ orbital groups

$$\Delta E^{(\gamma)}(X) = \sum_{i_1 i_2 \ldots i_\gamma}^{Combinations} \Delta E^{(\gamma)}_{i_1 i_2 \ldots i_\gamma}(X), \qquad (2)$$

where $\Delta E^{(\gamma)}_{i_1 i_2 \ldots i_\gamma}(X)$ denotes the contribution that the $i_1 i_2 \ldots i_\gamma$ combination of orbital groups makes to $\Delta E^{(\gamma)}(X)$. Note that in eq 2, the summation occurs over each unique combination of orbital groups. It is important to note that the correlation energy calculated for each reduced CI, $\Delta E^{corr}_{i_1 i_2 \ldots i_\gamma}(X)$, includes contributions from lower body terms that must be removed before its value can be assigned to $\Delta E^{(\gamma)}_{i_1 i_2 \ldots i_\gamma}(X)$.

For example, in F_2, the configuration space that is used to evaluate $E_{1,7}(2)$ also generates the determinants that determine $E_1(2)$ and $E_7(2)$. Before the value of $\Delta E^{corr}_{1,7}(2)$ can be assigned to $\Delta E^{(2)}_{1,7}(2)$, the 1-body energy contributions that $\Delta E_1(2)$ and $\Delta E_7(2)$ make to $\Delta E^{corr}_{1,7}(2)$ must be removed.

$$\Delta E^{(2)}_{1,7}(2) = \Delta E^{corr}_{1,7}(2) - \Delta E^{(1)}_{1}(2) - \Delta E^{(1)}_{7}(2)$$

Following the same rationale, eqs 3-5 list general expressions for $\Delta E^{(1)}_{i_1}(X)$, $\Delta E^{(2)}_{i_1 i_2}(X)$, and $\Delta E^{(3)}_{i_1 i_2 i_3}(X)$:

$$\Delta E^{(1)}_{i_1}(X) = \Delta E^{corr}_{i}(X) \qquad (3)$$

$$\Delta E^{(2)}_{i_1 i_2}(X) = \Delta E^{corr}_{i_1 i_2}(X) - \Delta E^{(1)}_{i_1}(X) - \Delta E^{(1)}_{i_2}(X) \qquad (4)$$

$$\Delta E^{(3)}_{i_1 i_2 i_3}(X) = \Delta E^{corr}_{i_1 i_2 i_3}(X) - \Delta E^{(2)}_{i_1 i_2}(X) - \Delta E^{(2)}_{i_1 i_3}(X) - \Delta E^{(2)}_{i_2 i_3}(X) \\ - \Delta E^{(1)}_{i_1}(X) - \Delta E^{(1)}_{i_2}(X) - \Delta E^{(1)}_{i_3}(X) \quad (5)$$

The following expression can be used to evaluate $\Delta E^{(\gamma)}(X)$ directly from the correlation energies and the total lower body contributions to $\Delta E^{corr}_{nB}(X)$

$$\Delta E^{(\gamma)}(X) = \sum_{i_1 i_2 \ldots i_\gamma}^{Combinations} \Delta E^{corr}_{i_1 i_2 \ldots i_\gamma}(X) - \sum_{k=1}^{\gamma-1} \binom{N_G - k}{\gamma - k} \Delta E^{(k)}(X). \quad (6)$$

where N_G is the total number of orbital groups. Applying eq 6 to F_2, the following expressions are obtained for the total 1-body, 2-body, and 3-body contributions to $\Delta E^{corr}_{nB}(X)$:

$$\Delta E^{(1)}(X) = \sum_{i_1=1}^{7} \Delta E^{corr}_{i_1}(X)$$

$$\Delta E^{(2)}(X) = \sum_{i_1=2}^{7} \sum_{i_2=1}^{i_1-1} \Delta E^{corr}_{i_1 i_2}(X) - 6 \times \Delta E^{(1)}(X)$$

$$\Delta E^{(3)}(X) = \sum_{i_1=3}^{7} \sum_{i_2=2}^{i_1-1} \sum_{i_3=1}^{i_2-1} \Delta E^{corr}_{i_1 i_2 i_3}(X) - 5 \times \Delta E^{(2)}(X) - 15 \times \Delta E^{(1)}(X)$$

It is worth noting that in cases with orbital symmetry, some of the reduced CI calculations may have the same energy and need not be duplicated. For example, in the F_2 case, $E_3(X)$ and $E_4(X)$ are equal due to the symmetry of the π_u orbitals.

Extrapolated Correction to the MBE Approximation

As will be seen in more detail in the Results section, the MBE approximation of the exact CI energy fails to achieve a consistently useful level of accuracy. To correct this error, an approximation of the exact CI energy can be made using an extrapolation technique that is analogous to the CEEIS method. The extrapolation is based on a linear relationship between the value of the exact CI energy and the value of the MBE approximation as the number of active virtual orbitals is changed. The relationship can be expressed through the following equation:

$$\Delta E_{exact}^{corr}(X\mid m) = a_X \Delta E_{nB}^{corr}(X\mid m) + b_X \qquad (7)$$

where *m* denotes the number of active virtual orbitals and $\Delta E_{exact}^{corr}(X\mid m)$ and $\Delta E_{nB}^{corr}(X\mid m)$ denote the values of the exact correlation energy and the MBE approximation of the correlation energy, respectively. The parameters a_X and b_X are determined through a linear least squares fit.

In this method, several sets of CI calculations are performed with varying numbers of active virtual orbitals, *m*. Each set includes a calculation of the exact CI energy as well as calculations of the reduced CI energies that determine $\Delta E_{nB}^{corr}(X\mid m)$, both with a limited number of active virtual orbitals.

For each value of *m*, eqs 1-6 are used to determine $\Delta E_{nB}^{corr}(X\mid m)$. A linear least-squares fit to the values for $\Delta E_{nB}^{corr}(X\mid m)$ and $\Delta E_{exact}^{corr}(X\mid m)$, for multiple *m* values, is generated to determine the slope, a_X, and intercept, b_X, of eq 7. Once a_X and b_X are known, reduced CI energies are calculated using the full set of virtual orbitals to give $\Delta E_{nB}^{corr}(X) \equiv \Delta E_{nB}^{corr}(X\mid M)$, where *M* denotes the total number of virtual orbitals that were generated by the basis set. Finally, $\Delta E_{nB}^{corr}(X)$ is used in Eq. 7 to extrapolate the *n*-body CEEMBE approximation of the exact correlation energy, $\Delta E_{CEEnB}^{corr}(X) \equiv a_X \Delta E_{nB}^{corr}(X) + b_X$. In Figure 2, we have shown an example CEEMBE extrapolation for the CISDT energy of F_2 using the cc-pVTZ basis and an up to 3-body MBE approximation. The linear relationship between $\Delta E_{nB}^{corr}(X\mid m)$ and $\Delta E_{exact}^{corr}(X\mid m)$ can be clearly seen (in this case, *X* = 3, and *nB* = *3B*). The points in the figure are obtained using virtual orbital numbers of $m = 18, 24, 30, 36, 41, 46$, and 50. The best-fit line was obtained from $m = 18$, 24, and 30. The error in the CEEMBE extrapolation is 0.578 mhartree.

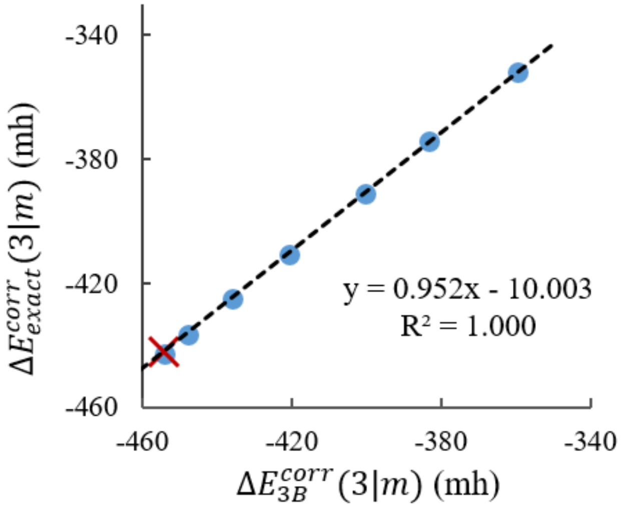

Figure 2. CEEMBE extrapolation of the CISDT correlation energy in F_2 (cc-pVTZ) using a 3-body MBE approximation. The three rightmost points are used for the best-fit line, the leftmost blue point includes the exact CISDT energy in the full virtual space. The red "X" indicates the CEEMBE extrapolated energy.

In practice, we have typically used three points for m that increase by about 5 virtual orbitals starting at a value near the number of virtual orbitals that are generated by the double zeta basis set. It is necessary to confirm that the selected range of m values exhibits the linear relationship described above. When symmetry does exist, it is important to treat each degenerate set of virtual orbitals equivalently (either they must all be included or excluded in the calculation). Because the CI calculations will be performed using incomplete subsets of the virtual orbitals, it is often beneficial to use pseudo-natural virtual orbitals. Pseudo-natural virtual orbitals are known to increase the speed of convergence for the correlation energy as the number of virtual orbitals is increased. The pseudo-natural virtual orbitals, which are used in both the reduced and exact CI calculations, are generated by diagonalizing the virtual/virtual block of the exact CISD one-particle density matrix.

In summary, the CEEMBE method requires the following steps:

1. Separate the valence orbitals into groups that will define the bodies of the MBE approximation of the CI energy. Select a range of virtual orbital subsets, m, over which to perform the linear extrapolation.
2. Perform reduced CI calculations where excitations into the virtual space come from limited subsets of the valence orbitals, for all combinations of the orbital groups which include up to n-bodies. Calculate approximate CI energies using the MBE formulas. This must be repeated for a series of calculations using a range of virtual orbital subsets, m, including calculations using the full set of virtual orbitals.
3. Perform exact CI calculations where excitations into the virtual space are allowed from all the active valence orbitals at once. This must also be repeated using a range of virtual orbital subsets, m, but NOT including the full set of virtual orbitals.
4. Plot the energies from step 2 versus the energies from step 3 at each m value and obtain a linear least squares fit to the data. Extrapolate the exact CI energy with the full set of virtual orbitals.

Note that steps 2 and 3 can be performed simultaneously. Each of the CI calculations required for the MBE and the extrapolation can be performed independently of one another and thus a CEEMBE job can be easily distributed across a number of nodes, or even separate machines, with no communication required until the simple MBE summations and linear extrapolations required at the end of the method.

Computational Methods

All calculations were performed using the occupation restricted multiple active space (ORMAS)[22] determinant CI code in the GAMESS[23] program suite. ORMAS provides the ability to specify the changing orbital spaces needed for the reduced CI calculations in the MBE approximation. Basis sets are described below in the results for each molecular system.

Results and Discussion

F_2

The first chemical system that will be considered is molecular fluorine. As discussed above, the CASSCF(2,2) reference wave function includes the two electron configurations:

$$[He_2](2\sigma_g)^2(2\sigma_u)^2(1\pi_u)^4(1\pi_g)^4(3\sigma_g)^2 \text{ and } [He_2](2\sigma_g)^2(2\sigma_u)^2(1\pi_u)^4(1\pi_g)^4(3\sigma_u)^2$$

which are needed to obtain a qualitatively correct potential energy surface for the

F_2 ($X\ ^1\Sigma_g^+$) → 2F ($X\ ^2$P) dissociation.

The dissociation channel of F_2 does not encounter any significant nonadiabatic effects, and we have chosen to examine only the ground state in these calculations. The system was studied extensively by Bytautas *et al.*[17], providing a detailed and well documented set of highly accurate CI energies for comparison. These characteristics make F_2 an ideal benchmark system for the CEEMBE method. To ensure that static correlation effects are observed, energies were evaluated for F_2 at a series of points from the experimental equilibrium bond distance (~1.412 Å) to near the inflection point of the dissociation channel (1.6 Å). All of the calculations of F_2 were performed using D_{2h} symmetry and the cc-pVQZ basis set.

A preliminary (2,2)-CASSCF/cc-pVQZ calculation was performed to optimize the occupied molecular orbitals and a preliminary CISD calculation was performed to obtain pseudo-natural orbitals for the virtual orbitals. The CI and CEEIS calculations that were performed by Bytautas *et al*. determined that the total contribution to the correlation energy that arises from the quintuple, hextuple, heptuple, and octuple excitations was less than 2 mhartree. Because these changes to the correlation energy are smaller than the target error of the CEEMBE method (~2-3 mhartree), only calculations up to the quadruple excitation level were performed.

As described above, the orbital groups that were used to perform the MBE were formed by separating the eight valence orbitals and 14 valence electrons into seven groups. The first six groups each consist of one orbital and two electrons, and the final group consists of both the $3\sigma_g$ and $3\sigma_u$ orbitals, with two electrons.

CEEMBE calculations were performed using up to 2- and 3-bodies, with active virtual subsets of m = 18, 24, 29, and M = 100 orbitals. Exact values of the CISD and CISDT energies using the full 100 virtual orbitals were obtained. The size of the exact CISDTQ calculation (run for m=M=100) exceeded the available computational resources. Instead, the CEEIS extrapolation of the CISDTQ energy that was reported in a previous study[17] was used in place of the exact CISDTQ energy for benchmarking purposes. Energies at R = 1.6 Å for the exact CI calculations (when m=100), the MBE approximations (when m=100), and the CEEMBE approximations are shown in Table 1.

Table 1. Exact and Approximate Values of the CISD, CISDT, and CISDTQ Energies for the Ground State of F_2, Calculated at $R = 1.6$ Å Using the cc-pVQZ Basis Set and the CAS(2,2) Reference[a]

	CISD, $X = 2$	CISDT, $X = 3$	CISDTQ, $X = 4$
$N_{exact}(X\|100)$	389,820	80,694,344	8,957,279,580
$\Delta E_{exact}^{corr}(X\|100)$	-468.593	-485.861	(-506.591)[b]
$\Delta E_{CEEIS}^{corr}(X\|100)$[c]	---	-488.309	-506.192
1-*Body Approximation*		*5 1-Body CI Calculations*	
$N_{1B}(X\|100)$[d]	7,172	7,172	7,172
$\Delta E_{1B}^{coor}(X\|100)$	-121.346	-121.346	-121.346
$\Delta E_{CEE1B}^{corr}(X\|100)$[e]	-440.297	-457.504	-476.263
2-*Body Approximation*		13 *Additional* 2-*Body CI Calculations*	
$N_{2B}(X\|100)$[d]	36,278	1,383,786	17,748,218
$\Delta E_{2B}^{corr}(X\|100)$[f]	-471.504	-478.136	-479.492
$\Delta E_{CEE2B}^{corr}(X\|100)$[e]	-467.822	-486.238	-506.509
3-*Body Approximation*		21 *Additional* 3-*Body CI Calculations*	
$N_{3B}(X\|100)$[d]	83,314	6,380,042	223,288,164
$\Delta E_{3B}^{corr}(X\|100)$[g]	-479.788	-499.050	-510.802
$\Delta E_{CEE3B}^{corr}(X\|100)$[e]	-468.422	-485.337	-505.957

[a] All energies are reported in mhartree. Determinant counts, N, are included for each type of calculation.

[b] A high accuracy CEEIS extrapolation from previous work[17] is used to approximate $\Delta E_{exact}^{corr}(4|100)$.

Table 1 continued

[c] The energies reported for the $\Delta E_{CEEIS}^{corr}(X|100)$ energies were determined from CEEIS extrapolations that used the same number of active virtual orbitals as were used to perform the CEEMBE extrapolations (*m* = 18, 24, and 29).

[d] $N_{1B}(X|100)$, $N_{2B}(X|100)$, and $N_{3B}(X|100)$ are the number of determinants from the most expensive 1-body, 2-body, and 3-body reduced CI calculations, respectively.

[e] The CEEMBE extrapolations were determined using 18, 24, and 29 active virtual orbitals.

[f] The values listed for $\Delta E_{2B}^{corr}(X|100)$ include the 1-body contributions that comprise the corresponding $\Delta E_{1B}^{corr}(X|100)$ energies.

[g] The values listed for $\Delta E_{3B}^{corr}(x|100)$ include the 1-body and 2-body contributions that comprise the corresponding $\Delta E_{2B}^{corr}(x|100)$ energies.

The straightforward use of the MBE approximation of the CI energy based on valence orbital groups does not yield highly accurate correlation energies. When only 1-body terms are included, the errors are several hundred mhartree, whereas including up to 2 or 3 bodies gives errors that range from ~3-30 mhartree. However, with the extrapolated correction applied to the MBE energies, the CEEMBE results compare very favorably with the exact CI correlation energies. The CEEMBE errors at all levels of excitation are less than 1 mhartree.

The energies reported in Table 1 indicate that the accuracy of the CEEMBE extrapolations for the 3-body CISD and CISDT energies are not significantly improved over the 2-body approximation. Likewise, the ΔE_{2B}^{corr} and ΔE_{3B}^{corr} energies demonstrate that the many-body expansion is not guaranteed to improve with an increase in the number of bodies included in the approximation. However, the errors for the 1-body CEEMBE extrapolations of the CISD, CISDT, and CISDTQ correlation energies clearly show that, at minimum, the 2-body approximation should be used.

Additional points along the potential energy curve of F_2 show similar quality of results. In Figure 3, the errors for the CISDT energies using the CEE2B and CEE3B approaches are shown. For these seven geometry points the error remains below 0.6 mhartree for both methods. Furthermore, the CEEMBE energies change in a smooth fashion along the curve; there are no sudden jumps in the error that would accompany rapid changes in the CEEMBE energies. Likewise, the CEEMBE CISD energies also show less than 1 mhartree error at these geometry points, and the absolute difference between the CEEIS and CEEMBE approximate CISDTQ energies is within 0.4 mhartree (See the Supporting Information for more detail).

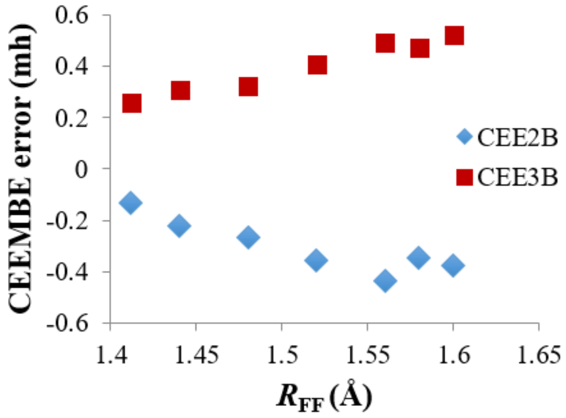

Figure 3. CEEMBE errors (in mhartree) compared to the exact CISDT energy along the F_2 (cc-pVQZ) potential energy curve.

The difference between the dimension of the CI space for the exact CI calculations and the dimension of the CI space for the largest reduced CI calculations (Table 1) indicates that, compared to the exact CI calculation, the CEEMBE method substantially reduces the memory and time required to accurately predict the correlation energy. A comparison of the CEEMBE and CEEIS extrapolations of the CISDT and CISDTQ correlation energies reveals that both methods have advantages and disadvantages. Overall, the CEEMBE method demands more work due to the large number of reduced CISDTQ calculations that need to be performed. However, unlike the CEEIS extrapolation, it is not necessary to perform separate CISDT calculations to extrapolate the CISDTQ energy. For each value of m that was considered, including m=100, the number of determinants required to determine the exact CISDT energies for the CEEIS extrapolation was larger than the number of determinants that were needed to perform the largest reduced CISDTQ calculations for the 2-body CEEMBE extrapolation, therefore, requiring more memory.

The correlation between $\Delta E_{exact}^{corr}(X|m)$ and $\Delta E_{nB}^{corr}(X|m)$ is stronger than the correlation between $\Delta E_{exact}^{corr}(X|m)$ and $\Delta E_{exact}^{corr}(X-2|m)$ (the basis of the CEEIS extrapolations), allowing the CEEMBE extrapolation to be performed using fewer active virtual orbitals (*i.e.* smaller values of m). This is particularly pronounced in the extrapolation of the CISDT energy. Using the CISD and CISDT energies that were evaluated when m was 18, 24, and 29, CEEMBE and CEEIS extrapolations were performed for the CISDT energy (Table 1). The CEEMBE and CEEIS energies indicate that the accuracy of the CEEMBE extrapolation is almost an order of magnitude higher than the accuracy of the CEEIS extrapolation. This behavior is seen at each point along the potential energy curve; the CEEIS errors for the CISDT energies with the same m values range from ~1.4-2.6 mhartree.

O_3

The final molecule that will be considered is ozone. Unlike F_2, ozone has a very complex multiconfigurational electronic structure. Its electronic states also experience significant amounts of nonadiabatic coupling, and O_3 was one of the earliest systems used to demonstrate the existence of a conical intersection.[24–28] Theoretical calculations have shown the existence of two stable ground state minima,[29–32] but the closed ring minimum has never been observed experimentally.

The ozone test case also provides an example of the CEEMBE method applied to an excited electronic state.

The calculations reported in this paper will focus on the 1 $^1A_1$ and 2 $^1A_1$ energies at the following geometries:

OM – the 1^1A_1 open minimum

RM – the 1^1A_1 ring minimum

TS – transition state between the OM and the RM on the 1^1A_1 surface

ESM – the minimum of the 2^1A_1 state

CX – the conical intersection between the 1^1A_1 and 2^1A_1 states

The geometries used in this study were obtained in a previous study[33] from optimizations using state-averaged CASSCF(18,12)/cc-pVQZ calculations involving the two lowest $^1A_1$ states of O_3.

The reference spaces and CI expansions used for O_3 will also follow those defined in the previous work. In Figure 4 the full set of valence orbitals from a state-averaged CASSCF(18,12) calculation are given. The CEEMBE method was tested on two reference spaces: one obtained from a CASSCF(6,4) calculation with $6a_1$, $1a_2$, $4b_1$, and $2b_2$ as active orbitals, and one from a CASSCF(2,2) calculation with $4b_1$, and $2b_2$ as active orbitals. In all calculations reported, the $5b_1$ and $7a_1$ orbitals were placed in the virtual space. When performing CI expansions of these reference spaces, excitations may or may not be allowed from the full set of valence orbitals shown in Figure 4. A "*" label next to the reference active space (i.e. (2,2)*) indicates that excitations from the $3a_1$, $4a_1$, and $2b_1$ orbitals that involve mostly oxygen 2s atomic orbitals were *not* included.

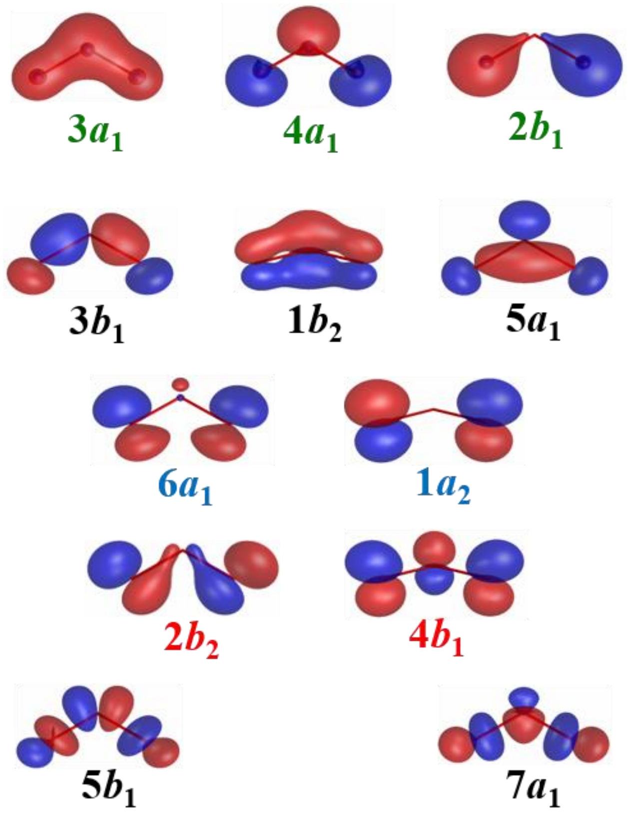

Figure 4. Canonicalized valence orbitals of the state-averaged CASSCF(18,12)/cc-pVTZ wave functions for the 1 $^1A_1$ and 2 $^1A_1$ states of O_3 at the OM. Below each orbital, the symmetry label (in C_{2v}) is given. Orbitals with green symmetry labels are not correlated in "*" excitation schemes. Blue and red symmetry labels indicate the (6,4) active space. Red labels indicate the (2,2) active space.

The orbitals groups for the MBE approximations of ozone were defined similarly to the F_2 case. In each CEEMBE calculation, the valence orbitals not in the CASSCF reference active space were each assigned to a separate group of one orbital, whereas the active orbitals from the CASSCF calculation were assigned to an orbital group together. For example, the (2,2)* MBE approximation makes use of the following six bodies: {$5a_1$}, {$3b_1$}, {$1b_2$}, {$6a_1$}, {$1a_2$}, {$4b_1$, $2b_2$}. As before, the virtual orbitals are pseudonatural orbitals from an exact CISD calculation. The *m* values used in the calculations with subsets of the virtual orbitals were: 30, 35, and 40 for the schemes with a (2,2) reference (both with “*” and without) whereas 30, 36, and 40 were used with the (6,4) reference. The total number of virtual orbitals is 77 in the cc-pVTZ basis.

The errors for the CEEMBE method relative to the exact values are reported in Tables 2 and 3 for the (2,2)* and (6,4)* schemes, respectively. As with F_2, the errors are in general quite small and less than 1 mhartree on average, even for the excited state. However, for some geometries and active spaces the errors may be as large as ~2 mhartree. The largest errors are usually at the conical intersection for the (2,2)* scheme. The CEEMBE relative energies between the different structures also differ by no more than ~1 mhartree compared to the exact values, again with the exception of the conical intersection. The reported CISDTQ “errors” are simply the energy differences between the CEEMBE and CEEIS methods. The two extrapolations are typically in agreement to within ~1 mhartree or less. On the basis of this small number of data points, there does not appear to be a consistent increase in accuracy by including 3-body contributions in the CEEMBE calculation. Though this would require further testing, it may be possible to achieve sufficient accuracy while only including up to 2-body calculations.

Comparing the results for the two active spaces shows that the (6,4)* CEEMBE calculations have a noticeably smaller error overall – usually less than 0.5 mhartree. This result is not surprising given that the number of orbital groups in the (6,4)* scheme is smaller than in the (2,2)*, with four and six bodies respectively. This leads to the MBE approximation being more accurate in the (6,4)* scheme and presumably easier to correct with the extrapolations. Another point of interest is a comparison of the TS and ESM geometries. These two geometries are only slightly different (0.02° difference in O-O-O angle), and as was seen in the F_2 curve, the CEEMBE errors appear to change smoothly with small geometrical changes.

Table 2. Energy Differences (in mhartrees) between CEEMBE and Exact CI calculations on O_3 with the (2,2)* Reference Space

		geometry				
		OM	TS	ESM	CX	RM
1^1A_1						
CISD	CEE2B	0.242	0.751	0.763	1.286	0.783
	CEE3B	0.004	-0.752	-0.766	-2.405	0.050
CISDT	CEE2B	-0.065	0.237	0.262	0.837	0.371
	CEE3B	0.106	-0.276	-0.285	-1.692	0.216
CISDTQ[a]	CEE2B	(0.029)	(0.418)	(0.433)	(1.102)	(0.469)
	CEE3B	(0.178)	(-0.166)	(-0.187)	(-1.481)	(0.306)
2^1A_1						
CISD	CEE2B	1.164	0.071	0.065	0.790	
	CEE3B	1.431	0.246	0.264	1.686	
CISDT	CEE2B	-0.134	-0.729	-0.750	-0.084	
	CEE3B	1.062	0.186	0.199	1.727	
CISDTQ[a]	CEE2B	(0.165)	(-0.555)	(-0.532)	(0.353)	
	CEE3B	(1.438)	(0.360)	(0.418)	(2.186)	

[a] CISDTQ values are differences between CEEMBE and CEEIS calculations and are denoted with parentheses.

Table 3. Energy Differences (in mhartrees) between CEEMBE and Exact CI calculations on O_3 with the (6,4)* Reference Space

		geometry				
		OM	TS	ESM	CX	RM
1^1A_1						
CISD	CEE2B	0.253	0.038	0.036	0.360	-0.010
	CEE3B	0.025	-0.021	-0.020	-0.054	0.030
CISDT	CEE2B	0.435	-0.122	-0.130	0.147	-0.018
	CEE3B	0.096	0.005	0.003	0.008	0.028
CISDTQ[a]	CEE2B	(0.437)	(0.000)	(-0.011)	(0.316)	(0.119)
2^1A_1						
CISD	CEE2B	-0.015	0.145	0.144	0.406	
	CEE3B	0.072	0.275	0.276	0.314	
CISDT	CEE2B	-0.223	-0.511	-0.506	-0.214	
	CEE3B	0.136	0.118	0.120	0.174	
CISDTQ[a]	CEE2B	(-0.356)	(-0.296)	(-0.293)	(0.027)	

[a] CISDTQ values are differences between CEEMBE and CEEIS calculations and are denoted with parentheses.

We encountered an issue obtaining CEEMBE energies for the 2^1A_1 excited state at the ring minimum. For some of the reduced CI calculations, consistent 2^1A_1 states were not found as the number of virtual orbitals was varied. Specifically, the calculations with small *m* values did not include the correct 2^1A_1 state present in the calculation with the full set of virtual orbitals. More work is needed to determine the prevalence and severity of this issue and its impact on the method's application to excited states. No 2^1A_1 values are reported at the RM for this reason.

Calculations at the OM geometry using CI expansions which included excitations from the $3a_1$, $4a_1$, and $2b_1$ orbitals were also performed. The errors in the CEEMBE method for those schemes are reported in Table 4. The additional orbitals lead to the (2,2) CEEMBE calculations requiring nine bodies whereas the (6,4) calculations require seven bodies. The increasing number of orbital groups unsurprisingly leads to decreasing accuracy for the CEEMBE method, though the errors are still usually less than 3 mhartree. As before, the (6,4) reference space, which requires a smaller number of orbital groups for the MBE, shows better accuracy. In the case of the (2,2) space, the 3-body contributions usually lower the error significantly, suggesting that the 3-body contributions become important as the number of bodies increases. The 3-body contributions also decrease the error in the (6,4) scheme for the ground state but slightly increase the error for the excited state (all the excited state errors are still less than 1 mhartree).

The number of determinants required for the CI calculations in the CEEMBE method is much smaller than what would be required for the exact calculations in the full virtual space, reducing the amount of memory needed for the calculation. In Table 5, values are given for the number of determinants in the most expensive CI calculation required for the MBE approximation as a percentage of the number of determinants in the exact CI calculation in the full virtual space. We also report the same number for the most expensive exact CI calculation, using a subset of the virtual orbitals, required to perform the linear extrapolation (Extrapolation in the Table), and the total number of determinants for the exact CI calculation. The "Extrapolation" value is the same for CEEMBE and CEEIS calculations using the same *m* values. In most cases, the more expensive step is the same for both the CEEIS and the CEEMBE methods.

Table 4. Energy Differences (in mhartress) between CEEMBE and Exact CI calculations with the (2,2) and (6,4) Schemes at the OM Geometry.

		(2,2)	(6,4)
1^1A_1			
CISD	CEE2B	2.957	1.726
	CEE3B	-0.920	0.915
CISDT	CEE2B	3.445	1.871
	CEE3B	0.243	0.996
CISDTQ[a]	CEE2B	(3.931)	
	CEE3B	(0.223)	
2^1A_1			
CISD	CEE2B	2.842	0.375
	CEE3B	2.019	0.922
CISDT	CEE2B	3.520	0.327
	CEE3B	3.629	0.934
CISDTQ[a]	CEE2B	(4.132)	
	CEE3B	(3.936)	

[a] CISDTQ values are differences between CEEMBE and CEEIS calculations and are denoted with parentheses.

Table 5. Percentage of Determinants in the Most Expensive CI Calculations for Each Approximate Method Relative to an Exact CI Calculation, the Number of Determinants for the Largest Exact CI Calculation Used in the Extrapolation, as Well as the Total Number of Determinants that Would Be Required for the Exact CI Calculation (bold, in thousands).

		CISD	CISDT	CISDTQ
(2,2)	2-body (%)	4.8	0.7	0.1
	3-body (%)	11.6	3.3	0.8
	extrapolation (%)	27.2	14.0	7.2
	total determinants	**798**	**175,465**	**20,854,292**
(2,2)*	2-body (%)	12.0	2.9	0.4
	3-body (%)	28.9	13.5	5.4
	extrapolation (%)	27.2	14.1	7.3
	total determinants	**323**	**42,572**	**2,918,346**
(6,4)	2-body (%)	8.8	2.6	
	3-body (%)	20.1	7.9	
	extrapolation (%)	27.0	13.9	
	total determinants	**2,545**	**477,002**	
(6,4)*	2-body (%)	26.8	14.3	7.7
	3-body (%)	61.4	43.4	32.4
	extrapolation (%)	27.0	14.0	7.2
	total determinants	**835**	**86,598**	**4,796,535**

When using the (6,4)* scheme for O_3, the CEE3B calculation will require more computational effort than a CEEIS style extrapolation. As the (6,4)* scheme only uses four orbital groups in total, an up to 3-body MBE includes calculations which only lack 1 body from the exact calculation, resulting in smaller savings. However, it is useful to note that the present results show that the 3-body MBE does not provide significantly better results than a 2-body MBE and is at a much higher cost.

Estimating the cost savings of the CEEMBE method is not straightforward since it will depend on the number of bodies (and, therefore, the number of reduced calculations), the cost of each of the reduced calculations due to the varying number of determinants and the overall expense of the exact CI calculations with varying *m* values. One of the advantages of the CEEMBE method is that the many reduced and exact CI calculations can be run independently and in parallel on different machines and with different numbers of processors. During this study, we took advantage of this to accelerate the overall computations and, therefore, do not have consistent timings to show across all of the computations. However, by converting the timings to processor hours and by using the clock speed between different platforms to estimate the cost difference between platforms, we can make some initial comments on the computational cost (mostly based on the F_2 costs). For CISD calculations, the exact CI is usually less time consuming than the CEEMBE approach if the memory is available. The CEEIS method is generally less expensive (by about 1 orders of magnitude) than the CEE2B method for CISDT, with the caveat that that the accuracy is lower for the CEEIS method with the values of *m* used in this study. For CISDT, the 2-body expense is much lower overall than the exact (over an order of magnitude based on the F_2 timings), while the 3-body expense approaches that of the exact CI. As noted before, though, the 3-body expansion does not seem necessary for the cases studied. For CISDTQ, the CEE2B expense is very similar to that of the CEEIS method and both of these are much lower than the 3-body expense (which is approximately 1.3 orders of magnitude more expensive than the 2-body expense). The exact CISDTQ expense is not known since memory resources for this size of calculation were not available. Of course, different active spaces, choice of the decomposition of the active space into bodies, and size of the basis set will all play different roles in the expense of the computations. So, different chemical systems will have varying costs associated with each method. However, in cases where the memory of the compute resource is an issue, the CEEMBE method seems to be a viable method. In particular, the 2-body expansion appears to be an appropriate choice for CISDT and CISDTQ calculations.

Conclusions

The correlation energy extrapolation by many-body expansion is a new approach for approximating CI energies which, like the CEEIS method, exploits linear relationships between calculations performed in subsets of the virtual orbital space. One advantage the CEEMBE method offers over the CEEIS method is the ability to approximate lower levels of excitation more easily. The CISD energies cannot be extrapolated using CEEIS, whereas the CEEIS CISDT extrapolations are often of a lower quality than extrapolations of quadruples and higher contributions.

These two methods also suggest that there may be other useful approaches that make use of similar linear extrapolations. The general scheme pairs a lower accuracy (but affordable) calculation with a higher accuracy calculation: MBE vs exact CI for CEEMBE, lower vs higher CI excitation level for CEEIS. Once the linear relationship has been determined by a series of calculations using subsets of the virtual orbitals, the lower accuracy calculation can be corrected to give good agreement with the higher accuracy calculation. There may be other useful pairs of calculations to apply such a scheme too.

Application of the CEEMBE method to the F_2 potential energy curve has shown errors of less than 1 mhartree using MBEs of up to 2- or 3-bodies, good agreement with the previously established CEEIS method for CISDTQ energies, as well as a smooth change in the energies along the dissociation curve. For O_3, the errors for the absolute energies and the relative energies between structures show a greater range that depends on the reference active space and excitation scheme but are still within ~2-3 mhartree in almost all cases. The method is applicable to excited states, but some complications may arise. In both systems, the method provides high accuracy CI energies at a fraction of the computational resources needed for exact calculations.

Acknowledgements

This work was supported by the US Department of Energy, Office of Basic Energy Sciences, Division of Chemical Sciences, Geosciences & Biosciences through the Ames Laboratory at Iowa State University under Contract No. DE-AC02-07CH11358. The work was partially supported by compute time and software management provided by the Research IT team at Iowa State University, utilizing HPC@ISU equipment, some of which has been purchased through funding provided by NSF under MRI grant number CNS 1229081 and CRI grant number 1205413.

References

(1) Bytautas, L.; Ruedenberg, K. A Priori Identification of Configurational Deadwood. *Chem. Phys.* **2009**, *356* (1–3), 64–75.

(2) Booth, G. H.; Thom, A. J. W.; Alavi, A. Fermion Monte Carlo without Fixed Nodes: A Game of Life, Death, and Annihilation in Slater Determinant Space. *J. Chem. Phys.* **2009**, *131* (5), 54106.

(3) Tubman, N. M.; Lee, J.; Takeshita, T. Y.; Head-Gordon, M.; Whaley, K. B. A Deterministic Alternative to the Full Configuration Interaction Quantum Monte Carlo Method. *J. Chem. Phys.* **2016**, *145* (4), 44112.

(4) Schriber, J. B.; Evangelista, F. A. Communication: An Adaptive Configuration Interaction Approach for Strongly Correlated Electrons with Tunable Accuracy. *J. Chem. Phys.* **2016**, *144* (16), 161106.

(5) Knowles, P. J. Compressive Sampling in Configuration Interaction Wavefunctions. *Mol. Phys.* **2015**, *113* (13–14), 1655–1660.

(6) Bytautas, L.; Scuseria, G. E.; Ruedenberg, K. Seniority Number Description of Potential Energy Surfaces: Symmetric Dissociation of Water, N_2, C_2, and Be_2. *J. Chem. Phys.* **2015**, *143* (9), 94105.

(7) Liu, W.; Hoffmann, M. R. iCI: Iterative CI toward Full CI. *J. Chem. Theory Comput.* **2016**, *12* (3), 1169–1178.

(8) Giner, E.; Scemama, A.; Caffarel, M. Fixed-Node Diffusion Monte Carlo Potential Energy Curve of the Fluorine Molecule F2 Using Selected Configuration Interaction Trial Wavefunctions. *J. Chem. Phys.* **2015**, *142* (4), 44115.

(9) Bytautas, L.; Ruedenberg, K. Correlation Energy Extrapolation by Intrinsic Scaling. I. Method and Application to the Neon Atom. *J. Chem. Phys.* **2004**, *121* (22), 10905–10918.

(10) Bytautas, L.; Ruedenberg, K. Correlation Energy Extrapolation by Intrinsic Scaling. II. The Water and the Nitrogen Molecule. *J. Chem. Phys.* **2004**, *121* (22), 10919–10934.

(11) Bytautas, L.; Ruedenberg, K. Correlation Energy Extrapolation by Intrinsic Scaling. IV. Accurate Binding Energies of the Homonuclear Diatomic Molecules Carbon, Nitrogen, Oxygen, and Fluorine. *J. Chem. Phys.* **2005**, *122* (15), 154110.

(12) Gordon, M. S.; Fedorov, D. G.; Pruitt, S. R.; Slipchenko, L. V. Fragmentation Methods: A Route to Accurate Calculations on Large Systems. *Chem. Rev.* **2012**, *112* (1), 632–672.

(13) Richard, R. M.; Lao, K. U.; Herbert, J. M. Aiming for Benchmark Accuracy with the Many-Body Expansion. *Acc. Chem. Res.* **2014**, *47* (9), 2828–2836.

(14) Collins, M. A.; Bettens, R. P. A. Energy-Based Molecular Fragmentation Methods. *Chem. Rev.* **2015**, *115* (12), 5607–5642.

(15) Stoll, H. Correlation Energy of Diamond. *Phys. Rev. B* **1992**, *46* (11), 6700–6704.

(16) Paulus, B. The Method of Increments—a Wavefunction-Based Ab Initio Correlation Method for Solids. *Phys. Rep.* **2006**, *428* (1), 1–52.

(17) Bytautas, L.; Nagata, T.; Gordon, M. S.; Ruedenberg, K. Accurate Ab Initio Potential Energy Curve of F_2. I. Nonrelativistic Full Valence Configuration Interaction Energies Using the Correlation Energy Extrapolation by Intrinsic Scaling Method. *J. Chem. Phys.* **2007**, *127* (16), 164317.

(18) Bytautas, L.; Ruedenberg, K. Accurate Ab Initio Potential Energy Curve of O_2. I. Nonrelativistic Full Configuration Interaction Valence Correlation by the Correlation Energy Extrapolation by Intrinsic Scaling Method. *J. Chem. Phys.* **2010**, *132* (7), 74109.

(19) Bytautas, L.; Matsunaga, N.; Scuseria, G. E.; Ruedenberg, K. Accurate Potential Energy Curve for B_2. Ab Initio Elucidation of the Experimentally Elusive Ground State Rotation-Vibration Spectrum. *J. Phys. Chem. A* **2012**, *116* (7), 1717–1729.

(20) Boschen, J. S.; Theis, D.; Ruedenberg, K.; Windus, T. L. Accurate Ab Initio Potential Energy Curves and Spectroscopic Properties of the Four Lowest Singlet States of C_2. *Theor. Chem. Acc.* **2013**, *133* (2), 1425.

(21) Dunning Jr., T. H. Gaussian Basis Sets for Use in Correlated Molecular Calculations. I. The Atoms Boron through Neon and Hydrogen. *J. Chem. Phys.* **1989**, *90* (2), 1007–1023.

(22) Ivanic, J. Direct Configuration Interaction and Multiconfigurational Self-Consistent-Field Method for Multiple Active Spaces with Variable Occupations. I. Method. *J. Chem. Phys.* **2003**, *119* (18), 9364–9376.

(23) Schmidt, M. W.; Baldridge, K. K.; Boatz, J. A.; Elbert, S. T.; Gordon, M. S.; Jensen, J. H.; Koseki, S.; Matsunaga, N.; Nguyen, K. A.; Su, S.; et al. General Atomic and Molecular Electronic Structure System. *J. Comput. Chem.* **1993**, *14* (11), 1347–1363.

(24) Xantheas, S.; Elbert, S. T.; Ruedenberg, K. An Intersection Seam between the Ground State of Ozone and an Excited State of like Symmetrya). *J. Chem. Phys.* **1990**, *93* (10), 7519–7521.

(25) Xantheas, S. S.; Atchity, G. J.; Elbert, S. T.; Ruedenberg, K. Potential Energy Surfaces of Ozone. I. *J. Chem. Phys.* **1991**, *94* (12), 8054–8069.

(26) Atchity, G. J.; Ruedenberg, K. Strong Shifts in Diabatic Nondynamic Electron Correlations Cause Conical Intersection between Low-lying Closed-shell Adiabatic Singlets of like Symmetry in Ozone. *J. Chem. Phys.* **1993**, *99* (5), 3790–3798.

(27) Atchity, G. J.; Ruedenberg, K. Global Potential Energy Surfaces for the Lowest Two 1A′ States of Ozone. *Theor. Chem. Acc. 96* (3), 176–194.

(28) Atchity, G. J.; Ruedenberg, K.; Nanayakkara, A. The Intersection Seam between the 11A′ and 21A′ States of Ozone. *Theor. Chem. Acc. 96* (3), 195–204.

(29) Hay, P. J.; Goodard, W. A. Theoretical Results for the Excited States of Ozone. *Chem. Phys. Lett.* **1972**, *14* (1), 46–48.

(30) Hay, P. J.; Dunning, T. H.; Goddard, W. A. Theoretical Evidence for Bound Electronic Excited States of Ozone. *Chem. Phys. Lett.* **1973**, *23* (4), 457–462.

(31) Wright, J. S. Theoretical Evidence for a Stable Form of Cyclic Ozone, and Its Chemical Consequences. *Can. J. Chem.* **1973**, *51* (1), 139–146.

(32) Shih, S.; Buenker, R. J.; Peyerimhoff, S. D. Theoretical Investigation of the Cyclic Conformer of Ozone. *Chem. Phys. Lett.* **1974**, *28* (4), 463–470.

(33) Theis, D.; Ivanic, J.; Windus, T. L.; Ruedenberg, K. The Transition from the Open Minimum to the Ring Minimum on the Ground State and on the Lowest Excited State of like Symmetry in Ozone: A Configuration Interaction Study. *J. Chem. Phys.* **2016**, *144* (10), 104304.

CHAPTER 6. A HYBRID CORRELATION ENERGY EXTRAPOLATION APPROACH

Jeffery S. Boschen, Theresa L. Windus

Abstract

The correlation energy extrapolation by many-body expansion (CEEMBE) method is a recently introduced procedure for approximating configuration interaction (CI) energies. The method is based on a MBE of the CI energy which is corrected by a linear extrapolation inspired by the correlation energy extrapolation by intrinsic scaling (CEEIS) method. In this work, a hybrid of CEEMBE and CEEIS is presented: CEEMBE-*h*. The new method closely follows the CEEMBE procedure, but makes use of CEEIS style extrapolations to reduce the overall computational cost. In benchmark calculations on ozone and diatomic fluorine, CEEMBE and CEEMBE-*h* energies are found to agree within a small margin of 0.1-0.5 millihartree or less. The full dissociation curve of F_2 is examined to further evaluate the accuracy of the CEEMBE method. The results indicate that sub-millihartree accuracy is possible, but errors on the order of a few millihartree also occur.

1. Introduction

Methods which approximate or otherwise attempt to capture the full configuration interaction (FCI) energy are an active area of research in quantum chemistry[1–9]. The FCI method gives the exact solution to the Schrödinger equation within a basis set. FCI fully recovers the electron correlation energy within a specified basis and represents the highest accuracy possible for an electronic structure method. Unfortunately, FCI is prohibitively expensive – scaling exponentially with the size of the basis. Practical attempts to achieve FCI accuracy rely on the fact that the correlation energy can be obtained with only a small percentage of the total configurations required for the FCI[1].

In a recent work[10], the correlation energy extrapolation by many-body expansion (CEEMBE) method was introduced as a new approach for approximating high level configuration interaction (CI) energies. CEEMBE is closely related to the correlation energy extrapolation by intrinsic scaling (CEEIS) method[11–13]. Previously the CEEMBE method has been shown to approximate CISD, CISDT and CISDTQ energies to within ~1-2 millihartree accuracy or better in calculations on several points of the ozone and diatomic fluorine potential energy surfaces. The CEEMBE method is based partly on an approximation of CI energies using a many-body expansion in terms of orbital groups. MBE techniques have been applied to calculating electron correlation in a number of works[9,14–17]. Both CEEIS and CEEMBE are based on linear extrapolations using small subsets of the virtual orbitals.

In this work, a hybrid method which incorporates CEEIS extrapolations into the CEEMBE methodology is described and evaluated. The hybrid method, denoted CEEMBE-*h*, closely mimics the CEEMBE method, but with a reduction in the computational cost due to including the CEEIS extrapolations. The method will be evaluated using the same systems as the previous CEEMBE work: ozone and F_2. Comparisons between the new CEEMBE-*h* and previous CEEMBE results will be provided at points of interest for the two systems, and an extended evaluation of the F_2 potential energy curve with both approaches is included.

2. Theoretical Methods

The CEEIS and CEEMBE methods are closely related approaches for approximating CI energies. Both CEEIS and CEEMBE approximate the target CI energy by performing a linear extrapolation from a series of CI calculations which use limited subsets of the virtual orbitals. A brief description of both the CEEIS and CEEMBE methods will be given, and then the new hybrid approach will be introduced. The methods can be applied to single- or multi-reference wavefunctions.

CEEIS

Developed by Ruedenberg and coworkers, the CEEIS method has been described in detail in a number of papers, and has been used to obtain accurate potential energy curves for a number of diatomics[18–21], as well as a study of ozone[22]. The full CI energy can be decomposed into a series of energy changes from increasing levels of excitation:

$$E_{Full\ CI} = E_{Reference} + \Delta E(1) + \Delta E(2) + \Delta E(3) + \Delta E(4) \cdots \tag{1}$$

where $E_{Reference}$ is the energy of the reference wavefunction, and each $\Delta E(X)$ is the energy change from increasing the allowed excitations into the virtual orbitals from $X-1$ to X, i.e. $\Delta E(4)$ is the energy difference between a CI calculation including single, double, triple, and quadruple electron excitations (CISDTQ) and a CI calculation including up to triple excitations (CISDT). The CEEIS method exploits a linear relationship between truncated CI energies of differing excitation levels.

By varying the number of virtual orbitals, *m*, included in a CI calculation, it was observed that a linear relationship exists between $\Delta E(X)$ and $\Delta E(X-2)$:

$$\Delta E(X) = a_X \Delta E(X-2) + b_X \tag{2}$$

This relationship holds even if the number of virtual orbitals included in the CI calculation is greatly reduced (down to a certain limit – usually the size of the virtual space for a double zeta basis set). The values of a_X and b_X can be determined from a linear least-squares fit to a series of CI calculations that give $\Delta E(X)$ and $\Delta E(X-2)$ for a range of virtual orbitals, *m*. Then $\Delta E(X-2)$ is calculated when *m* includes the full set of virtual orbitals. Finally, these values are used in eq. 2 to extrapolate $\Delta E(X)$ in the full set of virtual orbitals.

In practice, $\Delta E(2)$ is computed as $\Delta E(1,2)$, i.e. CISD energy minus the reference energy, due to the negligible (or nonexistent) energy contribution from only single excitations. As a special case, it is also possible to extrapolate $\Delta E(3)$ using $\Delta E(1,2)$, but this approach requires including larger values of *m* and usually produces lower quality results.

CEEMBE

Introduced in a recent work[10], the CEEMBE method is inspired by the CEEIS approach. In the CEEMBE method, the linear relationship exploited is between an MBE based approximation of the CI energy and the CI energy:

$$E(X) = a_X E_{MBE}(X) + b_X \tag{3}$$

where $E(X)$ is now the CI energy with up to X excitations included, rather than the energy change, $\Delta E(X)$, used in the CEEIS method. $E_{MBE}(X)$ is an approximation of $E(X)$ based on a many-body expansion. As before, a series of CI calculations are performed using a range of virtual orbital counts, *m*, to obtain a_X and b_X, and a linear extrapolation is used to determine $E(X)$ in the full set of virtual orbitals.

The calculation of the approximate CI energies, $E_{MBE}(X)$, requires partitioning the active valence orbitals to be correlated into orbital groups or “bodies”. Each body is defined by the orbitals it includes as well as a number of electrons. When performing multi-reference calculations, it is important that selection of the bodies captures the static correlation. Consider the example of F_2 using a CASSCF(2,2) reference wavefunction. The $3\sigma_g$ and $3\sigma_u$ orbitals which describe the (2,2) CAS must be included in one body (with two electrons). Orbitals which are doubly occupied in the reference function can be grouped into single orbital bodies with two electrons. Following this scheme, the valence space for F_2 is divided into seven orbital groups, as shown in Figure 1.

$E_{MBE}(X)$ is given by a sum of up to *n*-body contributions:

$$E_{MBE}(X) = E_{nB}(X) = \sum_{i=1}^{n} \Delta E_i(X) \tag{4}$$

where ΔE_i is the contribution from including *i*-body contributions to the MBE. We have found that *n* must be at least two to obtain high quality results, and that (in the applications so far) $n = 2$ is sufficient for high accuracy. The $\Delta E_i(X)$ are calculated by performing “reduced” CI calculations where excitations into the virtual orbitals only come from a small number of active valence orbitals. A reduced CI calculation is required for each combination of *i* orbital groups from the total set of bodies. For $i > 1$, the values of $\Delta E_i(X)$ must account for the double counting of lower terms. Details of the MBE as applied in this context can be found in our previous work[10], or more general information on the MBE in a number of other references[23–25]. A CEEMBE calculation which includes contributions from up to *n* bodies is denoted by CEE*n*B.

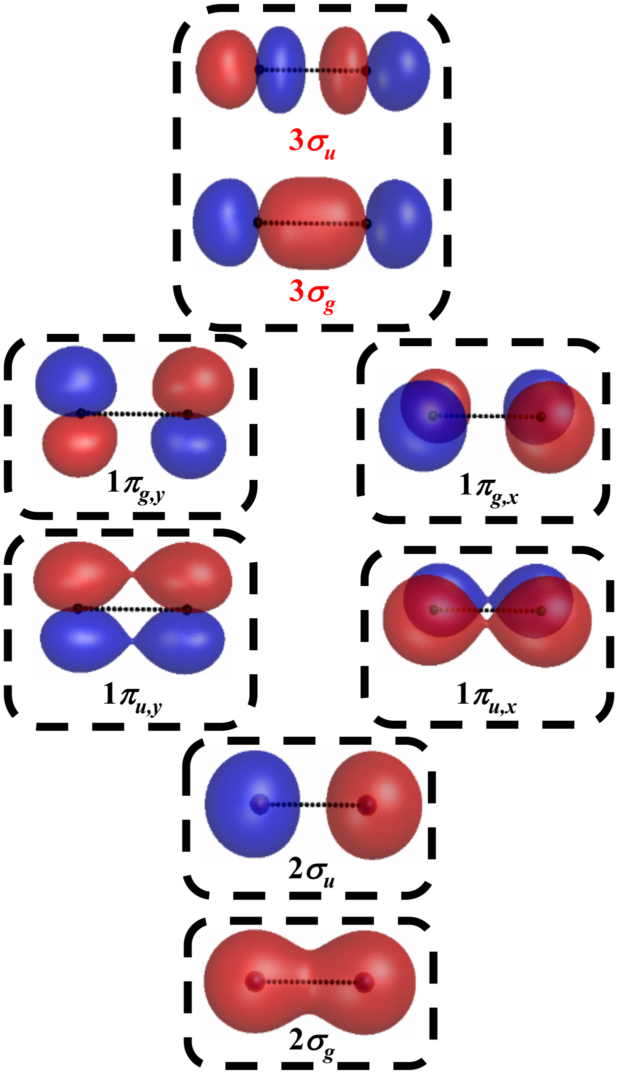

Figure 1. Canonical valence orbitals of the CASSCF(2,2)/cc-pVQZ wave function for the ground state of F_2 when R = 1.600 Å. Dashed boxes indicate the orbital groups or "bodies".

Hybrid Extrapolation Approach: CEEMBE-h

When applying the CEEMBE method to CI calculations with excitations $X = 3$ or higher, it is possible to incorporate CEEIS extrapolations of the reduced CI energies. This combination of the two methods allows the reduced CI calculations in the full virtual space to be approximated by CEEIS extrapolations. There are two possible schemes for incorporating the CEEIS extrapolation:

> Scheme A – Extrapolate then add: The reduced CI energies (i.e. using only electrons in orbitals of a particular *i*-body combination for the CI excitations) in the full virtual space are individually extrapolated using CEEIS for each unique orbital group combination. These numbers are then used in the MBE formulas to obtain $E_{MBE}(X)$ in the full virtual space.
>
> Scheme B – Add then extrapolate: The reduced CI energies in the limited virtual orbital subsets are combined to obtain the series of $\Delta E_{MBE}(X \mid m)$ and $\Delta E_{MBE}(X-2 \mid m)$ required for a single CEEIS extrapolation to obtain $E_{MBE}(X)$ in the full virtual space.

Both schemes give good agreement with the original CEEMBE energies obtained without any CEEIS extrapolation and can greatly reduce the computational expense of the CEEMBE method. By performing these CEEIS extrapolations, the expensive calculations of the reduced CI energies in the full virtual space can be avoided.

In all the extrapolation methods described above, the results depend on the selection and ordering of the virtual orbitals. Previous work with CEEIS[11–13,18–21] and CEEMBE[10] have shown that CISD natural orbitals ordered by occupation number are a suitable basis for the virtual orbitals.

Computational Details

Calculations were performed using the occupation restricted multiple active space (ORMAS)[26] determinant CI code in the GAMESS program suite[27]. ORMAS provides the ability to specify the changing orbital spaces needed for the reduced CI calculations in the MBE approximation. Basis sets used are the Dunning correlation consistent cc-pVXZ series[28], with X = T, Q.

3. Results

The agreement of the CEEMBE-*h* energies compared to the original CEEMBE energies will be evaluated for the same systems and points on the potential energy surfaces as were used in our previous paper[10] on the CEEMBE method. Additionally, we will extend the number of points on the potential energy curve of F_2 to include the full dissociation.

Ozone

We will examine the following points of interest on the potential energy surfaces of the 1^1A_1 and 2^1A_1 states of the ozone molecule from the open minimum to the theoretically predicted, but experimentally unobserved ring minimum[29–32]:

OM – the 1^1A_1 open minimum

RM – the 1^1A_1 ring minimum

TS – the transition state between the OM and the RM on the 1^1A_1 surface

ESM – the minimum of the 2^1A_1 state

CX– the conical intersection between the 1^1A_1 and 2^1A_1 states

The geometries were obtained in a previous study[22] through optimizations of state-averaged CASSCF(18,12)/cc-pVQZ energies.

The correlated orbitals of the calculations are shown in Figure 2. The CI calculations performed include excitations from these orbitals into the virtual space. Two different reference wavefunctions and orbital groupings are used to define the MBE. The CASSCF(2,2) reference includes orbitals $2b_2$ and $4b_1$ in the active space, while the CASSCF(6,4) reference also includes

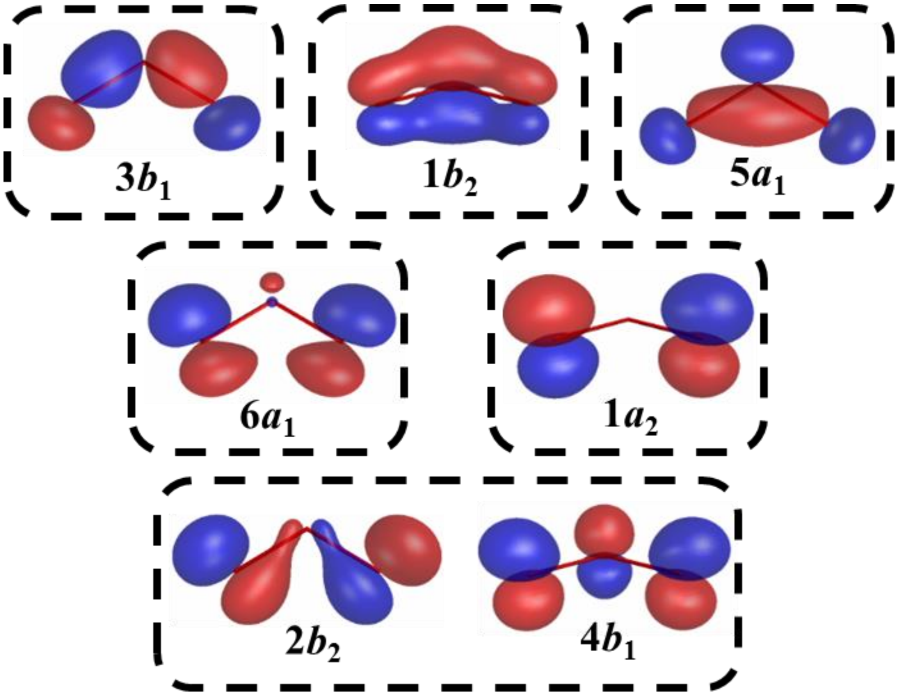

Figure 2. Correlated valence orbitals, as well as the orbital groups (indicated by dashed boxes) used in CEEMBE calculations with a (2,2)* reference. Images are from the state-averaged CASSCF(18,12)/cc-pVTZ wave functions for the 1 $^1A_1$ and 2 $^1A_1$ states of O_3 at the OM. Below each orbital, the symmetry label (in C_{2v}) is given.

orbitals 6a_1 and 1a_2. A more thorough discussion of the possible active spaces for this portion of the potential energy surface can be found in the earlier CEEIS study from Theis *et al*[22].

For CEEMBE calculations with either reference space, each doubly occupied orbital is used as an individual body, while the active space is grouped together into a multiple orbital body. The (2,2) reference MBE groups are shown in Figure 2. Pseudo-natural CISD orbitals from a block diagonalization of the virtual-virtual part of the one-particle density matrix are used in the virtual space. All results are reported for the cc-pVTZ basis set. The linear extrapolations (both CEEIS and CEEMBE) are performed using *m* values of 30, 35, and 40 for the (2,2) space, while 30, 36, and 40 were used for the (6,4) space. The *m* values are chosen to maintain consistency with and enable comparison to the previous work[10,22]. The full set of virtual orbitals includes 77 orbitals.

Table 1. Energy differences (CEEMBE minus CEEMBE-*h*, in millihartrees) between CEEMBE and CEEMBE-*h* calculations for CISDTQ energies of O_3 with the (2,2) reference space.

		Geometry				
		OM	TS	ESM	CX	RM
1^1A_1						
CEE2B	Scheme A	0.001	0.067	0.061	0.101	-0.013
	Scheme B	0.018	0.052	0.051	0.070	-0.026
CEE3B	Scheme A	-0.023	0.050	0.043	0.215	0.012
	Scheme B	0.029	0.140	0.141	0.485	0.066
2^1A_1						
CEE2B	Scheme A	0.010	0.063	0.103	0.169	
	Scheme B	0.008	0.085	0.085	0.135	
CEE3B	Scheme A	-0.029	0.043	0.082	0.130	
	Scheme B	-0.063	0.062	0.060	0.039	

Tables 1 and 2 report the energy differences between CEEMBE and CEEMBE-*h* energies at the CISDTQ level for the (2,2) and (6,4) references respectively. Both schemes are able to recover the CEEMBE energies to within ~0.1 millhartree or less at most geometries, and the current set of results do not clearly favor one scheme over another. The energy differences are largest at the CX, but are still less than 0.5 millihartree. The missing values at the RM for the 2^1A_1 state are due to a complication in the CEEMBE calculations which prevents performing a reasonable extrapolation with the MBE energies. CEEMBE energies at the CEE3B level were prohibitively expensive to calculate for the (6,4) reference. In all cases, the difference between CEEMBE and CEEMBE-*h* is on the same order of magnitude or smaller than the errors between CEEMBE energies and the target CI energies that have been previously observed. The good agreement between CEEMBE and CEEMBE-*h* is a direct result of the effectiveness of the CEEIS method for approximating CI energies with high levels of excitation.

Table 2. Energy differences (CEEMBE minus CEEMBE-*h*, in millihartrees) between CEEMBE and CEEMBE-*h* calculations for CISDTQ energies of O_3 with the (6,4) reference space.

		Geometry				
		OM	TS	ESM	CX	RM
1^1A_1						
CEE2B	Scheme A	-0.135	-0.033	-0.033	0.065	0.006
	Scheme B	-0.027	0.080	0.079	0.096	0.105
2^1A_1						
CEE2B	Scheme A	-0.232	0.078	0.077	0.151	
	Scheme B	-0.150	0.167	0.165	0.164	

F_2

The second system considered is diatomic fluorine. As was described in the Methods section, and depicted in Figure 1, the orbital groupings for F_2 give seven bodies consisting of six doubly occupied orbitals plus the (2,2) space consisting of the $3\sigma_g$ and $3\sigma_u$ orbitals. This reference space is needed to obtain a qualitative description of the dissociation of F_2. As with ozone, the previous CEEMBE results[10] are compared with the new CEEMBE-*h* approach. A section of the potential energy curve from the experimental equilibrium distance (~1. 412 Å) to near the dissociation inflection point (1.6 Å) was calculated using the cc-pVQZ basis. Valence orbitals were obtained from a CASSCF(2,2) calculation, while pseudo-natural CISD orbitals were used for the virtual set. Extrapolations were performed using virtual orbital subsets of m = 18, 24, and either 29 or 30, with a full virtual space of 100 orbitals.

Figure 3 shows the energy differences between CEEMBE and CEEMBE-*h* approaches across the chosen section of the potential energy curve. As with ozone, the CEEMBE-*h* energies are in very good agreement with the CEEMBE. For CEE2B energies, the difference is less than 0.1 millihartree at all points. The CEE3B values are consistently higher, but generally less than 0.5 millihartree. Whether the CEE3B-*h* agreement is systematically worse remains to be seen, as the same trend was not found in the ozone results. At all points, scheme A performs slightly worse than scheme B, however the relative difference is quite small and at the CEE2B level the difference is negligible.

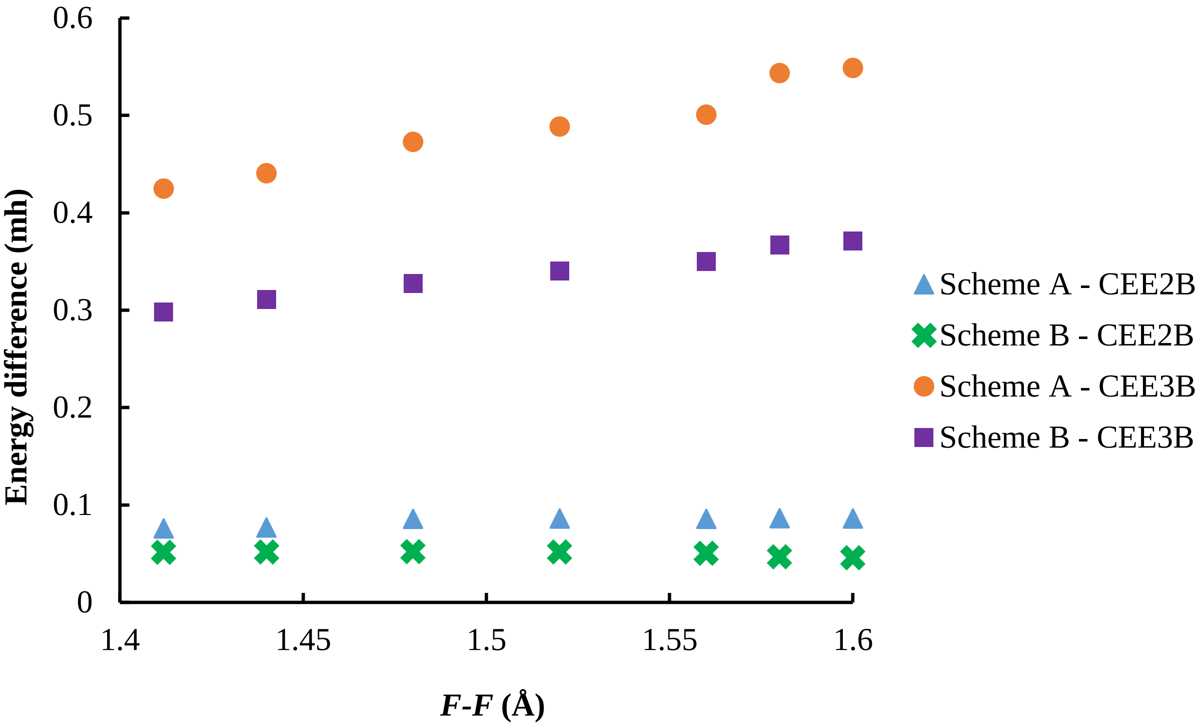

Figure 3. Energy differences (in millihartrees) between CEEMBE and CEEMBE-*h* calculations for CISDTQ energies of F_2 (cc-pVQZ basis).

Although the CEEMBE method was previously shown to achieve sub-millihartree accuracy on the small section of the potential energy curve above, the behavior across the entire dissociation channel was still unknown. In the interest of exploring the F_2 application more thoroughly, 13 points along the entire curve have been calculated. Both cc-pVTZ and cc-pVQZ basis sets were used, and CISDTQ energies were obtained for the cc-pVTZ basis in order to find the actual errors in the CEEMBE approaches. The results include CEEIS, CEEMBE, and CEEMBE-*h* energies.

The procedure for generating orbitals was modified slightly from above in order to match earlier work[18]. A full valence CASSCF(14,8) calculation provided the initial valence orbitals.

Then natural orbitals from a CISD calculation using the CAS(14,8) reference were used for the valence and virtual orbitals in the CEEIS, CEEMBE, and CEEMBE-*h* methods. Virtual orbital subsets of m = 18, 24, and 29 were used for the extrapolations. The full set of virtual orbitals contains 50 and 100 orbitals for the cc-pVTZ and cc-pVQZ basis sets respectively.

Figures 4 and 5 show the energy differences between CISDTQ level CEEMBE and CEEMBE-*h* energies. As before, the two approaches agree very well. CEE2B differences remain below ~0.1 millihartree for both basis sets, while the CEE3B values remain within 0.5 millihartree. An additional point at 8.0 Å is not pictured in the figures, but the energy difference is less than 0.08 millihartree with all methods and basis sets. Figure 5 reports only the CEE2B values, as the CEE3B results were not calculated across the entire curve with the cc-pVQZ basis due to expense, however CEE3B-*h* calculations were still feasible at this basis set level.

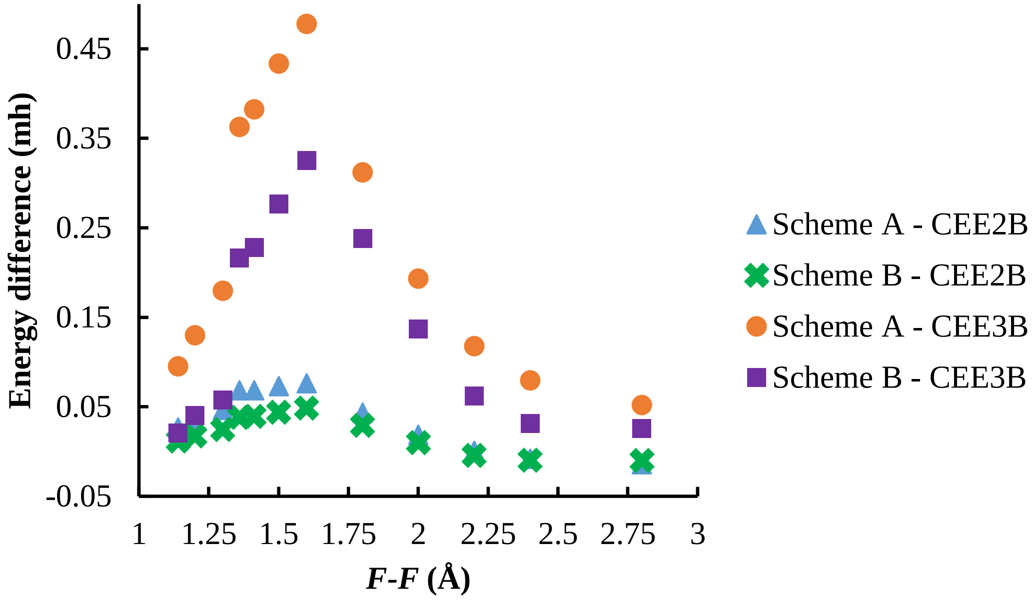

Figure 4. Energy differences (in millihartrees) between CEEMBE and CEEMBE-*h* calculations for CISDTQ energies of F_2 (cc-pVTZ basis).

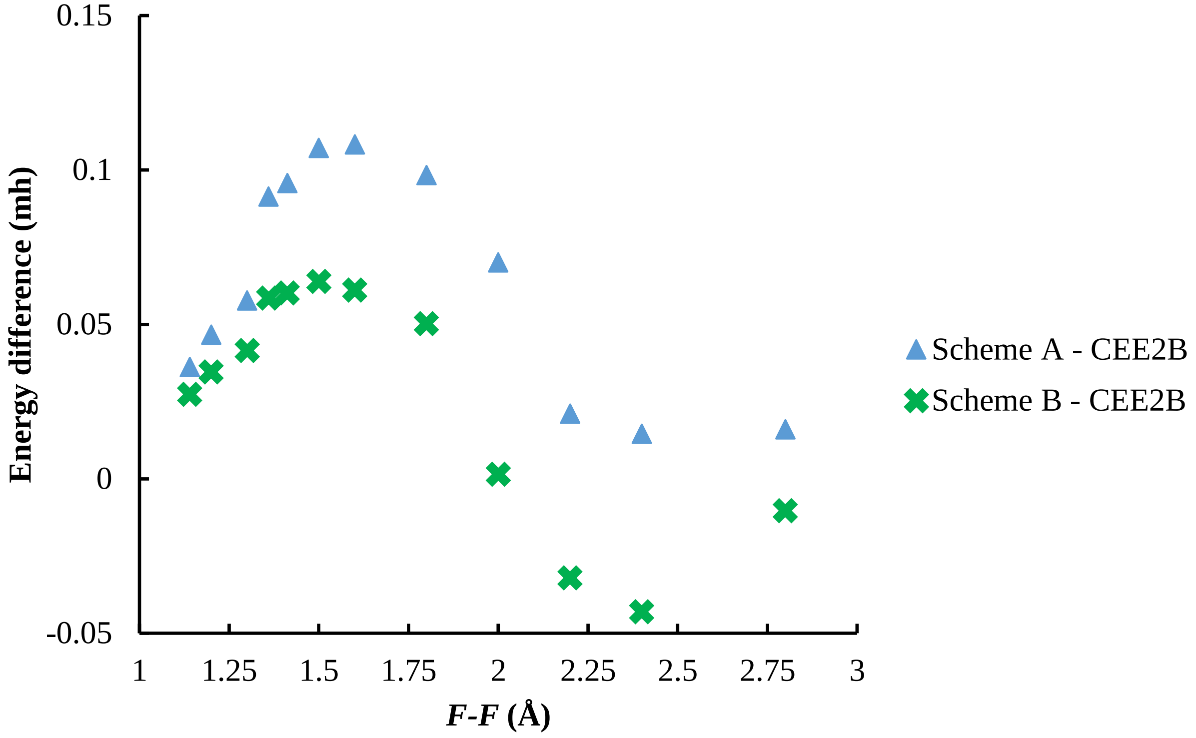

Figure 5. Energy differences (in millihartrees) between CEEMBE and CEEMBE-*h* calculations for CISDTQ energies of F_2 (cc-pVQZ basis).

Although the quality of the agreement between CEEMBE and CEEMBE-*h* results is well established, further benchmarking of the agreement of those energies with the true CI energies is of interest. Below we report the actual errors in CEEMBE (and CEEIS) energies across the potential energy curve at the CISDTQ level. Figure 6 shows the results with the cc-pVTZ basis, where the exact CISDTQ energy has been calculated and compared with the approximations.

For both CEE2B and CEE3B, the errors across the curve peak near ~1 millihartree, while the CEEIS errors remain below 0.6 millihartree. At 8 Å (not shown), the errors are -0.79, 1.22, and -0.08 for CEE2B, CEE3B, and CEEIS respectively. Comparing the two CEEMBE approximations, the CEE2B error fluctuates more across the curve, which is problematic in producing a smooth potential energy curve that parallels the true CISDTQ surface. In comparison, the CEE3B errors change much more smoothly. Overall, in this case, the CEEIS energies provide both a better relative and absolute approximation to the CISDTQ energy.

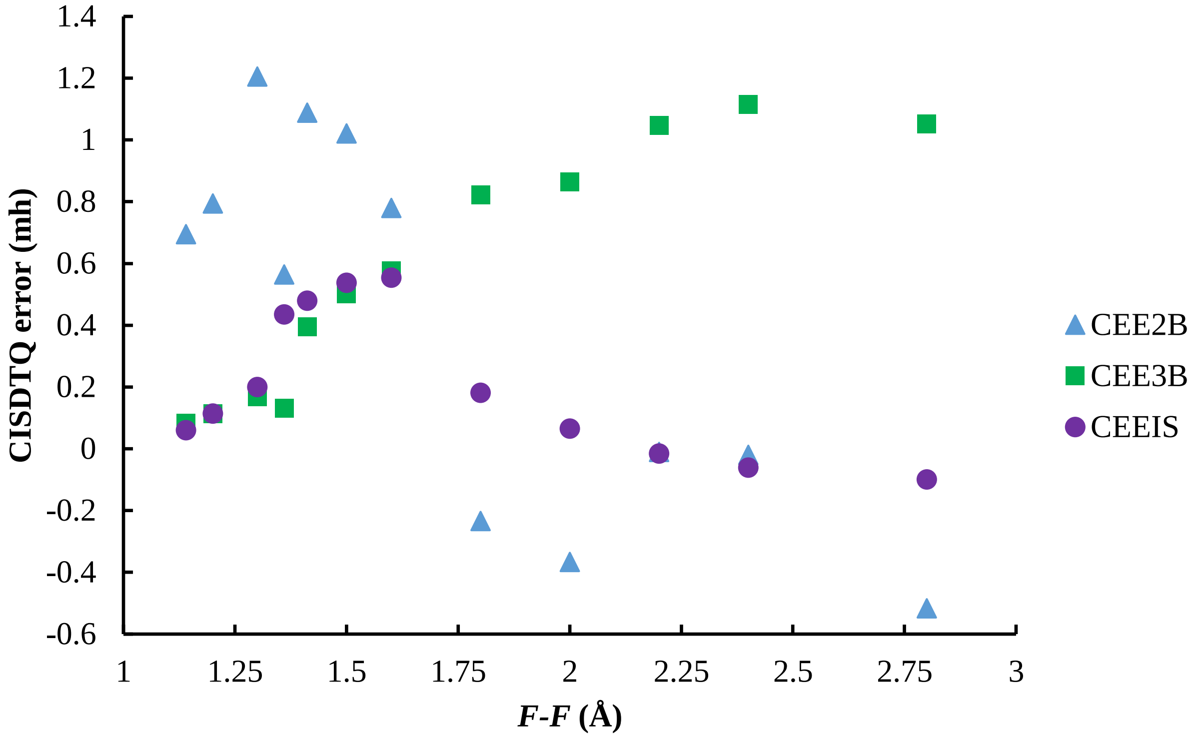

Figure 6. Errors (in millihartree) of CEEMBE and CEEIS energies compared to the true CISDTQ results for F_2 (cc-pVTZ basis).

Based on the cc-pVTZ results, the cc-pVQZ results are reported under the premise that the CEEIS energies provide a suitable benchmark. In Figure 7, the energy differences relative to the CEEIS method are reported for CEE2B and CEE3B-*h* using scheme B. The CEE3B-*h* results with scheme A are very similar. Although the exact accuracy of the CEEIS method is unknown for these points, the results for the CEEMBE methods are of lower quality at the larger separation distances. The CEE2B differences from CEEIS are as large as 2-3 millihartree at several points, and also vary considerably across the curve. The CEE3B differences again vary more smoothly, but also grow to as large as 2 millihartree at some distances.

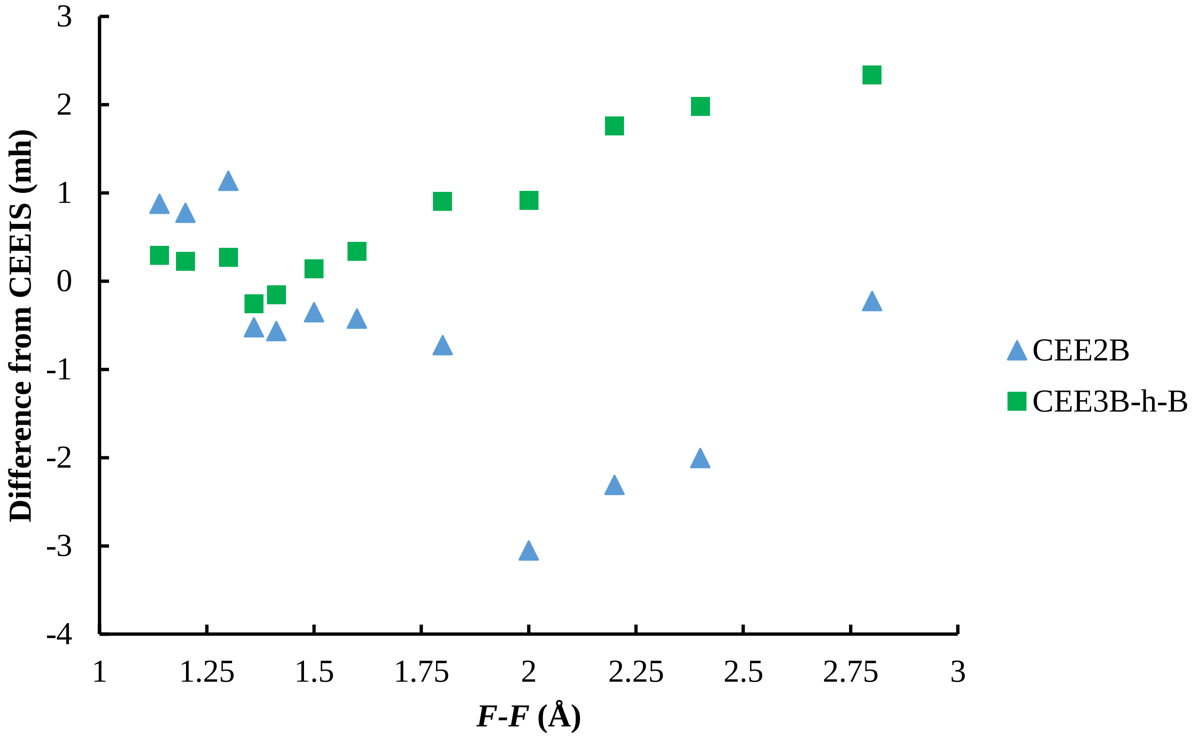

Figure 7. CEEMBE minus CEEIS energies (in millihartrees) at the CISDTQ level for F_2 (cc-pVQZ basis).

Although errors of 1-2 millihartree are still within chemical accuracy, further benchmarking would be required to fully assess the accuracy of the CEEMBE method. Of particular concern is the wide variation in the CEE2B results, which will affect the accuracy of relative energies as well. Improvement of the F_2 results may be possible with further exploration of the *m* values used in the extrapolations or of the initial orbitals used.

4. Discussion

The question of which CEEMBE-*h* scheme to favor is largely irrelevant, as both approaches give high quality agreement with the original CEEMBE method. A possible disadvantage of scheme A is the large number of linear extrapolations that must be performed: one for every unique orbital group combination of up to *n* bodies. However, these extrapolations are of inconsequential effort compared to the CI calculations.

Although not demonstrated in this paper, the CEEMBE method is applicable for CI calculations of lower excitation level as well. The previous work has shown the approximation can be effective at the CISD and CISDT levels. For the systems under consideration, CISD calculations are already affordable so the approximation is not of great interest. For large molecules or basis sets, the CEEMBE method may provide an affordable route to capturing electron correlation at lower excitation levels (SD or SDT). A current challenge of applying the method is the unknown value of the error compared to the target CI calculation. Benchmarking provides a general idea about the possible magnitudes of the errors, but still leaves the precise value undetermined. Furthermore, selection of *m* values for the linear extrapolations can have a significant impact on the final result. Preliminary results suggest that the accuracy of CEEMBE results at the CISD level may correlate with the accuracy of CEEMBE results at the CISDTQ level, but further examination is needed to establish whether the trend is consistent and precise enough to be useful.

Ultimately, the methodology is far from black-box and has a number of parameters which could affect the quality of results. Sensitivity to the choice of *m* values, orbitals, and orbital groupings all must be better understood to make the method more widely applicable.

5. Conclusions

The recently introduced CEEMBE method has been combined with the related CEEIS method to give a new hybrid approach: CEEMBE-*h*. Comparisons with the previous CEEMBE results in applications to ozone and F_2 show clearly that the CEEMBE and CEEMBE-*h* energies are in agreement to within ~0.1 millihartree or less in most cases, and the worst agreement is on the order of ~0.5 millihartree. These differences are generally an order of magnitude smaller than the CEEMBE errors, and as such, the CEEMBE-*h* offers reduced computational expense without loss of accuracy relative to the original CEEMBE approach. The good agreement is due to the accuracy of the CEEIS method for approximating high level CI energies.

A more thorough exploration of the F_2 dissociation curve has shown that the CEEMBE method can often achieve sub-millihartree accuracy, but that some points may show errors as large as a few millihartree. Also of note, CEE2B shows noticeably less smooth energy changes across the dissociation curve than the CEE3B method. Further benchmarking is still required to fully establish the level of accuracy which can be expected from the CEEMBE methods.

Acknowledgements

This work was supported by the US Department of Energy, Office of Basic Energy Sciences, Division of Chemical Sciences, Geosciences & Biosciences through the Ames Laboratory at Iowa State University under Contract No. DE-AC02-07CH11358. The work was partially supported by compute time and software management provided by the Research IT team at Iowa State University, utilizing HPC@ISU equipment, some of which has been purchased through funding provided by NSF under MRI grant number CNS 1229081 and CRI grant number 1205413.

References

(1) Bytautas, L.; Ruedenberg, K. *Chem. Phys.* **2009**, *356* (1–3), 64–75.

(2) Booth, G. H.; Thom, A. J. W.; Alavi, A. *J. Chem. Phys.* **2009**, *131* (5), 054106.

(3) Tubman, N. M.; Lee, J.; Takeshita, T. Y.; Head-Gordon, M.; Whaley, K. B. *J. Chem. Phys.* **2016**, *145* (4), 044112.

(4) Schriber, J. B.; Evangelista, F. A. *J. Chem. Phys.* **2016**, *144* (16), 161106.

(5) Knowles, P. J. *Mol. Phys.* **2015**, *113* (13–14), 1655–1660.

(6) Bytautas, L.; Scuseria, G. E.; Ruedenberg, K. *J. Chem. Phys.* **2015**, *143* (9), 094105.

(7) Liu, W.; Hoffmann, M. R. *J. Chem. Theory Comput.* **2016**, *12* (3), 1169–1178.

(8) Giner, E.; Scemama, A.; Caffarel, M. *J. Chem. Phys.* **2015**, *142* (4), 044115.

(9) Zimmerman, P. M. *J. Chem. Phys.* **2017**, *146* (10), 104102.

(10) Boschen, J. S.; Theis, D.; Ruedenberg, K.; Windus, T. L. *J. Phys. Chem. A* **2017**, *121* (4), 836–844.

(11) Bytautas, L.; Ruedenberg, K. *J. Chem. Phys.* **2004**, *121* (22), 10905–10918.

(12) Bytautas, L.; Ruedenberg, K. *J. Chem. Phys.* **2004**, *121* (22), 10919–10934.

(13) Bytautas, L.; Ruedenberg, K. *J. Chem. Phys.* **2005**, *122* (15), 154110.

(14) Stoll, H. *Phys. Rev. B* **1992**, *46* (11), 6700–6704.

(15) Paulus, B. *Phys. Rep.* **2006**, *428* (1), 1–52.

(16) Stoll, H.; Paulus, B.; Fulde, P. *J. Chem. Phys.* **2005**, *123* (14), 144108.

(17) Voloshina, E.; Paulus, B. *J. Chem. Theory Comput.* **2014**, *10* (4), 1698–1706.

(18) Bytautas, L.; Nagata, T.; Gordon, M. S.; Ruedenberg, K. *J. Chem. Phys.* **2007**, *127* (16), 164317.

(19) Bytautas, L.; Ruedenberg, K. *J. Chem. Phys.* **2010**, *132* (7), 074109.

(20) Bytautas, L.; Matsunaga, N.; Scuseria, G. E.; Ruedenberg, K. *J. Phys. Chem. A* **2012**, *116* (7), 1717–1729.

(21) Boschen, J. S.; Theis, D.; Ruedenberg, K.; Windus, T. L. *Theor. Chem. Acc.* **2013**, *133* (2), 1425.

(22) Theis, D.; Ivanic, J.; Windus, T. L.; Ruedenberg, K. *J. Chem. Phys.* **2016**, *144* (10), 104304.

(23) Gordon, M. S.; Fedorov, D. G.; Pruitt, S. R.; Slipchenko, L. V. *Chem. Rev.* **2012**, *112* (1), 632–672.

(24) Richard, R. M.; Lao, K. U.; Herbert, J. M. *Acc. Chem. Res.* **2014**, *47* (9), 2828–2836.

(25) Collins, M. A.; Bettens, R. P. A. *Chem. Rev.* **2015**, *115* (12), 5607–5642.

(26) Ivanic, J. *J. Chem. Phys.* **2003**, *119* (18), 9364–9376.

(27) Schmidt, M. W.; Baldridge, K. K.; Boatz, J. A.; Elbert, S. T.; Gordon, M. S.; Jensen, J. H.; Koseki, S.; Matsunaga, N.; Nguyen, K. A.; Su, S.; Windus, T. L.; Dupuis, M.; Montgomery, J. A. *J. Comput. Chem.* **1993**, *14* (11), 1347–1363.

(28) Dunning Jr., T. H. *J. Chem. Phys.* **1989**, *90* (2), 1007–1023.

(29) Hay, P. J.; Goodard, W. A. *Chem. Phys. Lett.* **1972**, *14* (1), 46–48.

(30) Hay, P. J.; Dunning, T. H.; Goddard, W. A. *Chem. Phys. Lett.* **1973**, *23* (4), 457–462.

(31) Wright, J. S. *Can. J. Chem.* **1973**, *51* (1), 139–146.

(32) Shih, S.; Buenker, R. J.; Peyerimhoff, S. D. *Chem. Phys. Lett.* **1974**, *28* (4), 463–470.

CHAPTER 7. PHOTODYNAMICS WITH SPIN-FLIP TIME-DEPENDENT DENSITY FUNCTIONAL THEORY FOR A MODEL PROTONATED SCHIFF BASE

Jeffery S. Boschen, Theresa L. Windus

Abstract

The spin-flip formulation of time-dependent density functional theory (SF-TDDFT) is one approach which addresses the shortcomings of conventional linear response TDDFT, and represents a potentially powerful tool for exploring photochemical dynamics. However, SF-TDDFT suffers from spin-contamination, and produces a manifold of states which are often difficult to identify with the physical states of interest. In this work, we implement nonadiabatic dynamics simulations using SF-TDDFT and evaluate the quality of the results on the model protonated Schiff base, penta-2,4-dieniminium cation, or PSB3. An interface between the Newton-X and GAMESS programs couples electronic structure calculations with molecular dynamics, and includes an algorithm for tracking the electronic states of interest. We present an extension of the Casida ansatz to SF-TDDFT, which allows the calculation of time-derivative couplings between states based on an approximate wave function overlap method. Qualitative agreement with analytical CASSCF time-derivative couplings demonstrate the soundness of the overlap method with SF-TDDFT. Our dynamic simulations of PSB3 *trans-cis* photoisomerization are qualitatively consistent with previous theoretical work, encouraging future studies with our methodology. Issues related to spin contamination and state tracking are likely to be a continuing concern.

1 Introduction

Photochemical processes are of great importance in biology, energy applications, as well molecular motors, switches, and probes. Modeling these processes requires a quantum chemical description of the electronic excited states, as well as the interactions between excited states. Conical intersections, the regions of degeneracy between two electronic states, are widely studied to understand the transitions between and decay from excited states[1–4]. Time-independent studies are usually focused on finding minimum energy conical intersections[5–7], but such minimum energy intersections are not necessarily the dominant path taken in the dynamic chemical reaction[8]. Increasingly, nonadiabatic molecular dynamics simulations are being used to explore excited state processes. The ultrafast nature of these reactions also make the application of on-the-fly quantum chemical calculations feasible despite their high computational cost.

Time-dependent density functional theory[9] (TDDFT), in the linear response formulation[10], is one of the most widely used methods for treating excited states of medium to large sized molecules. However, TDDFT has some shortcomings which limit its application to photochemical studies. In TDDFT, the ground state and excited states are not treated on the same footing. While the ground state is given by Kohn-Sham DFT[11], the excited states are obtained from the linear response of the ground state density to a time-dependent perturbation. Additionally, the excited states are described only in the basis of singly excited configurations, and excited states which possess double excitation character are not adequately represented. As a result, conical intersections between ground and excited states do not exhibit the correct topology[12,13]. This failure limits the application of TDDFT to photochemical processes.

An approach which addresses these shortcomings is the spin-flip TDDFT (SF-TDDFT) method[14]. SF-TDDFT builds all the states of interest with spin-flipping excitations from a high-spin reference state. This approach yields ground and excited states which are described by the same formalism and introduces some double excitation character into the states. However, SF-TDDFT is inherently spin-contaminated and one cannot guarantee that the method will produce states of the desired spin. Despite this, SF-TDDFT has been used to explore conical intersections in a large number of molecules[5–7,13,15–22], and has also been used to drive molecular dynamics[23–25].

We have developed an interface between the programs Newton-X[26,27] and GAMESS[28] to perform nonadiabatic dynamics simulations using SF-TDDFT and the fewest switches surface hopping (FSSH) method[29–31]. Following the dynamics on the correct electronic states requires a state-tracking algorithm to distinguish SF-TDDFT states, which are often spin-mixed. The nonadiabatic couplings between states are computed using an approximate wavefunction overlap method for which we introduce an extension of the Casida ansatz[10] from TDDFT to SF-TDDFT. We will evaluate the suitability of SF-TDDFT for nonadiabatic dynamic studies using the penta-2,4-dieniminium cation, a model chromophore.

The penta-2,4-dieniminium cation ($C_5H_8N^+$), or PSB3, has been widely studied[8,13,21,22,32–40] theoretically as the smallest model molecule for the retinal protonated Schiff bases (RPSBs). The *cis-trans* and *trans-cis* isomerization of RPSB chromophores are the primary photochemical processes in activating rhodopsin proteins that are key to vision mechanisms[41–45]. Figure 1 shows the ground state minima of the *trans-* and *cis-*PSB3. In previous work,[13,21,22] SF-TDDFT has been applied to the study of PSB3 isomerization, and has demonstrated that SF-TDDFT can model correctly the topology of the conical intersection. Several nonadiabatic dynamics studies have also been performed on PSB3[8,32,34] with other electronic structure methods, which will provide useful comparisons for the results in this work.

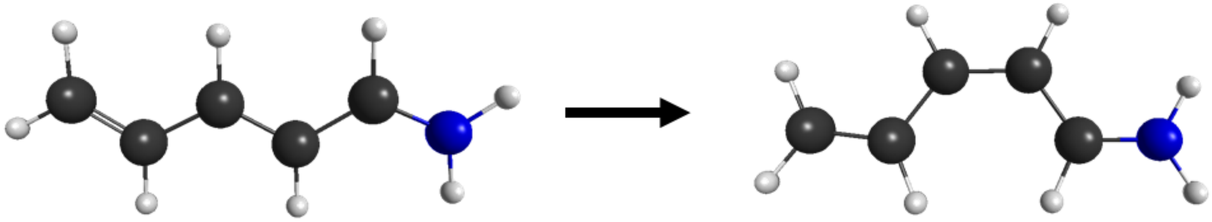

Figure 1. *trans*-PSB3 (left) and *cis*-PSB3 (right) S_0 minima.

2 Theoretical Methods

SF-TDDFT

As mentioned above, SF-TDDFT is based on calculating a high spin reference state using ground state Kohn-Sham DFT and then generating the states of interest using α to β spin-flip excitations. In this work, the high spin reference will be a triplet, as the states of interest are singlets. This spin-flip method only produces four configurations which are spin-complete and can form pure spin states. Figure 2 depicts these four configurations: **A** – the closed shell singlet which typically dominates the ground state of interest, **B** – a doubly excited closed shell singlet, and **C-D** – a pair of singly excited configurations which can form pure triplet/singlet states when combined with equal weights with same/opposite signs. When the weights of **C** and **D** are not equal the state will be spin contaminated to some degree. All other α to β excitations from the reference are spin incomplete and introduce spin contamination. The expectation value of the $\mathbf{S}^2$ operator, $\langle \mathbf{S}^2 \rangle$, provides a measure of the spin contamination of a state, and is equal to 0, 2, and 1 for pure singlet, pure triplet, and equally mixed singlet/triplet respectively.

Some work has been done to address the issue of spin contamination. An approximate spin projection formula[46,47] has been applied to correct the energies of mixed spin states after the SF-TDDFT calculation[21,22]. Approaches exist for ensuring pure spin states in open-shell TDDFT[48–51] as well as in spin-flip configuration interaction singles (SF-CIS)[52,53]. A recent work has also presented a spin-adapted method related to SF-TDDFT[54].

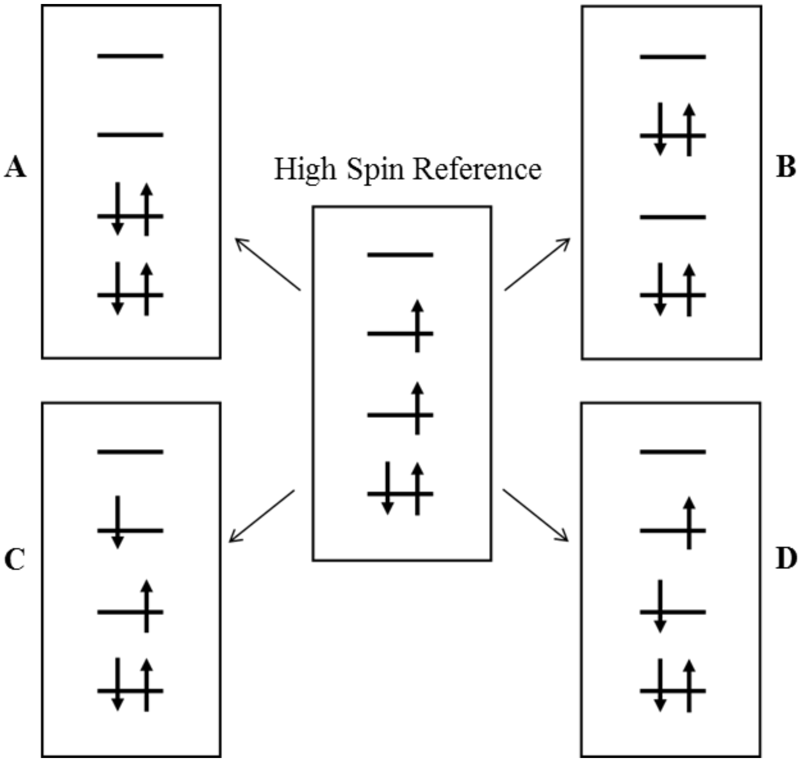

Figure 2. The set of configurations which can form spin-complete states in SF-TDDFT. From the reference triplet configuration, four different spin-flip excitations in the singly occupied orbitals generate configurations **A-D**. **A** and **B** correspond to closed shell singlets, while states with equal weights of **C** and **D** correspond to pure singlets or triplets (depending on signs).

Nonadiabatic Dynamics

The nonadiabatic dynamics simulations will follow Tully's fewest switches surface hopping (FSSH) method[29–31]. An ensemble of independent classical trajectories will move along a single active adiabatic potential from SF-TDDFT at each timestep. Surface hopping between adiabatic states occurs randomly based on the FSSH algorithm[31] and depends on the time-derivative couplings between the states:

$$\left\langle \Psi_j \middle| \frac{\partial}{\partial t} \Psi_k \right\rangle = \frac{\partial \mathbf{R}}{\partial t} \cdot \mathbf{d}_{jk} \tag{1}$$

In this work, the Ψ_j and Ψ_k will be S_0 or S_1. Eq. 1 shows the relation between the time-derivative coupling, $\left\langle \Psi_j \middle| \frac{\partial}{\partial t} \Psi_k \right\rangle$, the nuclear velocities, $\frac{\partial \mathbf{R}}{\partial t}$, and the nonadiabatic coupling vectors (NACVs), $\mathbf{d}_{jk}$:

$$d_{jk}^{(R)} = \left\langle \Psi_j \middle| \frac{\partial}{\partial R} \Psi_k \right\rangle \tag{2}$$

Recent work has demonstrated the implementation of analytical NACVs for SF-TDDFT[55,56]. The implementation of analytical NACVs for SF-TDDFT is not currently available in GAMESS. However, the time-derivative couplings may be computed using a finite difference approximation from wavefunction overlaps between the adiabatic surfaces at sequential timesteps[31]:

$$\left\langle \Psi_j \middle| \frac{\partial}{\partial t} \Psi_k \right\rangle \approx \frac{1}{2\Delta t} \left[\left\langle \Psi_j\left(t - \frac{\Delta t}{2}\right) \middle| \Psi_k\left(t + \frac{\Delta t}{2}\right) \right\rangle - \left\langle \Psi_j\left(t + \frac{\Delta t}{2}\right) \middle| \Psi_k\left(t - \frac{\Delta t}{2}\right) \right\rangle \right] \tag{3}$$

This approach has been applied with a variety of electronic structure methods[57–59]. However, SF-TDDFT does not give a wavefunction, and an approximate representation is needed to calculate the overlaps. In conventional linear response TDDFT, the so called Casida ansatz[10] is used in which the excited states are approximated by a CIS-like wavefunction[58,60,61]. We extend this approach for SF-TDDFT, and define the approximate CI wavefunction as:

$$\Psi_j = \sum_{i,a} c_{i,a} \psi_i^a \tag{4}$$

where ψ_i^a is the Slater determinant generated by a spin-flip excitation from the high spin reference Kohn-Sham orbitals, i.e. from the occupied α orbital i to the unoccupied β orbital a. The $c_{i,a}$ coefficients are set equal to the coefficients in the SF-TDDFT response vectors for state j. With this approximation, the state overlaps and time-derivative couplings are calculated from the SF-TDDFT response vectors, Kohn-Sham orbital coefficients, and atomic orbital overlaps. This approach has been implemented within the Newton-X framework using the GAMESS electronic structure code.

State Tracking

To propagate the nonadiabatic dynamics at each timestep requires the energy and gradient of the current state as well as the time-derivative couplings between all the states of interest. In this work, we will limit ourselves to the two lowest energy singlet states (S_0 and S_1). Because SF-TDDFT produces triplet, singlet, and mixed spin states, the identification of the two singlet states of interest at each timestep becomes nontrivial. This issue has been examined in the context of conical intersection searches[5,6,54], as well as dynamic simulations[23,24]. We will follow a modified version of the state tracking method proposed by Harabuchi *et al.*[23]

At each timestep the configuration coefficients, $c_{i,a}^{n+1}$, for every SF-TDDFT state are compared with the configurations coefficients, $c_{i,a}^{n}$, from S_0 and S_1 of the previous timestep. The following measure of similarity between the states at different timesteps is computed for all (j, k) pairs:

$$V_{jk} = \sum_{i,a} \left| c_{i,a}^{j,n} c_{i,a}^{k,n+1} \right| \tag{5}$$

where j is the state index of S_0 or S_1 at step n and k is the state index of any of the SF-TDDFT states at step $n + 1$. The states k with the highest V_{jk} are assigned as the new S_0 and S_1. States with an $\langle \mathbf{S}^2 \rangle$ value greater than 1.1 are excluded from assignment. In practice, we also found it necessary to restrict state assignments to those where the energy change between timesteps was less than 4 millihartree. The specific values for these constraints are arbitrary, and it is quite likely they can be improved upon.

Computational Details

CASSCF and SF-TDDFT calculations are performed using GAMESS, with the 6-31G(d) basis set[62]. The CASSCF calculations employ an active space of six π orbitals with six electrons and are state-averaged over the two lowest singlet states. SF-TDDFT calculations use the BHHLYP[63–65] functional and a restricted open-shell reference. The SF-TDDFT dynamics are propagated using Newton-X. Modifications were made to both GAMESS and Newton-X, and a Perl interface between the two was developed for performing both conventional TDDFT as well as SF-TDDFT dynamics. The interface is responsible for the state tracking described above and communicates geometries, energies, gradients, and the state information necessary to calculate the time-derivative couplings.

The *trans*-PSB3 S_0 minimum was optimized with SF-TDDFT and initial conditions were generated from a Wigner distribution of a quantum harmonic oscillator in the ground vibrational state[26,66]. All trajectories are initiated from the S_1 state. From an initial set of 100 trajectories, 88 trajectories were selected randomly based on transition probabilities given by $p = f / f_{max}$, where f is the oscillator strength between S_0 and S_1 for a given initial condition and f_{max} is the largest oscillator strength amongst the original 100 trajectories. Nuclear dynamics were propagated classically using the velocity-Verlet algorithm[67] with a timestep of 0.5 fs. The time-dependent Schrödinger equation was integrated with a sub-timestep of 0.025 fs using the fifth-order Butcher algorithm[68], with interpolation of the required quantities between full timesteps. Surface hops are attempted at each sub-timestep, and are only considered between S_0 and S_1. In case of a frustrated hop the momentum is maintained. After a successful hop the momentum is adjusted along the momentum direction, conserving total energy. Decoherence effects are included using the approach from Granucci and Persico[69] with $\alpha = 0.1$ hartree.

Of the initial 88 trajectories, 62 have been retained for analysis in the results section. Since we are interested largely in the dynamics surrounding S_1 to S_0 decay, the trajectories which fail before relaxing to the ground state or before reaching ~200 fs are ignored in the analysis. The rough 200 fs cutoff is selected as the point at which the excited state decay has greatly slowed down. The rejected trajectories have failed due to either convergence issues in the reference DFT or SF-TDDFT calculation, or because two singlet states could not be assigned under the energy difference and $\langle \mathbf{S}^2 \rangle$ constraints required by the state tracking algorithm described above. As the state tracking issues are more severe near the conical intersection between the states, these failures will bias our results to some degree towards trajectories which do not reach the conical intersection.

3 Results

Time-derivative Coupling Evaluation

We first consider the effectiveness of the overlap method for calculating time-derivative couplings in SF-TDDFT. As the analytical NACVs are not presently implemented in GAMESS for SF-TDDFT, we have chosen to make a qualitative comparison with the analytical couplings available for a two state-averaged SA-2-CASSCF(6,6) wavefunction. We have taken the geometries from a dynamic trajectory and performed CASSCF calculations at each point. The dot product of the CASSCF NACV and the nuclear velocity, as seen in Eq. 1, gives the time-derivative coupling which can be compared with the SF-TDDFT result using the overlap method of Eq. 3. Figure 3 shows a plot of the time-derivative couplings for both methods.

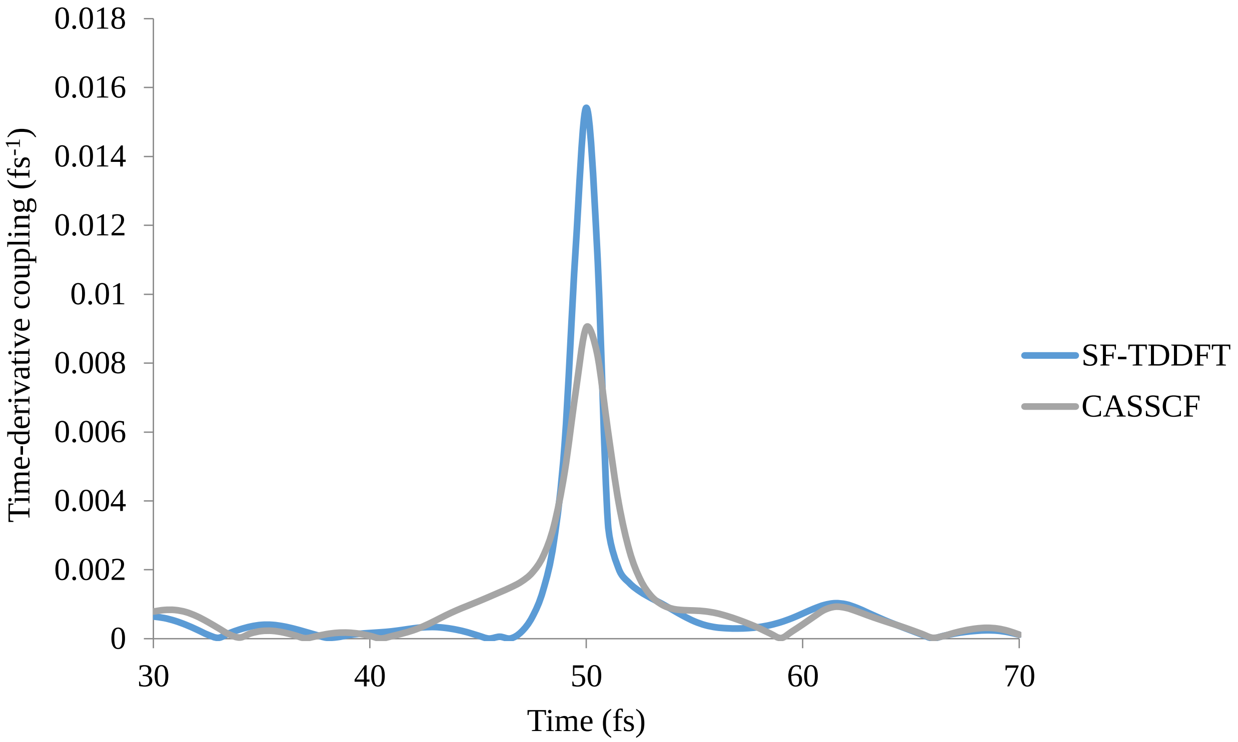

Figure 3. Time derivative couplings with SF-TDDFT and CASSCF between S_0 to S_1 along a single trajectory.

The trajectory hops from S_1 to S_0 at 50 fs. Although quantitative agreement between the two different methods is not expected, the qualitative agreement is quite good. Figure 4 reports the S_0 to S_1 excitation energies for the same timesteps. As expected, the coupling between the states remains small until the trajectory approaches the conical intersection between the two, at which point the coupling sharply increases. Examination of other trajectories gives similar qualitative agreement. These results suggest that the approximate wavefunction of Eq. 4 and the overlap method of calculating the couplings are appropriate for use in SF-TDDFT nonadiabatic dynamics. However, comparison with analytic NACVs would be needed to give a quantitative measure of the approximation's accuracy.

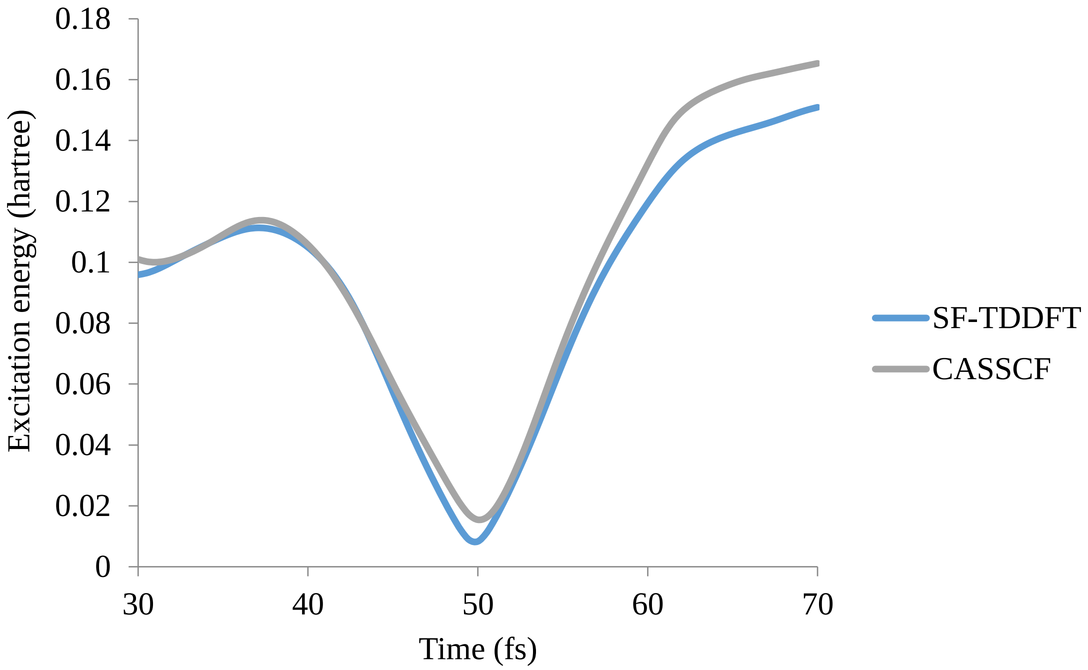

Figure 4. S_0 to S_1 excitation energies (in hartree) with SF-TDDFT and CASSCF along a single trajectory.

PSB3 Dynamics

As described in the methods section, 62 trajectories will be included in the analysis of the results. Figure 5 shows the S_1 population decay across all trajectories until a timestep of 200 fs. Trajectories which relax to S_0, move away from the conical intersection, and subsequently fail before 200 fs are reported as populating S_0 for the remaining timesteps up to 200 fs. This procedure is justified by the fact that the trajectories rapidly move away from the conical intersection after surface hopping to S_0 and the coupling between the two states quickly goes to near zero. There is a ~50 fs delay before trajectories reach the conical intersection and begin hopping to S_0. The S_1 decay has largely ceased by ~160 fs, with about 25% of trajectories remaining in the excited state.

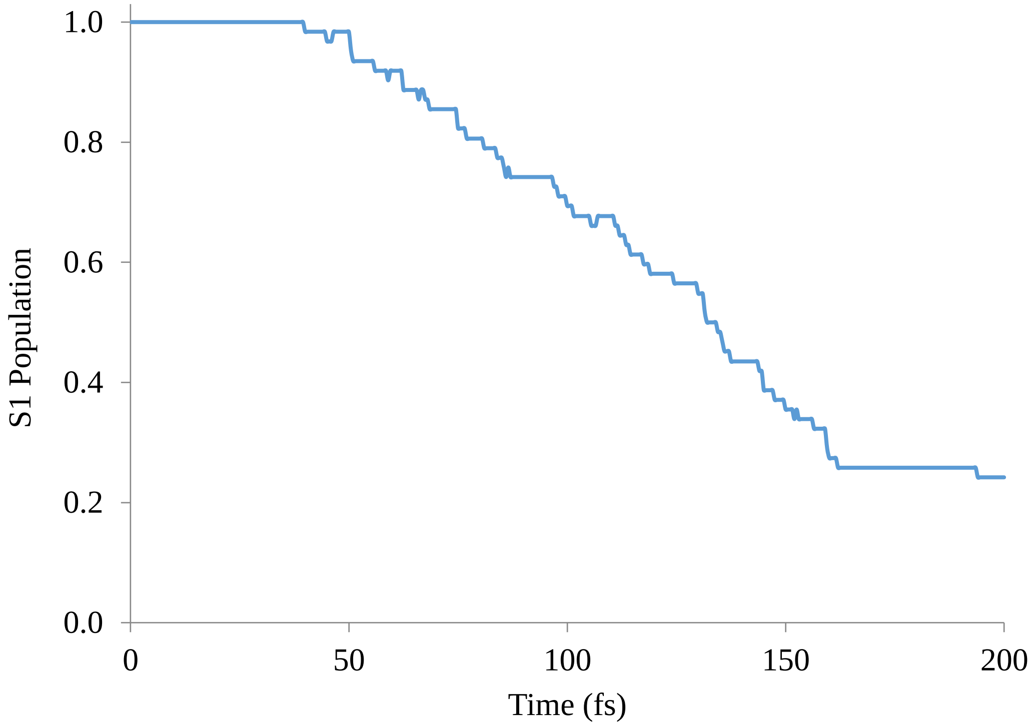

Figure 5. S_1 population of PSB3 as a function of time.

We compare our results with two previous nonadiabatic dynamics studies. Ruckenbauer *et al.*[34] applied FSSH using a multi-reference CIS (MR-CIS) wavefunction with a (4,5) active space of four electrons in five π orbitals and the 6-31G basis set. Liu *et al.*[8] applied ab initio multiple spawning[70] (AIMS) for the nonadiabatic dynamics, while their electronic structure methods were SA-3-CASSCF(6,6) and the multistate second order perturbation corrected CAS (MSPT2) method: SA-3-MS-CASPT2(6,6), both with the 6-31G basis. The references should be consulted for complete details. We will refer to the three sets of results as MR-CIS, CASSCF, and MSPT2 for brevity.

The MR-CIS results show an onset of decay at 49 fs using an exponential fit, in good agreement with our results. However, by 100 fs the MR-CIS and SF-TDDFT populations noticeably differ, as the MR-CIS S_1 population decays more rapidly. At ~160 fs the two methods differ by ~6%, and at 200 fs the difference is ~10%. The CASSCF results show a much shorter latency time at roughly 20 fs, while the MSPT2 latency is in good agreement with the MR-CIS and SF-TDDFT at ~50 fs. With the earlier onset of decay, the CASSCF population at 200 fs has already reached 10%. The MSPT2 population of ~22% is in very good agreement with SF-TDDFT. The MSPT2 and SF-TDDFT populations do diverge between 90-180 fs, where the MSPT2 values decay more rapidly until 140 fs, at which point the SF-TDDFT begins to decay more quickly.

Figure 6 shows the evolution of the average central C-C bond torsion angle. This angle is 180° at the *trans* isomer and 0° at the *cis* isomer. Comparison with the MR-CIS shows very good agreement until 75 fs, after which time the SF-TDDFT average rotation levels off while the MR-CIS angle continues to decrease; the discrepancy grows to ~25° around 120 fs, but an increasing MR-CIS torsion leads to a difference of only ~5° at 150 fs. The CASSCF and MSPT2 results reported in the reference for the average torsion angle have been restricted to AIMS trajectory basis functions that exhibit twisting about the central bond. Nonetheless, there is qualitative agreement with the average SF-TDDFT torsion, and discrepancies are on the order of 5-10° between the methods.

Although the comparisons provided are somewhat crude and qualitative, it is clear that the SF-TDDFT dynamics are capturing behavior similar to the wavefunction based methods. In particular, the close agreement with the dynamically correlated MSPT2 method is encouraging. Further simulations should focus on increasing the number of trajectories to ensure the results are statistically converged, and a great deal more analysis of the molecular motions is possible.

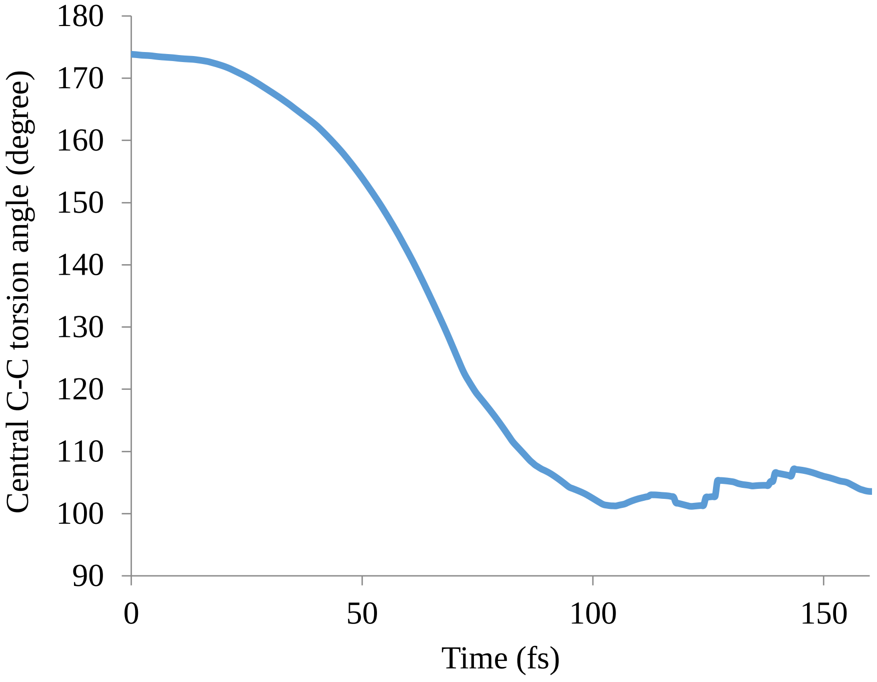

Figure 6. Average central C-C torsion angle of the *trans-cis* isomerization over all trajectories with SF-TDDFT.

Spin Contamination

We now examine the severity of and issues related to the spin contamination of SF-TDDFT states. Shown in Figure 7 is a measure of the average spin-contamination of the trajectories. At all timesteps the average ⟨**S**^{2}⟩ over all trajectories remains reasonably small for each of S_0, S_1, and the current active adiabatic state (either S_0 or S_1). In general, the trajectories are evolving on states with strong singlet character, and the time-derivative couplings are being computed between two primarily singlet states. Although the average for S_1 continues to increase as time increases, for most trajectories S_0 and S_1 will be widely separated and decoupled by that time.

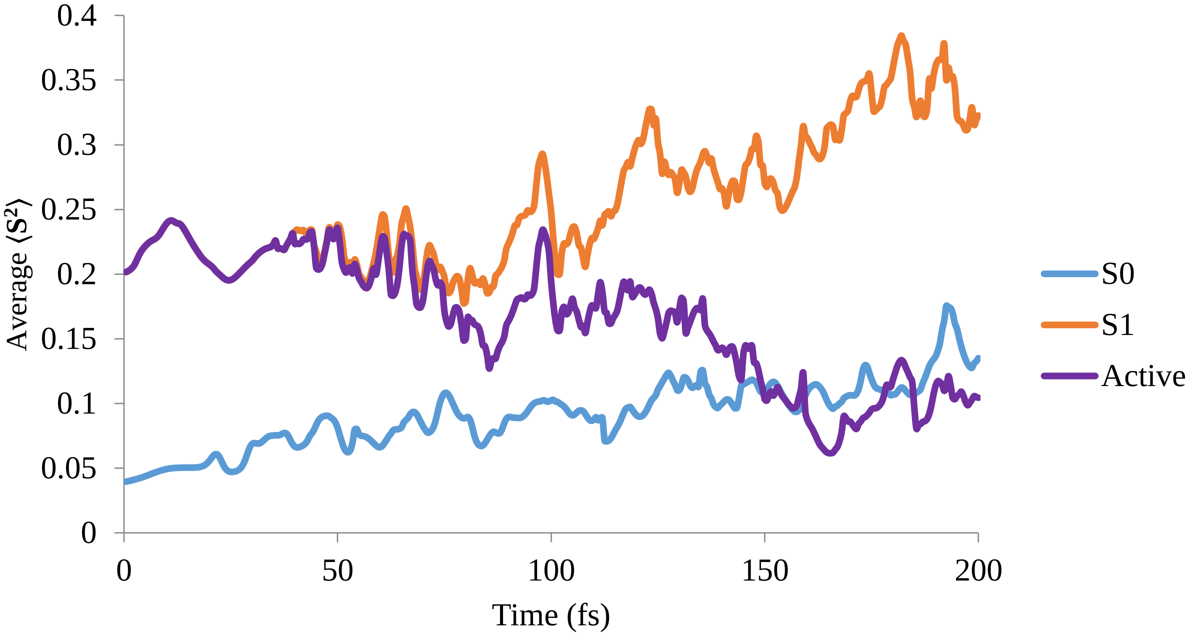

Figure 7. Average value of ⟨**S**^{2}⟩ over all trajectories for S_0, S_1, and the active electronic state.

However, the average value across all trajectories will mask to some degree the timesteps and specific trajectories which experience large amounts of spin contamination. If we count the timesteps (under 200 fs) where $\langle \mathbf{S}^2 \rangle > 0.75$, this occurs on average at 2% of timesteps for the active state and 8% of timesteps for one of either S_0 or S_1. The individual trajectories with the highest number of timesteps where $\langle \mathbf{S}^2 \rangle > 0.75$ showed high contamination 13% and 58% of the time for the active state and either S_0 or S_1. So even trajectories which do not experience state mixing severe enough to disrupt the state tracking algorithm may still spend a significant portion of time either reading energies and gradients, or at the very least time-derivative couplings from a spin-mixed state. The physical soundness of such a simulation is questionable, and additional benchmarking would be required to justify SF-TDDFT nonadiabatic dynamics simulations.

Returning to the state tracking algorithm, while the $\langle \mathbf{S}^2 \rangle < 1.1$ requirement does limit the amount of spin contamination tolerated in the trajectories, this constraint often leads to a trajectory failure after the trajectory has relaxed to the ground state and left the region of the conical intersection. In these cases, the $\langle \mathbf{S}^2 \rangle$ value of S_1 is too high, but the large separation between the two states means that the accuracy of the time-derivative couplings is no longer important as the coupling will be negligible. Finding two pure singlet states is not necessary to ensure a quality trajectory, only a sufficiently spin pure S_0. A modified algorithm which accounts for these issues would certainly decrease the number of trajectory failures. This will be especially important in applications where the dynamics on the ground state after relaxation are of interest.

4 Conclusions

We have demonstrated the use of SF-TDDFT for FSSH dynamics on the model chromophore PSB3. Our approach calculates the time-derivative coupling vectors using wavefunction overlaps. We approximate the SF-TDDFT states using SF-CIS-like wavefunctions generated from the high spin reference Kohn-Sham orbitals. This approximation has been validated as qualitatively correct in comparison with CASSCF calculations using analytical NACVs. A state tracking algorithm is employed to assign the S_0 and S_1 states at each timestep from the manifold of SF-TDDFT states. Our algorithm will not assign a mixed state with $\langle \mathbf{S}^2 \rangle > 1.1$ as S_0 or S_1, and this restriction does lead to some number of premature trajectory failures. Subtler criteria for state assignment will likely alleviate some number of trajectory failures while maintaining a similar quality of results. These methods and algorithms have been implemented within the Newton-X and GAMESS programs.

The nonadiabatic dynamics on PSB3 are in qualitative agreement with previous theoretical work on the molecule. A characteristic delay of roughly 50 fs before S_1 depopulation initiates is consistent across the methods. The rate of decay over 200 fs is more variable between different studies, but overall similar. The agreement between MSPT2 and SF-TDDFT is particularly good. The basic geometry change in the isomerization, twisting around the central C-C bond, is also described consistently by the various electronic structure and nonadiabatic dynamics. Much more analysis of the molecular motions in the SF-TDDFT dynamics is possible, and additional simulations are needed to establish the statistical reliability of the results presented. Exploring a greater range of systems, in particular larger molecules, could help to demonstrate the advantages of using SF-TDDFT for dynamics.

While the average ⟨$\mathbf{S}^2$⟩ on the active SF-TDDFT state is generally quite small, some trajectories propagate on mixed spin states for a significant portion of the simulation time, and at least one of the two “singlet” states shows mixed character for an even greater number of timesteps. The suitability and physical relevance of these mixed states is still not clear, despite our results that suggest the qualitative dynamic behavior is preserved. Practically speaking, the need for careful state tracking and evaluation of spin contamination limits the desirability SF-TDDFT dynamics studies. Spin adapted formulations[54] may ultimately solve these issues in a much more satisfactory way than any state tracking approach.

Acknowledgements

This work was supported by the US Department of Energy, Office of Basic Energy Sciences, Division of Chemical Sciences, Geosciences & Biosciences through the Ames Laboratory at Iowa State University under Contract No. DE-AC02-07CH11358.

References

(1) Yarkony, D. R. *J. Phys. Chem. A* **2001**, *105* (26), 6277–6293.

(2) Matsika, S.; Krause, P. *Annu. Rev. Phys. Chem.* **2011**, *62* (1), 621–643.

(3) Levine, B. G.; Martínez, T. J. *Annu. Rev. Phys. Chem.* **2007**, *58* (1), 613–634.

(4) Blancafort, L. *ChemPhysChem* **2014**, *15* (15), 3166–3181.

(5) Harabuchi, Y.; Maeda, S.; Taketsugu, T.; Minezawa, N.; Morokuma, K. *J. Chem. Theory Comput.* **2013**, *9* (9), 4116–4123.

(6) Maeda, S.; Harabuchi, Y.; Taketsugu, T.; Morokuma, K. *J. Phys. Chem. A* **2014**, *118* (51), 12050–12058.

(7) Harabuchi, Y.; Taketsugu, T.; Maeda, S. *Phys. Chem. Chem. Phys.* **2015**, *17* (35), 22561–22565.

(8) Liu, L.; Liu, J.; Martinez, T. J. *J. Phys. Chem. B* **2016**, *120* (8), 1940–1949.

(9) Runge, E.; Gross, E. K. U. *Phys. Rev. Lett.* **1984**, *52* (12), 997–1000.

(10) Casida, M. E. In *Recent Advances in Density Functional Methods (Part 1)*; 1995; pp 155–192.

(11) Kohn, W.; Sham, L. J. *Phys. Rev.* **1965**, *140* (4A), A1133–A1138.

(12) Levine, B. G.; Ko, C.; Quenneville, J.; MartÍnez, T. J. *Mol. Phys.* **2006**, *104* (5–7), 1039–1051.

(13) Gozem, S.; Melaccio, F.; Valentini, A.; Filatov, M.; Huix-Rotllant, M.; Ferré, N.; Frutos, L. M.; Angeli, C.; Krylov, A. I.; Granovsky, A. A.; Lindh, R.; Olivucci, M. *J. Chem. Theory Comput.* **2014**, *10* (8), 3074–3084.

(14) Shao, Y.; Head-Gordon, M.; Krylov, A. I. *J. Chem. Phys.* **2003**, *118* (11), 4807–4818.

(15) Minezawa, N.; Gordon, M. S. *J. Phys. Chem. A* **2009**, *113* (46), 12749–12753.

(16) Minezawa, N.; Gordon, M. S. *J. Phys. Chem. A* **2011**, *115* (27), 7901–7911.

(17) Zhang, X.; Herbert, J. M. *J. Phys. Chem. B* **2014**, *118* (28), 7806–7817.

(18) Suzuki, S.; Maeda, S.; Morokuma, K. *J. Phys. Chem. A* **2015**, *119* (47), 11479–11487.

(19) Isegawa, M.; Morokuma, K. *J. Phys. Chem. A* **2015**, *119* (18), 4191–4199.

(20) Li, Y.; Liu, F.; Wang, B.; Su, Q.; Wang, W.; Morokuma, K. *J. Chem. Phys.* **2016**, *145* (24), 244311.

(21) Xu, X.; Gozem, S.; Olivucci, M.; Truhlar, D. G. *J. Phys. Chem. Lett.* **2013**, *4* (2), 253.

(22) Zhou, P.; Liu, J.; Han, K.; He, G. *J. Comput. Chem.* **2014**, *35* (2), 109–120.

(23) Harabuchi, Y.; Keipert, K.; Zahariev, F.; Taketsugu, T.; Gordon, M. S. *J. Phys. Chem. A* **2014**, *118* (51), 11987–11998.

(24) Harabuchi, Y.; Yamamoto, R.; Maeda, S.; Takeuchi, S.; Tahara, T.; Taketsugu, T. *J. Phys. Chem. A* **2016**, *120* (44), 8804–8812.

(25) Yue, L.; Lan, Z.; Liu, Y.-J. *J. Phys. Chem. Lett.* **2015**, *6* (3), 540–548.

(26) Barbatti, M.; Granucci, G.; Persico, M.; Ruckenbauer, M.; Vazdar, M.; Eckert-Maksić, M.; Lischka, H. *J. Photochem. Photobiol. Chem.* **2007**, *190* (2–3), 228–240.

(27) Barbatti, M.; Ruckenbauer, M.; Plasser, F.; Pittner, J.; Granucci, G.; Persico, M.; Lischka, H. *Wiley Interdiscip. Rev. Comput. Mol. Sci.* **2014**, *4* (1), 26–33.

(28) Schmidt, M. W.; Baldridge, K. K.; Boatz, J. A.; Elbert, S. T.; Gordon, M. S.; Jensen, J. H.; Koseki, S.; Matsunaga, N.; Nguyen, K. A.; Su, S.; Windus, T. L.; Dupuis, M.; Montgomery, J. A. *J. Comput. Chem.* **1993**, *14* (11), 1347–1363.

(29) Tully, J. C.; Preston, R. K. *J. Chem. Phys.* **1971**, *55* (2), 562–572.

(30) Tully, J. C. *J. Chem. Phys.* **1990**, *93* (2), 1061–1071.

(31) Hammes-Schiffer, Sharon; Tully, J. C. *J. Chem. Phys.* **1994**, *101* (6), 4657–4667.

(32) Szymczak, J. J.; Barbatti, M.; Lischka, H. *J. Chem. Theory Comput.* **2008**, *4* (8), 1189–1199.

(33) Tuna, D.; Lefrancois, D.; Wolański, Ł.; Gozem, S.; Schapiro, I.; Andruniów, T.; Dreuw, A.; Olivucci, M. *J. Chem. Theory Comput.* **2015**, *11* (12), 5758–5781.

(34) Ruckenbauer, M.; Barbatti, M.; Müller, T.; Lischka, H. *J. Phys. Chem. A* **2013**, *117* (13), 2790–2799.

(35) Huix-Rotllant, M.; Filatov, M.; Gozem, S.; Schapiro, I.; Olivucci, M.; Ferré, N. *J. Chem. Theory Comput.* **2013**, *9* (9), 3917.

(36) Gozem, S.; Krylov, A. I.; Olivucci, M. *J. Chem. Theory Comput.* **2013**, *9* (1), 284–292.

(37) Kobayashi, O.; Nanbu, S. *Chem. Phys.* **2015**, *461*, 47–57.

(38) Mori, T.; Nakano, K.; Kato, S. *J. Chem. Phys.* **2010**, *133* (6), 064107.

(39) Gozem, S.; Melaccio, F.; Lindh, R.; Krylov, A. I.; Granovsky, A. A.; Angeli, C.; Olivucci, M. *J. Chem. Theory Comput.* **2013**, *9* (10), 4495–4506.

(40) Gozem, S.; Huntress, M.; Schapiro, I.; Lindh, R.; Granovsky, A. A.; Angeli, C.; Olivucci, M. *J. Chem. Theory Comput.* **2012**, *8* (11), 4069–4080.

(41) Birge, R. R. *Biochim. Biophys. Acta BBA - Bioenerg.* **1990**, *1016* (3), 293–327.

(42) Schoenlein, R. W.; Peteanu, L. A.; Mathies, R. A.; Shank, C. V. *Science* **1991**, *254* (5030), 412–415.

(43) Palings, I.; Pardoen, J. A.; Van den Berg, E.; Winkel, C.; Lugtenburg, J.; Mathies, R. A. *Biochemistry (Mosc.)* **1987**, *26* (9), 2544–2556.

(44) Altoè, P.; Cembran, A.; Olivucci, M.; Garavelli, M. *Proc. Natl. Acad. Sci.* **2010**, *107* (47), 20172–20177.

(45) Polli, D.; Altoè, P.; Weingart, O.; Spillane, K. M.; Manzoni, C.; Brida, D.; Tomasello, G.; Orlandi, G.; Kukura, P.; Mathies, R. A.; Garavelli, M.; Cerullo, G. *Nature* **2010**, *467* (7314), 440–443.

(46) Yamaguchi, K.; Tsunekawa, T.; Toyoda, Y.; Fueno, T. *Chem. Phys. Lett.* **1988**, *143* (4), 371–376.

(47) Shoji, M.; Koizumi, K.; Kitagawa, Y.; Kawakami, T.; Yamanaka, S.; Okumura, M.; Yamaguchi, K. *Chem. Phys. Lett.* **2006**, *432* (1–3), 343–347.

(48) Vahtras, O.; Rinkevicius, Z. *J. Chem. Phys.* **2007**, *126* (11), 114101.

(49) Li, Z.; Liu, W. *J. Chem. Phys.* **2010**, *133* (6), 064106.

(50) Li, Z.; Liu, W.; Zhang, Y.; Suo, B. *J. Chem. Phys.* **2011**, *134* (13), 134101.

(51) Li, Z.; Liu, W. *J. Chem. Phys.* **2011**, *135* (19), 194106.

(52) Sears, J. S.; Sherrill, C. D.; Krylov, A. I. *J. Chem. Phys.* **2003**, *118* (20), 9084–9094.

(53) Tsuchimochi, T. *J. Chem. Phys.* **2015**, *143* (14), 144114.

(54) Zhang, X.; Herbert, J. M. *J. Chem. Phys.* **2015**, *143* (23), 234107.

(55) Zhang, X.; Herbert, J. M. *J. Chem. Phys.* **2014**, *141* (6), 064104.

(56) Zhang, X.; Herbert, J. M. *J. Chem. Phys.* **2015**, *142* (6), 064109.

(57) Pittner, J.; Lischka, H.; Barbatti, M. *Chem. Phys.* **2009**, *356* (1–3), 147–152.

(58) Barbatti, M.; Pittner, J.; Pederzoli, M.; Werner, U.; Mitrić, R.; Bonačić-Koutecký, V.; Lischka, H. *Chem. Phys.* **2010**, *375* (1), 26–34.

(59) Plasser, F.; Crespo-Otero, R.; Pederzoli, M.; Pittner, J.; Lischka, H.; Barbatti, M. *J. Chem. Theory Comput.* **2014**, *10* (4), 1395–1405.

(60) Tavernelli, I.; Tapavicza, E.; Rothlisberger, U. *J. Mol. Struct. THEOCHEM* **2009**, *914* (1–3), 22–29.

(61) Werner, U.; Mitrić, R.; Suzuki, T.; Bonačić-Koutecký, V. *Chem. Phys.* **2008**, *349* (1–3), 319–324.

(62) Hariharan, P. C.; Pople, J. A. *Theor. Chim. Acta* **1973**, *28* (3), 213–222.

(63) Becke, A. D. *Phys. Rev. A* **1988**, *38* (6), 3098–3100.

(64) Becke, A. D. *J. Chem. Phys.* **1993**, *98* (2), 1372–1377.

(65) Lee, C.; Yang, W.; Parr, R. G. *Phys. Rev. B* **1988**, *37* (2), 785–789.

(66) Barbatti, M.; A. Aquino, A. J.; Lischka, H. *Phys. Chem. Chem. Phys.* **2010**, *12* (19), 4959–4967.

(67) Swope, W. C.; Andersen, H. C.; Berens, P. H.; Wilson, K. R. *J. Chem. Phys.* **1982**, *76* (1), 637–649.

(68) Butcher, J. C. *J. ACM JACM* **1965**, *12* (1), 124–135.

(69) Granucci, G.; Persico, M. *J. Chem. Phys.* **2007**, *126* (13), 134114.

(70) Virshup, A. M.; Punwong, C.; Pogorelov, T. V.; Lindquist, B. A.; Ko, C.; Martínez, T. J. *J. Phys. Chem. B* **2009**, *113* (11), 3280–3291.

CHAPTER 8. GENERAL CONCLUSIONS

The interactions between S and Cu surfaces has been examined through DFT calculations using both atomic orbital and plane-wave basis sets. Cu clusters of varying sizes and two types are examined: tetrahedral with exposed (111) facets, and square pyramidal with an exposed (100) base. Good agreement between the atomic orbital and plane wave based calculations was found across the clusters studied. We find that strong oscillations in the S binding energy exists, even in clusters of several hundred atoms. Such quantum size effects are expected for small clusters with discrete energy levels, however, the observed oscillations persist even for cluster sizes of a few hundred atoms where a density of states description of the system applies. Two techniques were shown to help alleviate the binding energy oscillation: 1) using smearing to create partial occupancy in the plane-wave DFT calculations, or 2) averaging adsorption energy over a range of cluster sizes. Both approaches aid in relating calculations on small to medium size clusters to bulk behavior. Comparison of the results for binding to (100) and (111) facets yielded insights into the experimentally observed preference for S binding to four-fold hollow sites over three-fold hollow sites. An analysis combining crystal orbital Hamiltonian population and site-projected density of states results suggest that the bonding interactions at the four-fold and three-fold hollow site are of similar strength, but that antibonding interactions are greater in the three-fold hollow sites, leading to the overall preference for four-fold hollow sites.

In an extension of the CEEIS method to study multiple excited states, highly accurate, benchmark quality PECs of C_2 singlet states were calculated. By employing complete basis set extrapolations of the reference and correlation energies, and including core-valence correlation, spin-orbit coupling, and relativistic effects, we were able to achieve a chemically accurate dissociation energy that deviates from experiment by only -0.38 kcal/mol. Our theoretical ro-vibrational levels for the four lowest-lying singlet states demonstrate “near spectroscopic accuracy”, with mean absolute deviations from experiment of between 10-20 cm^{-1}. We found that using dynamic weighting in state-averaged MCSCF calculations made a negligible impact on the electronic energies once dynamic correlation was included by CEEIS.

Closely related to CEEIS, the CEEMBE method was developed and tested in application to ozone and F_2. CEEMBE provides an approximation of CI energies at a reduced computational expense. By dividing the valence orbital space into separate bodies, reduced CI calculations are performed using only a small number of bodies. If all combinations of up to *n*-bodies are calculated, an *n*-body MBE approximation of the CI energy can be obtained. A correction to this MBE energy is calculated, in analogy to CEEIS, using a linear extrapolation of CI energies featuring a reduced number of virtual orbitals. CEEMBE calculations on a portion of the F_2 ground state PEC show errors of less than 1 millihartree using MBEs of 2- and 3-bodies. Characteristic points on potential energy surfaces of the 1^1A_1 and 2^1A_1 states of ozone have shown errors of no greater than ~2-3 millihartree, and often less than 1 millihartree.

We have also developed a combination of the CEEIS and CEEMBE methods, CEEMBE-*h*, which should be considered an approximation of the original CEEMBE approach. In CEEMBE-*h*, the reduced CI calculations in the full set of virtual orbitals are approximated using a CEEIS extrapolation. This reduces the computational cost of calculating the MBE approximate CI energies. The remainder of the calculation is identical to the original CEEMBE method. Calculations on ozone and the F_2 dissociation curve show that the agreement between CEEMBE-*h* and CEEMBE is generally within ~0.1 millihartree or less, and no worse than ~0.5 millihartree, which can be attributed to the accuracy of the CEEIS extrapolations. Further benchmarking of the CEEMBE approach on the full F_2 dissociation curve show that CEEMBE errors may be as large as a few millihartree, though the method often achieves sub-millihartree accuracy.

SF-TDDFT driven nonadiabatic dynamics were made possible by an interface between the programs Newton-X and GAMESS. Nonadiabatic effects are treated by surface hopping, which requires the calculation of time-derivative couplings between SF-TDDFT states. A finite difference method using wavefunction overlaps is used to compute the couplings. Approximate wavefunctions are constructed for the SF-TDDFT states by extending the Casida ansatz to the spin-flip case. The approximate couplings were found to be in good agreement with analytical couplings from CASSCF calculations. SF-TDDFT calculations are spin-contaminated and produce a set of states which can include singlets, triplets, and mixed-spin states. A state tracking algorithm is used to follow the singlet states of interest during the simulation. Nonadiabatic dynamic simulations on the PSB3 model chromophore showed good agreement with previous theoretical results, including a characteristic 50 fs time-delay before S_1 depopulation begins. The average spin-contamination across all trajectories is not severe, however, some trajectories were observed to move along heavily spin-contaminated states for significant amounts of time.